Ice Nucleation Activity of Soil Dust Aerosols

Zur Erlangung des akademischen Grades eines
DOKTORS DER NATURWISSENSCHAFTEN
von der Fakultät für Physik des
Karlsruher Instituts für Technologie (KIT)

genehmigte

DISSERTATION

von

Dipl.-Met. Thea Schiebel
aus Kirchheimbolanden

Tag der mündlichen Prüfung:	20.10.2017
Referent:	Prof. Dr. Thomas Leisner
Korreferent:	Prof. Dr. Corinna Hoose

Abstract

Only a minor, but strongly temperature and humidity dependent fraction of atmospheric aerosol particles act as ice nucleating particles (INPs) and thereby induce primary ice formation in tropospheric clouds. This primary formation of the ice-phase is often followed by secondary ice multiplication processes, and thereby markedly influences cloud radiative properties as well as the formation and distribution of precipitation. Mineral dust aerosols originating from dry and vegetation free desert sources are considered to significantly contribute to the abundance of atmospheric INPs. More recent investigations have shown that arable soil dust has an enhanced ice nucleation activity compared to this predominantly pure mineral dust probably because of its content of soil organic matter and biological material. It is the major subject of this thesis to comprehensively investigate the sources for this enhanced ice nucleation of soil dust dominated aerosol, and to quantify the ice nucleation activity for a selection of soil dust samples of relevance for the atmospheric aerosol.

The laboratory investigations presented in this study made use of the AIDA (Aerosol Interactions and Dynamics in the Atmosphere) cloud chamber to study the immersion freezing and deposition nucleation behavior in the temperature range between 190 K and 256 K. Four different soil dust samples were used for the cloud simulation experiments and were additionally characterized with other offline and online INP measurement methods. After dispersing the dry dust samples into the AIDA chamber, aerosol filter samples were, for example, taken and shipped to the Max Planck Institute for Chemistry for INP analysis with their MINA (mono ice nucleation assay) instrument. The new laboratory based continuous flow diffusion chamber INKA (Ice Nucleation instrument of the KArlsruhe Institute of Technology) was built as part of this thesis in collaboration with the Colorado State University (CSU), and was used for immersion freezing measurements with the same aerosols as used in the AIDA experiments. The advantage of INKA are fast automated scans of the aerosol ice nucleation behavior at well controlled temperatures (213 K to 263 K) and relative humidities.

Another instrument for INP measurements, that was developed as part of this thesis in cooperation with CSU is the Ice Nucleation SpEctrometer of the Karlsruhe Institute of Technology (INSEKT) that adopted the design of the CSU Ice Spectrometer instrument (CSU-IS). INSEKT was used for measuring the temperature dependent INP concentration in aerosols sampled from both the AIDA chamber and a field site in Cyprus during the A-LIFE campaign in April 2017. The advantage of this method is its high sensitivity for INP measurements, thereby extending and complementing the AIDA and INKA data to higher temperatures and providing concentrations of atmospheric INPs in a wide temperature range from

248 K to about 268 K. The INSEKT development was motivated by, and strongly benefited from two research stays at the CSU from July 2015 to October 2015 and from August 2016 to September 2016. The first research stay included the participation in a field campaign at the SPL (Storm Peak Laboratory) in September 2015, which was part of the Fifth International Workshop in Ice Nucleation (FIN). During this field campaign, atmospheric INP concentrations where measured with the CSU-IS at temperatures between 246 K to about 268 K. Further, the CSU-IS was used to measure INP temperature spectra of aerosols collected from the AIDA chamber as well as of atmospheric aerosols sampled at the Cyprus Atmospheric Observatory (CAO) during the INUIT-BACCHUS-ACTRIS campaign in April 2016.

The laboratory experiments were analyzed in terms of the so-called ice nucleation active surface site (INAS) density as a function of temperature, whereas for the field experiments temperature-dependent spectra of the INP concentrations were obtained. The laboratory and field measurements in the mixed-phase cloud regime, for temperatures between 243 K and 268 K, show two distinct regimes in the temperature spectrum of INP concentrations or INAS densities. Below 253 K, the ice nucleation activity follows an exponential temperature dependence with only a small variability between different samples. Heat and hydrogen peroxide treatment has almost no effect, indicating that the ice nucleation activity in this regime is dominated by mineral dust particles. At temperatures above 253 K, the ice nucleation activity varies largely between the individual samples. Heat and hydrogen peroxide treatment reduce the ice nucleation activity, clearly demonstrating the important contribution of heat-sensitive or chemically reactive organic compounds to the ice nucleation activity of multi-component soil dust aerosols at temperatures above 253 K.

A day with high mineral dust aerosol concentrations during the INUIT-BACCHUS-ACTRIS campaign provided a unique opportunity to sample and analyze the INP temperature spectrum of atmospheric mineral dust aerosol. The INP concentration followed an exponential temperature dependency over the entire temperature range (246 K to 265 K) and was independent of the applied heat and hydrogen peroxide treatment. This result underlines the conclusion that mineral dust particles mainly contribute to the atmospheric INP abundance at lower mixed-phase cloud temperatures.

Laboratory measurements in the cirrus cloud regime below about 238 K indicate that the ice nucleation activity of soil dust aerosol in this regime is independent of the soil organic matter content. A series of deposition nucleation experiments with one soil dust sample showed u-shaped isolines of the INAS density parameter in the temperature-saturation ratio diagram, similar to recent literature results for pure mineral dust aerosols. The here investigated soil dust is more ice active at low ice supersaturations than pure mineral dust aerosols investigated in previous AIDA studies.

Contents

1. Introduction

Pure water can remain liquid at temperatures well below its freezing point (Pruppacher, 1995). In this metastable phase, it is called supercooled water. At a temperature below about 235 K, supercooled water freezes homogeneously, where the ice phase forms in the absence of a foreign particle directly from the supercooled water phase (Koop, 2004). Depending on the temperature and the supersaturation with respect to the ice phase, heterogeneous ice formation can also occur by one of the four different nucleation modes *deposition nucleation*, *immersion freezing*, *condensation freezing* or *contact freezing* (Pruppacher and Klett, 1997; Cantrell and Heymsfield, 2005; Hoose and Möhler, 2012; Murray et al., 2012; Vali et al., 2015). Here, freezing is initiated by foreign particles, so-called ice nucleating particles (INPs).

In the atmosphere, INPs are very rare: Common INP concentrations are only 1 to 100 out of 10^6 total aerosol particles (Seinfeld and Pandis, 2016). In tropospheric clouds, INPs cause primary ice formation, which may be followed by secondary ice multiplication processes, and thereby markedly influences cloud radiative properties as well as the initiation and distribution of precipitation. Atmospheric INPs are, for example, mineral dust particles (DeMott et al., 2003a,b; Cziczo et al., 2013; Atkinson et al., 2013), volcanic ash particles (Hoyle et al., 2011; Steinke et al., 2011; Bingemer et al., 2012) or primary biological particles such as bacteria, fungal spores or pollen (Möhler et al., 2008; Iannone et al., 2011; Després et al., 2012; Fröhlich-Nowoisky et al., 2012; Augustin et al., 2013; Pummer et al., 2015).

Both laboratory and field studies contribute quantitative information on the ice activity of various atmospheric aerosol species. Laboratory studies allow for detailed investigations of individual aerosol species for their ice nucleation properties under well-controlled conditions. Field studies are affected by spatial and temporal changes of measurement conditions, but deliver important and direct information on the abundance and variability of the actual INP concentrations present in the atmosphere. Although there exist already many ground-based measurements of atmospheric INPs (DeMott et al., 2003b; Ardon-Dryer and Levin, 2014; Boose et al., 2016b; Mason et al., 2016), there is still a lack of long-term measurements on the global scale since most studies were only conducted during time-limited measurement campaigns in Northern America or in Europe. In addition, for the understanding of atmospherically relevant processes, it is of great interest to measure INP concentrations and chemical compositions of IPRs (ice particle residuals) in a height where clouds are actually forming. Such measurements can either be conducted on high altitude measurement stations, which sometimes are inside clouds (Chou et al., 2011; Boose et al., 2016a; Lacher et al., 2017; Schmidt et al., 2017), by aircraft measurements (Rogers et al.,

1998; Prenni et al., 2009; Cziczo et al., 2013) or by aerosol particle collection with unmanned aircraft systems (UAS) and offline INP analysis (Schrod et al., 2017). As a result, laboratory ice nucleation and atmospheric INP measurements contribute to better formulate and predict primary ice formation in cloud, weather and climate models (e.g., Ullrich et al. (2017); DeMott et al. (2010)) and also contribute to improve the model formulation of cloud processes and properties.

There are various different INP measurement methods available, which can be assigned to two groups: the so-called online methods investigate the sampled aerosol immediately at the sampling site, while offline methods collect aerosol particles on substrates or by immersion in liquids and investigate their ice nucleation activity afterwards. Examples for online methods are controlled expansion cloud chambers (Möhler et al., 2003), CFDCs (continuous flow diffusion chambers; Rogers (1988); Stetzer et al. (2008)) or CFMCs (continuous flow mixing chambers; Bundke et al. (2008)). Typical offline methods are cold stage based droplet freezing arrays (Wright and Petters, 2013; O'Sullivan et al., 2014; Budke and Koop, 2015), freezing arrays (Hill et al., 2014, 2016; Fröhlich-Nowoisky et al., 2015; Beall et al., 2017) and low pressure diffusion chambers (Schrod et al., 2016). In addition, there are instruments available, with which single droplets of aerosol suspensions can be investigated, for example in the electrodynamic balance (Rzesanke et al., 2012; Hoffmann et al., 2013) or in acoustic levitators (Diehl et al., 2014). Further, some methods are able to measure the INP content of size-selected aerosol particles (Mason et al., 2015). The increasing number of new INP measurement methods during the last years resulted in the need for intercomparison studies both in the laboratory under constant and known conditions (DeMott et al., 2011; Hiranuma et al., 2015; Wex et al., 2015; DeMott et al., 2017b) as well as in the field with the actual level and variability of ambient INP concentrations (DeMott et al., 2017a; Kanji et al., 2017).

Mineral dust aerosols, mostly originating from deserts, are known to be an important source for atmospheric INPs. Recent laboratory investigations have shown that agricultural soil dust has an enhanced ice nucleation activity by up to a factor of 10 compared to desert dust, especially at temperatures above 247 K (Steinke et al., 2016). This enhancement appears to be caused by very ice-active primary biological particles, such as bacteria, fungal spores and pollen, and their cell-free proteins and other macromolecules (Hoose and Möhler, 2012; Fröhlich-Nowoisky et al., 2012; Pummer et al., 2015). Further, in contrast to desert dust particles, arable soil dust aerosol also contains a considerable amount of organic matter, derived from plants and the soil microflora, which was shown to contribute to the ice nucleation activity (O'Sullivan et al., 2014; Tobo et al., 2014; Hill et al., 2016).

To be able to assess the influence of soil dust aerosols on atmospheric cloud formation, there is a need for more detailed information on the amount and origin of its ice nucleation behavior. For this purpose, comprehensive laboratory investigations as well as field measurements have been conducted as part of this thesis. In addition to comprehensive experiments with the AIDA (Aerosol Interactions and Dynamics in the Atmosphere) cloud chamber, two new instruments for laboratory ice nucleation studies

and atmospheric INP measurements were successfully developed and built during this thesis, in close collaboration with the Colorado State University in Fort Collins, USA: the new laboratory-based ice nucleation instrument of the Karlsruhe Institute of Technology (INKA) and the new freezing array ice nucleation spectrometer of the Karlsruhe Institute of Technology (INSEKT). Field INP measurements were performed at three different sites, the Storm Peak Laboratory (SPL) close to Steamboat Springs, Colorado, the Cyprus Atmospheric Observatory (CAO) near Agia Marina, and a site close to the airport Paphos, Cyprus. For both the laboratory and field studies, different sample treatments have been applied to investigate the contribution of heat-sensitive and organic-rich INPs on the ice nucleation activity of soil dust dominated aerosols and to thus gain information on their origin.

This thesis is structured as follows:

Chapter 2 will introduce soil dust emission mechanisms and the different ice nucleation processes in the atmosphere.

Chapter 3 will describe the aerosol preparation and characterization in the laboratory and in the field, and introduce the different INP measurement methods used in this thesis: the cloud simulation chamber AIDA, the laboratory ice nucleation instrument INKA and the freezing arrays INSEKT, CSU-IS and MINA.

Chapter 4 will present comprehensive laboratory investigations on the ice nucleation activity of arable soil dust aerosol in the mixed-phase and in the cirrus cloud regime including systematic investigations on the contribution of soil organic matter and primary biological components on the ice nucleation activity of arable soil dust.

Chapter 5 will describe and discuss INP concentration measurements in the Mediterranean, influenced by both organic/biological and mineral dust aerosol species. The results will also be compared with predictions using laboratory based INP parametrizations and with INP measurements conducted at other locations and with other methods.

Chapter 6 will summarize the findings of the laboratory and the field studies on the ice nucleation activity of arable soil dust aerosols.

2. Theoretical Background

2.1. Atmospheric Aerosol Particles

Aerosol particles are fine solid or liquid particles suspended in air (Whytlaw-Gray et al., 1923) with sizes between about 0.01 µm and 10 µm. Atmospheric aerosol particles can be emitted either by anthropogenic or by natural sources. Natural sources are, for example, wind dispersion (soil dust, biological particles), sea spray, volcanic eruptions (ash, minerals) or wildfires (soot). Among others, anthropogenic sources are industry or air and road traffic, which lead to the emission of soot and other particles into the atmosphere. Besides primary aerosol particles, that are directly emitted into the air, there are also secondary particles, which are formed in the atmosphere by the nucleation of precursor substances. Precursor sources may also be of anthropogenic or natural origin. An example of an important atmospheric secondary aerosol component is sulfuric acid (H_2SO_4), which is formed due to aerosol nucleation (Curtius, 2006) from the gaseous precursor sulfur dioxide (SO_2) (Roedel and Wagner, 2011). More recent experiments at the CERN-CLOUD chamber have demonstrated the role of some organic species for new particle formation and growth in the atmosphere (Kirkby et al., 2016; Tröstl et al., 2016).

The different aerosol sources and processes result in a multimodal distribution of the atmospheric aerosol (Whitby, 1978). The so-called *aitken mode* consists of particles with diameters between 0.01 µm and 0.1 µm, the *accumulation mode* between 0.1 µm and 1 µm and the *coarse mode* between 1 µm and 10 µm. The *nucleation mode* consists of particles smaller than 0.01 µm which grow very fast into the next modes. Coarse mode aerosol typically origins from primary particle emissions and is thus the most relevant mode for this thesis.

The abundance of the different atmospheric aerosol species strongly depends on factors such as the nucleation rate, the spatial and temporal emission as well as on their lifetime in the atmosphere. During their residence time in the atmosphere, the aerosols undergo physical and chemical changes. Condensation and coagulation changes their size, while aging by coating with, for example, sulfate or organics, changes their chemical composition and surface properties, the latter might also modify their ice nucleating properties. Removal of aerosol particles occurs either by dry deposition caused by settling, molecular or turbulent diffusion, or by wet deposition via scavenging through clouds or precipitation. The wet deposition can be either initiated due to activation of the aerosol particle as cloud condensation nuclei (CCN) or ice nucleating particle (INP), or due to coagulation of the aerosol particle with a hydrometeor (i.e. droplet or ice particle).

2.2. Ice Formation in the Atmosphere

Depending on the temperature and the supersaturation over ice, primary ice formation can either occur homogeneously or by one of the four different modes of heterogeneous ice nucleation *deposition nucleation*, *immersion freezing*, *condensation freezing* or *contact freezing* (Pruppacher and Klett, 1997; Cantrell and Heymsfield, 2005; Hoose and Möhler, 2012; Murray et al., 2012; Vali et al., 2015), which are initiated by atmospheric INPs (Fig. 2.1).

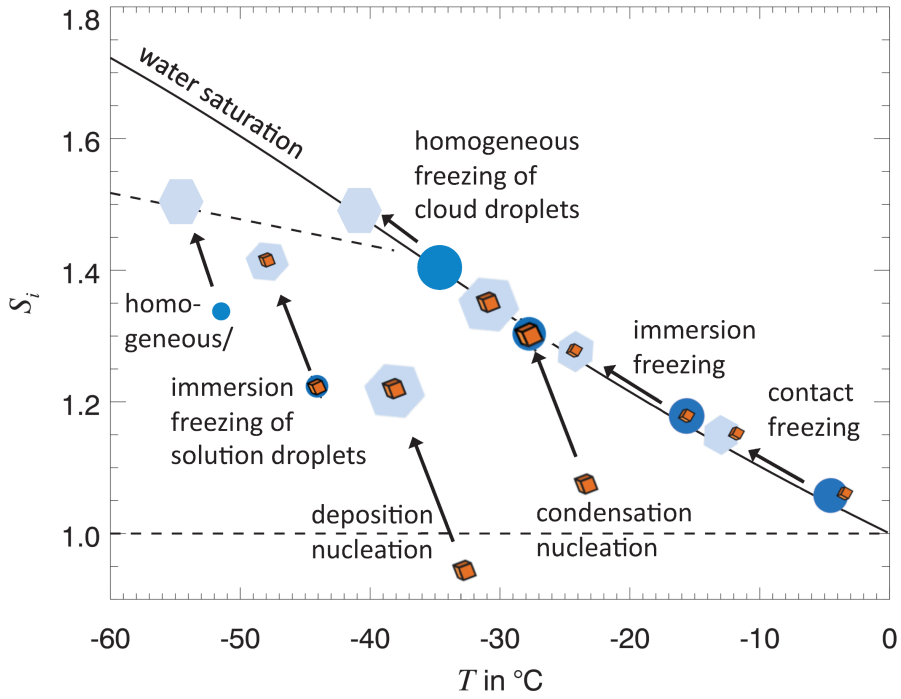

Fig. 2.1.: Schematic of the different ice nucleation processes in the atmosphere as function of temperature T and ice saturation S_i, from Hoose and Möhler (2012).

Homogeneous freezing describes the process, where the ice nucleation is initiated by the formation of a solid ice-like cluster of critical size (germ) inside a pure liquid water droplet.

Deposition nucleation means that the ice supersaturated water vapor nucleates on the INP surface directly from the gaseous to the solid state. The environment during the deposition nucleation process is subsaturated with respect to liquid water.

Immersion freezing is triggered by an INP, which is already immersed in the droplet before the nucleation starts, but did not necessarily act as CCN before.

Condensation freezing occurs at supersaturation with respect to liquid water and a temperature below the melting point of water. Here, an aerosol particle acts as CCN and directly triggers freezing of the condensing water.

Contact freezing describes the ice formation process, where the collision of an INP with a supercooled water droplet initiates freezing, which starts from the contact point.

Marcolli (2014) suggested that what is considered deposition nucleation can be interpreted in many cases also as homogeneous or immersion freezing of water that condensed in pores and cavities. Due to the inverse Kelvin effect, water may form in voids and cavities well below liquid water saturation. The pore diameter thereby determines the required water vapor saturation ratio. For temperatures below 235 K, homogeneous freezing would occur when at least one pore is filled with a sufficient amount of water to form the critical germ. The so-called pore condensation and freezing (PCF) mechanism may also occur in the immersion freezing regime, when at least one pore contains water and an active site. Recent laboratory experiments have demonstrated the PCF mechanism to occur not only on designed particles with pre-described pore sizes, but also on some atmospherically relevant aerosol types (Wagner et al., 2016).

2.2.1. Classical Nucleation Theory[1]

The classical volume-dependent nucleation theory describes the germ formation of a new phase and can be adapted to the heterogeneous ice nucleation (Pruppacher and Klett, 1997). The phase transition from the liquid to the solid phase of water is a first-order phase transition. Pure water can remain liquid, in a metastable supercooled phase, at temperatures below its melting point because it has to overcome an energy threshold before it can form the thermodynamically stable, crystalline phase (Kalikmanov, 2013). In case of immersion freezing, this energy barrier consists of a nucleation energy term F_g and a molar activation energy term g^+:

$$\Delta E = \Delta F_g + \Delta g^+ \qquad [2.1]$$

For deposition nucleation, it is equal to the nucleation energy.

Nucleation Energy

The free energy of the germ of the ice phase is the total of a surface contribution and a contribution from the bulk (Fig. 2.2). For small numbers of molecules and therefore for smaller germ sizes the contribution of the surface dominates. In this regime the dissociation of molecules is more likely. The growth of the germ is thereby a reversible process since both random incorporation and detachment of molecules occur simultaneously.

Above a critical number of molecules and thereby at a critical germ size the bulk outweights the surface contribution due to the decreasing surface-to-volume ratio of the germ with increasing size. This critical size of the germ defines the required free energy barrier between the liquid and the solid phase, which is equal to the free energy of germ formation ΔF_g. At this critical germ size, the growth and therefore

[1] Some elements of this section are adapted with changes from the author's diploma thesis (Schiebel, 2014).

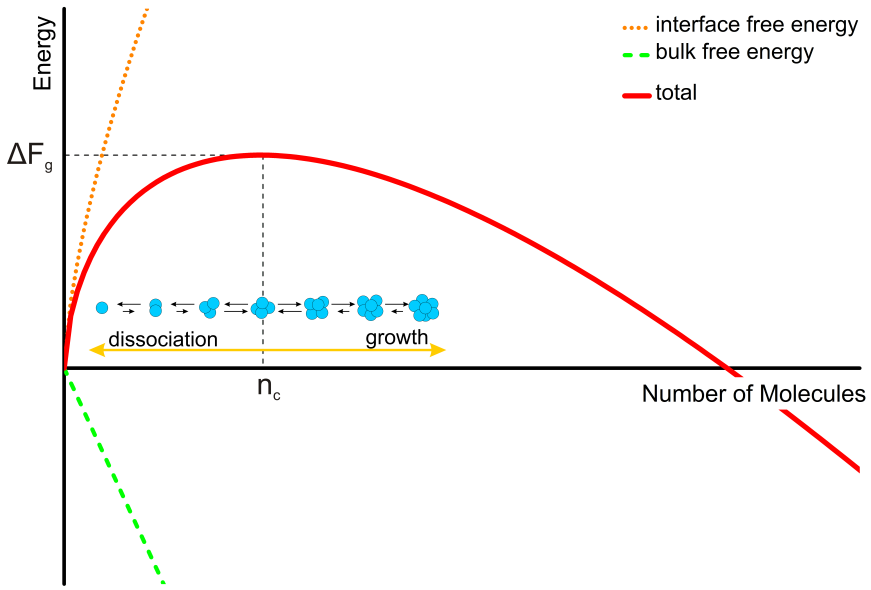

Fig. 2.2.: Schematic of the total free energy of the ice germ (red solid line) with the contribution of the interface (orange dotted line) and the bulk (green dashed line) versus the number of molecules of the germ. For small numbers of molecules the dissociation is more likely. Above a critical number of clusters and therefore above a critical cluster size, the growth becomes energetically favorable. From Schiebel (2014), adapted from Vali (1999).

the nucleation process becomes more energetic favorable than its decay. The critical size is a function of the supercooling. With decreasing temperatures the average number of molecules per cluster increases within liquid water (Némethy and Scheraga, 1962). Thereby the probability of the spontaneous formation of a cluster with critical size due to local fluctuations in temperature and density increases. This germ of the new phase grows until it becomes an ice particle.

Molar Activation Energy

The second energy barrier to nucleation is the molar activation energy Δg^+. This energy is required to pass a water molecule from its energetic equilibrium position in the supercooled water droplet to the equilibrium position in the ice germ (Pruppacher and Klett, 1997). This process includes the breaking of the already existing molecular bonds to the metastable liquid phase, the transfer to the germ interface and the creation of a new bond to the ice phase. Since the pressure and the temperature are assumed to be constant during this process, Δg^+ can also be identified as the molar Gibbs free enthalpy. For a long time Δg^+ had been defined as the activation energy for self-diffusion in water $(\Delta g)_{act,w}$. Experimental obtained data however showed that this assumption leads to an underestimation of the ice nucleation rate for temperatures below 240 K (Hagen et al., 1981; DeMott and Rogers, 1990). The reason for these discrepancies is the rapid increase of $(\Delta g)_{act,w}$ for decreasing temperatures below 240 K while experimental results suggest a strongly deceasing Δg^+ for decreasing temperatures (Hagen et al., 1981). Reasons for

this might be that at such low temperatures not only single molecules but whole clusters overcome the phase transition which means that not every single bond of a cluster needs to be broken before the cluster becomes part of the ice germ. Since Δg^+ is not directly measurable in the low temperature regime of heterogenous freezing, it needs to be determined in other ways, e.g. Pruppacher (1995) calculated it with the help of experimentally obtained ice nucleation rates.

Ice Nucleation Rates

The nucleation rate $J_{imm,dep}$ describes the formation of stable germs of the new phase per time and can be calculated with the following equation (Cantrell and Heymsfield, 2005; Pruppacher and Klett, 1997):

$$J_{imm}(T) = A_{imm}\, exp\left(-\frac{\Delta g^+}{kT} - \frac{\Delta F_g f}{kT}\right) \quad [2.2]$$

$$J_{dep}(T) = A_{dep}\, exp\left(-\frac{\Delta F_g f}{kT}\right) \quad [2.3]$$

$A_{imm,dep}$ is the kinetic prefactor (e.g. Zobrist et al. (2007)) and $k = 1.3806488 \times 10^{-23}\,\mathrm{J\,K^{-1}}$ is the Boltzmann constant. For heterogeneous ice nucleation, the geometric term f lowers the energy barrier compared to homogeneous freezing due to the influence of the substrate (e.g. Ickes et al. (2017)). This equation provides a closed-form expression but it requires the knowledge of some properties of water as function of the temperature. Especially, the calculation of the energy barrier includes a number of uncertain parameters like the interface tension between the supercooled liquid and the ice phase or the activation energy. For the metastable phase of supercooled water, there is often no data available. What is done instead, is to extrapolate data acquired above the melting point. There exist several on classical nucleation theory based formulations which use different approaches to derive the unknown parameters. This leads to variations of several orders of magnitudes in the properties of water, such as the activation energy or the interface tension (Hoose and Möhler, 2012; Ickes et al., 2015). In addition, the classical nucleation theory does not account for the complexity of natural aerosol particles. In recent years, several approaches have been established to compensate for these limitations. One example is the *soccer ball model* introduced by Niedermeier et al. (2011). Here, the aerosol particles are treated as complex particles, which can be covered by different active sites. The nucleation process of each of these sites follows the classical nucleation theory. Another example is the *active surface site approach* (Connolly et al., 2009; Niemand et al., 2012; Ullrich et al., 2017), which will be explained in more detail in the following chapter.

2.2.2. Active Surface Site Approach

The active surface site approach assumes that the ice nucleation process is independent of the time and occurs at specific active sites on the particle surface. These active sites nucleate ice at an individual temperature and with an individual probability, whereby the most ice active one initiates the ice nucleation process.

The approach has originally been developed for immersion freezing. The number of formed ice crystals $N_{ice,i}$ in the monodisperse size bin i is described as follows (Connolly et al., 2009; Niemand et al., 2012):

$$N_{ice,i} = N_{all,i} \left[1 - exp\left(-s_{single,i}\, n_s(T)\right)\right] \quad [2.4]$$

$N_{all,i}$ is the number of all particles in the size bin i, $s_{single,i}$ is the particle surface area of this single size bin and $n_s(T)$ is the density of ice active surface sites.

For polydisperse aerosol size distributions, the formed ice particles and the available aerosols in the individual size bins have to be summed up:

$$\sum_i N_{ice,i} = \sum_i N_{all,i} \left[1 - exp\left(-s_{single,i}\, n_s(T)\right)\right] \quad [2.5]$$

For small ice fractions $s_{single,i}\, n_s(T) \ll 1$ the equation can be approximated as follows:

$$\sum_i N_{ice,i} \approx \sum_i N_{all,i}\, s_{single,i}\, n_s(T) = n_s(T) \sum_i N_{all,i}\, s_{single,i} \quad [2.6]$$

Rearranging results in the following simplified expression for the ice nucleating active surface site density $n_s(T)$:

$$n_s(T) = \frac{\sum_i N_{ice,i}}{\sum_i N_{all,i}\, s_{single,i}} = \frac{\sum_i N_{ice,i}}{\sum_i s_{aero,i}} = \frac{N_{ice}}{s_{aero}} \quad [2.7]$$

This equation allows to calculate the INAS density from the measured ice number N_{ice} and the total available aerosol surface s_{aero}.

The active surface site approach has also been adopted to formulate deposition nucleation (e.g.Hiranuma et al. (2014); Ullrich et al. (2017)), where the ice nucleation process is temperature- as well as humidity-dependent.

3. Experimental Methods

During this thesis, ice nucleating particle (INP) measurements were conducted in the laboratory as well as in the field (Sec. 3.1). Especially laboratory investigations allow a combination of different INP measurement techniques to study the ice nucleation ability over wide temperature and humidity ranges. One of the here used laboratory methods is the well-established Aerosol Interactions and Dynamics in the Atmosphere (AIDA) cloud simulation chamber (Sec. 3.2). The continuous flow diffusion chamber INKA expands the measurement capacity of the AIDA facility with automated relative humidity (RH) scans at pre-selected constant aerosol temperatures (Sec. 3.3) and thereby gives additional information on the humidity dependence of the ice nucleation activity. The freezing array INSEKT contributes additional information on the temperature dependence of the ice nucleation behavior (Sec. 3.4). This method extends the temperature range of AIDA and INKA to higher temperatures because it is sensitive to relatively low INP number concentrations. Therefore, INSEKT is also well suited for atmospheric INP measurements where the INP concentrations can be rather low, in particular at higher temperatures.

3.1. Aerosol Preparation

This Section will describe the methods for generating and characterizing the aerosols under investigation during the laboratory experiments (Sec. 3.1.1) as well as the methods for sampling atmospheric aerosol particles during field campaigns (Sec. 3.1.2). Further, the different aerosol treatment methods with heat (Sec. 3.1.3) and hydrogen peroxide (Sec. 3.1.4) will be described.

3.1.1. Aerosol Generation and Characterization in the Laboratory

Before natural soil dust samples (Sec. 4.2) are investigated in the laboratory, they are dried and sieved ($<75\,\mu m$). A rotation brush generator (PALAS, RBG1000) aerosolizes and deagglomerates the soil samples. The thus generated aerosol is then injected into the $84\,m^3$ AIDA or into the $4\,m^3$ aerosol preparation and characterization (APC) chamber (Fig. 3.1). Depending on the aim of the experiment, the aerosol can be optionally channeled through inertial cyclone impactors before entering the chamber. This removes particles larger than $5\,\mu m$.

Inside the chambers, the aerosol is measured with a similar set of aerosol number concentration and size distribution experiments.

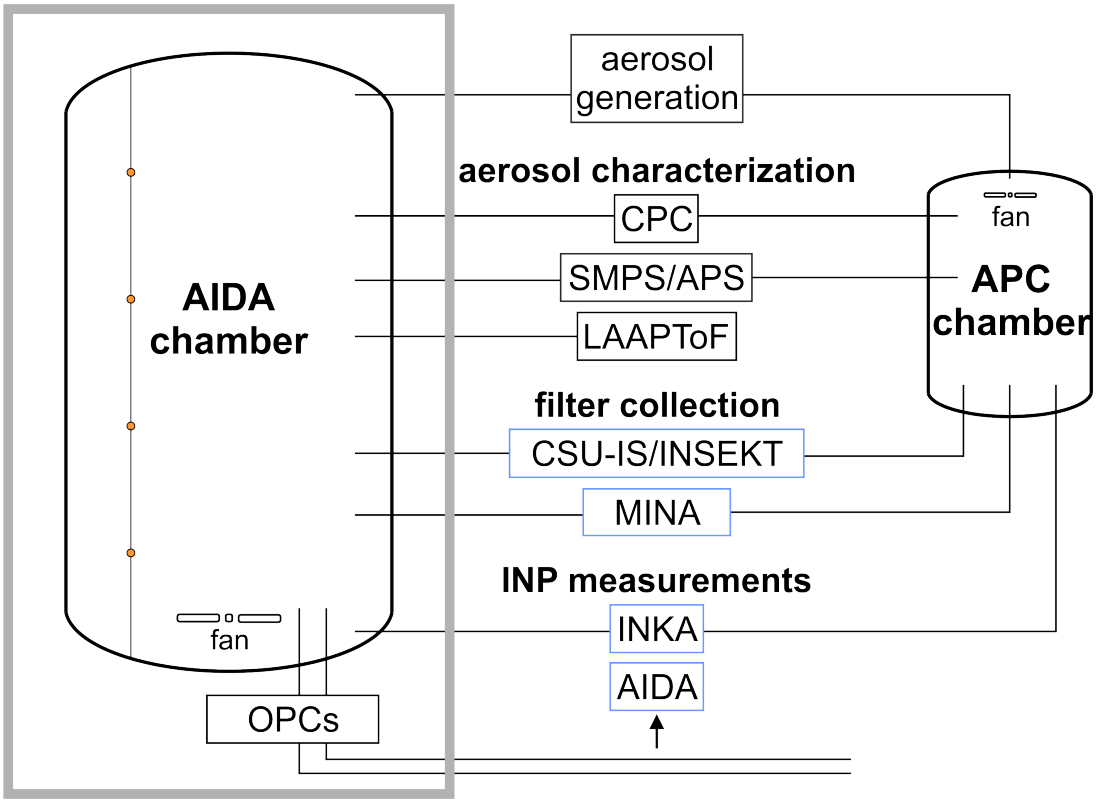

Fig. 3.1.: Schematics of the AIDA cloud chamber with aerosol generation and characterization instruments. The aerosols under investigation are either added to the AIDA cloud simulation chamber or the APC chamber. From there, the aerosol is sampled by different instruments to measure the number concentration, size distribution, and chemical composition, and is collected on filters and other substrates for offline analysis methods.

The aerosol particle number concentration is detected by a condensation particle counter (CPC). This instrument continuously samples the aerosol from the chamber via a horizontal sampling line. The sampled air is first saturated with butanol in an environment with a slightly increased temperature and then transferred into the colder condensation unit of the instrument, where the butanol vapor condenses on the particles. Due to condensational growth, the built droplets are large enough to be detected by an optical particle counter (OPC). With this measurement technique the instrument is able to detect particles with diameters as small as 0.01 µm and with number concentrations of up to 10 000 cm^{-3} (in case of the CPC3010 connected to AIDA, TSI (2002)).

The aerosol size distribution is measured with a combination of a scanning mobility particle sizer (SMPS) and an aerodynamic particle sizer (APS). The SMPS measures the size distribution of aerosol particles with mobility diameters between 0.014 µm and 0.82 µm. To ensure a known charge distribution, the instrument first exposes the sampled aerosol particles (horizontal sampling line) to a bipolar charge (TSI, 2009) (Kr85). Then, the particles are size selected with a differential mobility analyzer (DMA) and the particle number concentration of the size binned particles is measured with a CPC. The APS detects

larger aerosol particles with an aerodynamic diameter between 0.523 µm and 19.81 µm. The instrument is a time-of-flight spectrometer that exposes the sampled aerosol particles (horizontal sampling line) to an accelerating flow of sheath air (TSI, 2012). The velocity of the accelerated particle gives then information on the particle size. In order to cover the full aerosol size range, the measurement of both instruments needs to be combined. However, the mobility and aerodynamic diameters are only equal for spherical particles of unit density (ρ_0= 1 g cm^{-3}). Because the dust particles under investigation here are not spherical and have a density ρ_p different from unity, the mobility diameter d_m as well as the aerodynamic diameter d_a are converted to a volume equivalent diameter d_{ve}, which is the diameter of a spherical particle that has the same volume and mean density of the actual a-spherical particle.

$$d_{ve} = \frac{d_m}{\chi} \quad [3.1]$$

$$d_{ve} = \sqrt{\frac{\chi \rho_0}{\rho_p}}\, d_a \quad [3.2]$$

where χ is the so-called dynamic shape factor (DeCarlo et al., 2004).

From the measured size distribution of the particle number concentration $c_{n,aero}(log\, d_{ve})$, the aerosol surface area concentration size distribution $c_{s,aero}(log\, d_{ve})$ can be derived as follows with the assumption of spherical particles (Fig. 3.2):

$$c_{s,aero}(log\, d_{ve}) = \pi\, d_{ve}^2\, c_{n,aero}(log\, d_{ve}) \quad [3.3]$$

d_{ve} is thereby the volume equivalent aerosol particle diameter (Eq. 3.1 and 3.2).

The total aerosol surface concentration $c_{s,aero}$ is of great interest for the investigations of heterogeneous ice nucleation. It can be either derived by summing up the surface concentration (Eq. 3.3) of the single size bins in the SMPS and APS data, or it can be calculated from the parameters of a lognormal fit to the measured size distribution:

$$c_{s,aero} = \pi\, c_{n,aero}\, exp\left(2\, ln\, d_{p,m} + 2\, ln^2\, \sigma_g\right) \quad [3.4]$$

where $c_{n,aero}$ is the total number concentration. $d_{p,m}$ is the median diameter and σ_g the geometric standard deviation of the lognormal fit.

During most experiments, single aerosol particles were also analyzed with a laser ablation aerosol particle time-of-flight mass spectrometer (LAAPTOF) (Aeromegt GmbH) (Gemayel et al., 2016; Shen et al., 2017). The compact single particle mass spectrometer is able to online measure the size, chemical composition, and mixing state of individual aerosol particles in the size range of 0.3 µm to 2.5 µm. Positive and negative ion mass spectra are typically recorded for several hundred individual particles prior to the AIDA expansion experiment. In addition to the total aerosol, in some cases, ice particle residuals (IPRs) have been characterized during the experiment. Also, for some experiments, the remaining aerosol particles were investigated after the cloud expansion experiment.

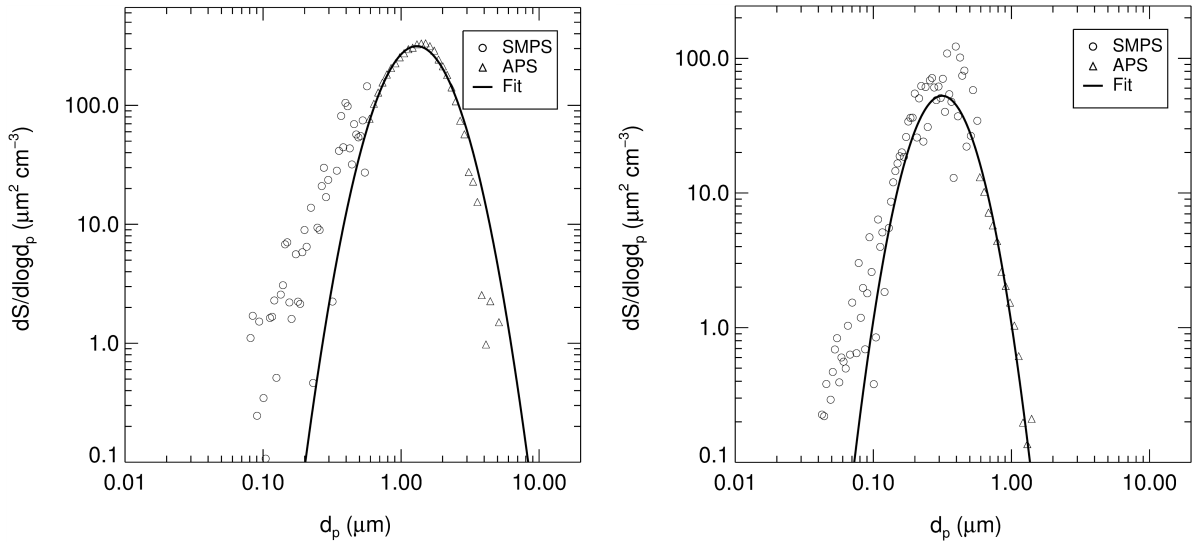

(a) Surface area distribution of an aerosol generated without the use of an inertial cyclone impactor.

(b) Surface area distribution of an aerosol generated with the use of an inertial cyclone impactor.

Fig. 3.2.: Measured aerosol surface concentration size distributions of the German soil dust collected in Gottesgabe. The combination of the two different measurement methods, the SMPS (circles) and the APS (triangles), enables to detect a wide aerosol size range. The difference between (a) and (b) indicates the influence of using cyclones on the size of the generated aerosol particles.

Prior to the AIDA expansion experiment, the generated aerosol particles are collected on filters for several offline methods.

For offline INP measurements with INSEKT and Colorado State University Ice Spectrometer (CSU-IS) (Sec. 3.4), aerosol containing chamber air is pumped through horizontally connected stainless steel filter holders (Sartorius Membranfilter GmbH, SM16254, with modified connections). The holders are thereby equipped with a 47 mm Nuclepore track-etched polycarbonate membranes with 0.2 µm-diameter-pores (Whatman). To lower the background of INP counts from the filter material, they are pre-cleaned by soaking them in 10 % hydrogen peroxide (H_2O_2) for 10 min (see description of the CSU-IS procedure in the supplement of Hiranuma et al. (2015) for details). Afterwards, three rinses with 0.1 µm-pore-diameter-filtered deionized water (18 MΩ) ensures to remove the H_2O_2. The filters are then dried in a particle-free, laminar flow clean box and are stored individually in sterile aluminum envelopes until they are used for the aerosol sampling. Total aerosol is sampled onto the filters with a flow rate of $10\,\mathrm{std1\,min^{-1}}$ for about 2 h. Then, the loaded filters are immediately stored individually packaged and sealed in a freezer until the aerosol is suspended with clean water (see Sec. 3.1.2 for details) and probed for its ice nucleation activity. The filters for analysis with the CSU-IS have been shipped on dry ice to CSU before the particles were suspended.

For additional INP measurements, particles are also collected for the offline method mono ice nucleation assay (MINA) (Sec. 3.4). For this purpose, sample air is sampled through a 47 mm quartz fiber filter, mounted in the same filter holders as used for the INSEKT and CSU-IS filter collection. The filters

are pre-cleaned by a heat treatment at 673 K. Chamber air is filtered with a flow rate of 20 std l min^{-1} for about 2 h. The filters are then stored individually packaged and frozen. For the INP analysis with MINA, the filters were shipped on dry ice to the Max Planck Institute for Chemistry (MPIC).

Also, aerosol particles are collected for environmental scanning electron microscope (ESEM) analysis. For this purpose, a sample air flow of 2 std l min^{-1} is pumped through a horizontally connected stainless steel filter holder (Sartorius Membranfilter GmbH, SM16251, with modified connections) for 30 min. This filter holder is mounted with a 25 mm Nuclepore filter. The collected filters are stored individually packaged at room temperature until they are analyzed with the ESEM.

The online INP measurement method INKA (Sec. 3.3) is also able to investigate the total aerosol from the AIDA or the APC chamber. For this purpose, the instrument is connected to the chambers via a horizontal sampling line and samples the aerosol containing chamber air with 0.63 l min^{-1} to 1.25 l min^{-1} for about 4 h. When the particle collection and sampling is finished, the actual AIDA cloud expansion experiment (Sec. 3.2) is conducted, which is also an online INP measurement.

With this setup, the generated aerosol particles are well-characterized by various different instruments which are all sampling from the same aerosol source. Especially for combining the different INP measurement methods, this is of great relevance in order to rule out differences due to different aerosol generation methods.

3.1.2. Aerosol Sampling and Characterization in the Field

During field measurements, ambient aerosol particles are collected on filters, e.g. at the Cyprus Atmospheric Observatory (Fig. 3.3, picture on the left-hand side). In order to do this, a certain amount of

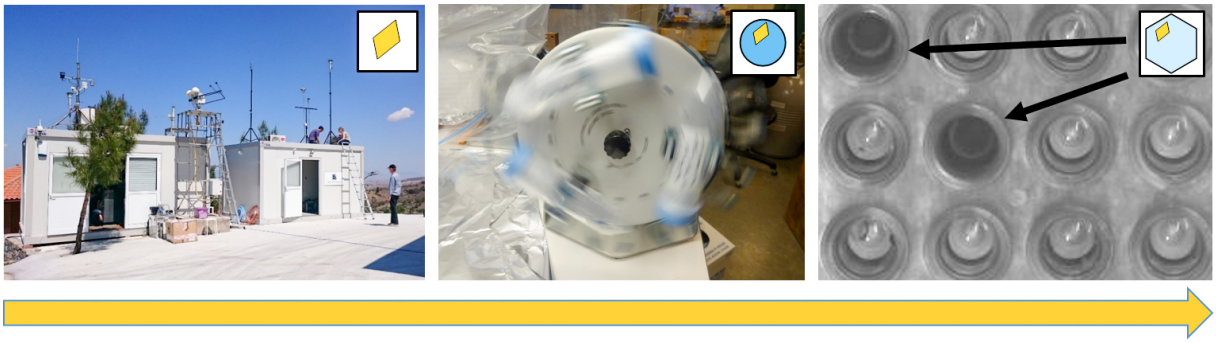

Fig. 3.3.: Illustration of the steps for atmospheric INP measurements. Atmospheric aerosol particles are collected on filters at certain field locations, e.g. at the CAO in Cyprus (left-hand side). Then the sampled aerosol particles are washed off the filters with clean water (middle, picture courtesy of Thomas C. J. Hill). Thereafter, small volumes of the resulting aerosol suspension are analyzed in an freezing array (right-hand side).

ambient air is pumped through a pre-cleaned 47 mm Nuclepore track-etched polycarbonate membrane

with 0.2 µm-diameter-pores (Whatman) (see Sec. 3.1.1 for details about the cleaning process), the same filters that were also used for the INSEKT and CSU-IS aerosol sampling during the AIDA experiments.

After particle collection, the samples are stored individually packaged and sealed in a freezer and are shipped or transported back to the laboratory. Here, the sampled aerosol particles are washed off the filter with clean water. For this purpose, the filter together with usually 8 ml of 0.1 µm-pore-diameter-filtered deionized water (18 MΩ) is filled into a sterile 50 ml polypropylene centrifuge tube (FALCON) and is tumbled for 30 min with 60 rpm on a rotator (Fig. 3.3, picture in the middle).

Small volumes of the so generated aerosol suspension (usually 50 µl) are pipetted into sterile, 96-well polypropylene polymerase chain reaction (PCR) trays (Life Science Products Inc. or BRAND, depending on the instrument) (Fig. 3.3, picture on the right-hand side). The PCR trays are then placed on a temperature controlled aluminum block and are continuously cooled while recording the increasing number of frozen wells. From this, the temperature dependent number concentration of INPs can be calculated for the respective suspensions (see Sec. 3.4 for details).

For the atmospheric INP measurements of this thesis, aerosol particles were sampled at three locations: The CAO, the temporary measurement station at the Airport Paphos and the Storm Peak Laboratory (SPL).

Cyprus Atmospheric Observatory (CAO)

Due to its location close to the Sahara Desert and the deserts of the Middle East, Cyprus is often influenced by mineral-dust-rich air masses. Especially during spring time, dust events are very likely. The Cyprus boundary layer aerosol is also influenced by marine sources due to the surrounding Mediterranean Sea. Anthropogenic emissions from Europe and the Middle East are also transported to the island. The CAO is located in the center of Cyprus (Fig. 3.4a, 35.04 °N, 33.06 °E, 535 m a.s.l.) at a remote side near Agia Marina. It is a rural background site in the foothills of the Troodos mountains (Fig. 3.4c). The station consists of two containers (Fig. 3.4b) which are equipped with instrumentation measuring meteorological parameters, such as the amount of rain (Department of Labour Inspection (DLI)) or the wind speed and direction (DLI), as well as with aerosol characterization instruments monitoring aerosol parameters, such as the mass concentration (DLI, PM2.5 and PM10 inlet).

At the CAO, atmospheric aerosol particles were collected during the INUIT-BACCHUS-ACTRIS campaign in April 2016. The goal of the four-week campaign was to investigate the influence of dust transport from the Sahara or the Middle East on the ambient INP concentration. In addition, a detailed series of INP measurements with good temporal resolution for the campaign period allows to elaborate the INP variability and a possible correlation with meteorological conditions. Further, the study focused on the intercomparison of field INP instruments and methods. For this purpose, two online and six offline INP measurement methods were measuring in a region and a season where dust events are very likely. During the campaign, two major dust events occurred. In addition to the standard instrumentation of the CAO, the INP measurements were accompanied with various further instrumentation characterizing the

(a) Map of Cyprus.

(b) Picture of the station.

(c) View from the station.

Fig. 3.4.: Cyprus Atmospheric Observatory (CAO).

aerosol particles. The INP results were related to the surface area concentration measured with the optical particle sizer (OPS, PM10 inlet, University of Frankfurt). The difference between the PM10 and the PM2.5 data (DLI) from the station was used to correlated the INP concentrations to the coarse particle mass load in the sampled aerosols.

Aerosol particles were collected on 0.2 µm pore diameter filters for immersion freezing analysis with the Ice Spectrometer of the Colorado State University (CSU-IS), similar to the aerosol sampling during the AIDA experiments (see Sec. 3.1.1). Here, the filter holder was connected to a PM10 aerosol particle inlet via a vertical sampling line. Ambient air was sampled with a flow rate of 16.7 l min^{-1} for about 8 h during daytime.

Temporary Measurement Station at the Airport Paphos[1]

The temporary measurement station, which was installed for the A-LIFE (absorbing aerosol layers in a changing climate: aging, lifetime and dynamics) campaign during April 2017, was located at the airport Paphos (Fig. 3.5a, 34.71 °N, 32.48 °E, 4 m a.s.l.) in Cyprus. Therefore, it was similar to the CAO influenced by mineral dust particles transported from the Sahara or the Middle East as well as by polluted

[1]The INP samples from this station were collected and analyzed by Barbara Dietel (see Dietel (2017)) and are used in the scope of this thesis for comparison to the INP measurements conducted at the CAO.

air masses from Europe or the Middle East. But the influence of marine aerosol particles can be higher in Paphos since it is situated directly at the coast to the Mediterranean Sea. Due to its location, the station might also be influenced by aircraft emissions.

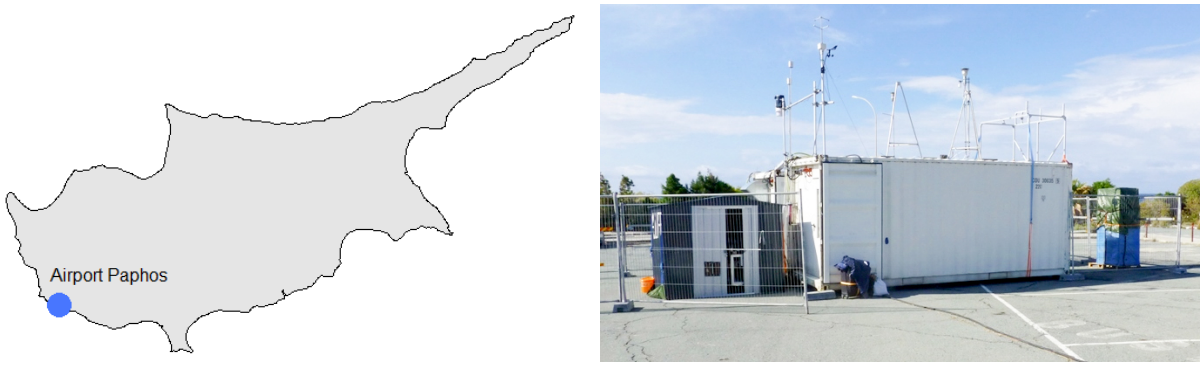

(a) Map of Cyprus. (b) Picture of the station.

Fig. 3.5.: Temporary measurement station at the airport Paphos. Picture of the station courtesy of Barbara Dietel.

At the Paphos station, aerosol samples were collected during the A-LIFE campaign (Dietel, 2017). The main goal of this three-week field campaign was to investigate the properties of absorbing mineral dust aerosols during their lifetime in the atmosphere. Therefore, this field measurements were located at a place and were conducted at a time where air masses with high dust levels are likely. During A-LIFE, aircraft measurements (Deutsches Zentrum für Luft- und Raumfahrt, University of Vienna) were combined with ground-based measurements of aerosol properties. These ground observations included aerosol LIDAR (light detection and ranging) measurements in Limassol (approx. 50 km from the airport Paphos) (TROPOS) and aerosol characterization measurements with two fully equipped containers at the airport Paphos (TROPOS, TU Darmstadt).

At Paphos (Fig. 3.5b), aerosol particles were collected on filters for offline immersion freezing analysis with INSEKT, similar to the aerosol sampling during the CAO campaign (see above). Ambient air was collected with a mean flow rate of $15.21\,\mathrm{min}^{-1}$ for 8 h during day and night time.

Storm Peak Laboratory (SPL)

The Desert Research Institute's Storm Peak Laboratory (SPL) is a permanent high altitude atmospheric research facility located in the Rocky Mountains of northwestern Colorado (Fig. 3.6, 40.46 °N, 106.74 °W, 3220 m a.s.l.) in the Routt National Forest (Borys and Wetzel, 1997). The mountain-top station is situated on a 70 km north-south mountain barrier perpendicular to the prevailing westerly winds coming from the Pacific. The research site allows for diverse measurement scopes. Under some conditions, it is in the local boundary layer and thereby influenced by the agricultural Yampa Valley as well as by the close-by town Steamboat Springs. Since the mountain range acts as upwind fetch, comprehensive in-cloud studies are possible as well. Due to its high altitude, the station also frequently allows for clear-air measurements

in the free troposphere without the influence of local emissions. The SPL is fully equipped with various instrumentation measuring the meteorological conditions as well as characterizing the aerosol.

(a) Map of the United States of America.

(b) Picture of the station.

(c) View from the station.

Fig. 3.6.: Storm Peak Laboratory (SPL).

At SPL, ambient aerosol particles were collected during the Fifth International Workshop on Ice Nucleation (FIN) part 3 in September 2015. The aim of the three-week field campaign was to compare various online and offline methods for INP measurements. This high elevation site provided a suitable platform to test the instruments and methods in a natural environment under various changing influences. The comprehensive INP measurements were supplemented by different aerosol characterization instruments, such as the PALMS instrument (particle analysis by laser mass spectrometry, MIT), the bioaerosol instrument WIBS (Wideband Integrated Bioaerosol Sensor, NOAA) and the black carbon (soot) detection instrument SP2 (Single Particle Soot Photometer, CSU and NOAA).

Ambient aerosol particles were collected on pre-cleaned filters for offline INP measurements with the CSU-IS. The 0.2 µm pore diameter filters were placed in sterile, single-used filter units (Nalgene, Thermo Scientific) where the particles were sampled onto the open-faced filters. A rain head protected the filter unit from precipitation. Ambient air was sampled with $14.91\,\mathrm{min}^{-1}$ for about 4 h during day and in some cases also during night time.

3.1.3. Heat Treatment

To investigate the contribution of heat-sensitive and organic-rich INPs to the ice nucleation activity of the soil samples, different heat treatment methods were used.

368 K Suspension Heat Treatment

Heat-sensitive substances of potentially biological origin are considered to largely contribute to the INP abundance at higher temperatures (Hill et al., 2016). A moderate heat treatment of 368 K has been chosen in order to denature proteinaceous INPs and thereby to investigate their contribution to the INP concentration in the sampled air masses. In this work, this treatment has only been conducted with aerosol samples analyzed with the CSU-IS. Here, 3 ml of the aerosol suspension is pipetted into a sterile 50 ml centrifugal tube. The screw-cap is closed and the tube is placed together with a precisely fitting styrofoam ring in a water-filled glass beaker. The styrofoam ring ensures that the tube is floating and that all of the aerosol suspension is below the water surface for best heat transfer. The beaker is covered with aluminum foil and is placed on a stirring hot plate to boil the water (similar to Fig. 3.8, but without UV lights). The sample tube remains in the boiling water for 20 min. Due to the low ambient pressure at CSU (Fort Collins, 1525 m a.s.l.), this corresponds to a temperature of 368 K. To obtain information on the contribution of heat-sensitive INPs on the ice nucleation activity, the INP concentration after heat treatment was measured with the CSU-IS and compared to the result form the untreated sample portion.

673 K Bulk Heat Treatment

To investigate the contribution of organic matter on the ice nucleation activity, organic substances present in the samples are oxidized due to a stronger heat treatment at 673 K. Tobo et al. (2014) showed that the 673 K heat treatment has a comparable effect on the freezing behavior of the treated INPs than a hydrogen peroxide treatment. For organic matter pyrolysis, 10 g of the soil dust bulk material is exposed to 673 K dry heat for 2 h. The heat exposure causes a visible dark coloring of the soil samples (Fig. 3.7). Then, the soil dust is aerosolized and is again investigated by the different INP measurement methods in order to detect the influence of the heat treatment on the ice nucleation behavior.

(a) Untreated soil dust.

(b) Heat-treated soil dust.

Fig. 3.7.: German soil dust from Gottesgabe (SDGe01) before (a) and after (b) 673 K bulk heat treatment.

Aerosol Heating Tube

An aerosol heating tube was constructed for the laboratory experiments in the AIDA and APC chambers. This heating device actually consists of four parallel tubes with a length of 150 cm and an inner diameter of about 8 mm each. On their way from the aerosol generator to the chambers, the aerosol was passed through the tube bundle and thereby heated to a temperature of up to 673 K for selected experiments. The effect of heating on the ice nucleation activity of the aerosol was then quantified by comparison with the results from experiments with the non-heated aerosol.

3.1.4. Hydrogen Peroxide Treatment

As an alternative method to the 673 K heating, the organics in the aerosol suspensions can also be digested with hydrogen peroxide (Tobo et al., 2014). In this work, this treatment has only been conducted with atmospheric aerosol samples analyzed with the CSU-IS. The method is described in McCluskey et al. (2017) and will only briefly be summarized here. For the treatment, 2 ml aerosol suspension together with 1 ml 30 % H_2O_2 (Sigma Aldrich) is pipetted into a sterile 50 ml centrifugal tube to obtain a 10 % H_2O_2 concentration. To generate hydroxyl radicals (Mikutta et al., 2005), the sample tube is immersed in boiling water (similar to the 368 K aerosol suspension heating) and exposed to UV light for 20 min (Fig. 3.8). The remaining H_2O_2 needs to be transformed into water and oxygen to suppress its

Fig. 3.8.: Hydrogen peroxide treatment. Picture courtesy of Thomas C. J. Hill.

potential influence on the freezing behavior of the suspensions. This is achieved by adding a catalase enzyme (Cat. number 100429, MP Biomedicals) (Mikutta et al., 2005) in 20 µl steps to the cooled aerosol suspension until no further effervescence is visible upon its adding. The INP concentration in the so

treated suspension is then also measured with the CSU-IS and again compared with the result from the untreated suspension portion in order to quantify the contribution of organics to the INP abundance.

3.2. The Cloud Simulation Chamber AIDA[2]

The cloud chamber facility AIDA enables to simulate the formation of clouds and to further investigate the involved microphysical processes under atmospherically relevant conditions.

3.2.1. Working Principle

The setup of the AIDA cloud chamber facility is described in several publications (Möhler et al., 2003, 2005; Benz et al., 2005; Wagner et al., 2009). This section will focus on a brief description of the setup for heterogeneous ice nucleation experiments with soil dust samples.

The main element of the facility is a cylindrical aluminum vessel, the actual cloud chamber, which is located inside a large thermostatic housing. This chamber has a height of about 7 m, a diameter of 4 m and a wall thickness of 20 mm, which result in a relatively large chamber volume of 84 m^3. The chamber is equipped with several instruments which monitor the thermophysical chamber conditions during the experiments and the formation of the simulated cloud (Tab. 3.1).

Tab. 3.1.: Instruments and their measured variables which are used for the investigation of heterogeneous ice nucleation at the AIDA cloud expansion chamber.

Instrument	Measured Variables
APeT	total water concentration
(SP-)APicT	water vapor concentration
APS	aerosol particle size distribution
CPC	aerosol particle number concentration
MBW	total water concentration
welas	droplet and ice particle size distribution
pressure sensor	pressure
SMPS	aerosol particle size distribution
vertical thermocouple string	gas temperature

The air inside the thermostatic housing is circulated through heat exchangers which can be cooled either with large refrigeration systems to about 243 K or by liquid nitrogen evaporation to 183 K. To ensure homogeneity of the temperature inside the chamber, a mixing fan is used, which is located around 1 m above the bottom of the chamber.

[2] Some elements of this section are adapted with changes from the author's diploma thesis (Schiebel, 2014).

Two strong mechanical pumps can be operated at different pump speeds and allow for adiabatic expansion cooling experiments. Starting at ambient pressure such so-called expansion experiments simulate the thermodynamical and cloud formation processes occurring in air parcels ascending in the atmosphere. For an additional very fast expansion, and thereby a strong additional cooling by 2 K to 3 K, the AIDA chamber volume can be expanded into the previously evacuated APC chamber by opening a valve in a connection tube with a diameter of 10 cm (Fig. 3.9) (Wagner et al., 2017). During an expansion experiment, all sensor data is recorded with a frequency of 1 Hz.

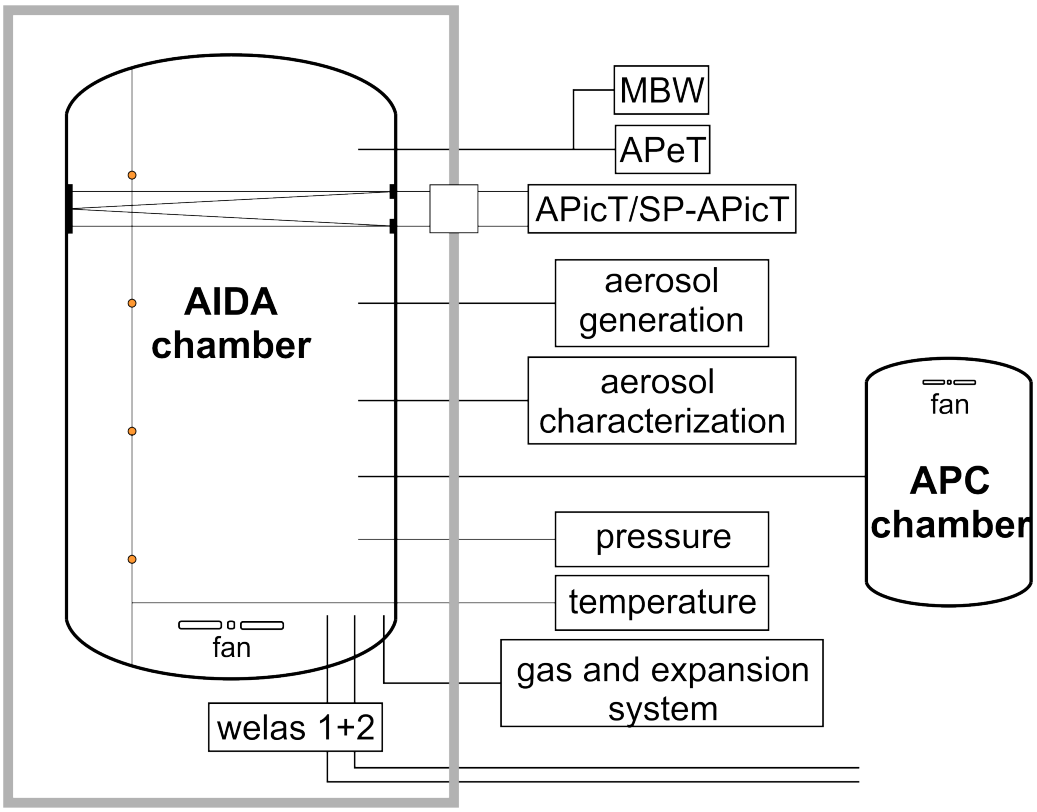

Fig. 3.9.: Schematic of the AIDA chamber with the instrumentation used for heterogenous ice nucleation experiments, adapted with changes from Möhler et al. (2003) and Benz et al. (2005).

Before the expansion, the soil dust aerosol particles are injected into the chamber (Sec. 3.1.1). The resulting aerosol number concentration, size distribution and surface area concentration of the dust aerosol are measured as described in Section 3.1.1. Thereby, the CPC (CPC3010, TSI) measures prior to the expansion and also during the measurement, whereas the SMPS (combination of DMA3081 and CPC3010) and the APS (APS3321) only measure prior to the cloud expansion experiment, because they need to be disconnected during the pressure drop of the expansion.

The size and number concentration of the droplets and ice particles are measured during the cloud simulation experiments with the optical particle counter welas, which will be described in more detail below.

Temperature Measurement

The gas temperature inside the chamber, T_g, is measured with a vertical string of four thermocouples which are fixed at different levels inside the chamber (Fig. 3.9), about 1 m off the vertical axis. The wall temperature of the chamber, T_w, is measured with another set of thermocouples, which are directly connected to the chamber wall. Both, T_g and T_w are measured with a frequency of 1 Hz and with an accuracy of ± 0.3 K (Möhler et al., 2006).

Humidity Measurement

Both the gas-phase and the total (gas- and condensed-phase) water concentration inside the chamber is measured with several different instruments. The water vapor concentration and therefore the partial pressure is measured in situ with the multipath tunable diode laser hygrometer APicT (AIDA PCI in cloud TDL) or by its single-path version SP-APicT. Additionally, a third tunable diode laser (TDL) hygrometer, the APeT (AIDA PCI extractive TDL), determines the total water content. It continuously samples gas from the chamber through a heated stainless steel line, where the condensed water content, either droplets or ice, completely evaporates. A fourth instrument, the chilled-mirror frost point hygrometer MBW (373LX from the company MBW), is attached to the same heated sampling line.

The liquid water saturation ratio S_{liq} and the relative humidity RH_{liq} can be derived from the ratio of the water vapor partial pressure p_w and the saturation pressure $p_{s,liq}(T_g)$:

$$S_{liq} = \frac{p_w}{p_{s,liq}(T_g)} \qquad [3.5]$$

The water vapor partial pressure p_w (in Pa) is obtained from the measured water concentration and the water vapor saturation pressure with respect to liquid water $p_{s,liq}$ (in Pa) is calculated from the gas temperature inside the chamber T_g given in K by using a parametrization by Murphy and Koop (2005) ($123 < T_g < 332$ K):

$$\begin{aligned} p_{s,liq}(T_g) \quad = \quad & exp(54.842763 - 6763.22/T_g - 4.210\,ln(T_g) \\ & + 0.000367\,T_g + tanh[0.0415\,(T_g - 218.8)]\,(53.878 \\ & - 1331.22/T_g - 9.44523\,ln(T_g) + 0.014025\,T_g) \end{aligned} \qquad [3.6]$$

This leads to the relative humidity with respect to liquid water RH_{liq}:

$$RH_{liq} = S_{liq} \times 100 \qquad [3.7]$$

The relative humidity with respect to ice is analogously calculated as the ratio of the water vapor partial pressure to the saturation vapor pressure with respect to ice $p_{s,ice}(T_g)$:

$$S_{ice} = \frac{p_w}{p_{s,ice}(T_g)} \qquad [3.8]$$

The saturation vapor pressure with respect to ice $p_{s,ice}$ (in Pa) can be calculated from the gas temperature T_g (in K) as follows (Murphy and Koop (2005), $T_g > 110\,\mathrm{K}$):

$$p_{s,ice}(T_g) = exp(9.550426 - \frac{5723.265}{T_g} + 3.53068\,ln(T_g) - 0.00728332\,T_g) \quad [3.9]$$

The relative humidity with respect to ice RH_{ice} is then determined by:

$$RH_{ice} = S_{ice} \times 100 \quad [3.10]$$

The relative humidity inside the AIDA chamber is determined with an accuracy of about $\pm 5\,\%$ (Fahey et al., 2014).

INP Measurement

The optical particle counter welas is used for measuring the size and number concentration of droplets and ice particles during the cloud expansion experiment. The instrument illuminates the single particles with a white light source. With the help of Mie calculations, the intensity of light scattered by single particles can be converted into the particle sizes (Mie, 1908). The particle number concentration is derived from the number of measured particles per time interval and from the volume flow rate through the optical detection volume of the sensor.

The AIDA facility is equipped with two welas systems with different measurement ranges to cover a wide range of particle sizes. welas 1 detects particles between 0.7 µm and 46 µm and welas 2 between 5.0 µm and 240 µm (Wagner and Möhler, 2013). Both sensors are located underneath the chamber and inside the thermal housing and are connected to it via vertical sampling lines (Fig. 3.9). Operating the sensor at chamber temperatures avoids evaporation of the sampled cloud droplets and ice particles. The welas system samples with a constant flow of $51\,\mathrm{min}^{-1}$ from the chamber. These sampled particles are transported through the optical detection volume of the welas sensor, which is located inside the sensor block and is illuminated by white light (Fig. 3.10).

Inside the sensor, the white light passes two lenses and an aperture before it illuminates the particles (Fig. 3.10a). The apertures and shapes of the lens systems define the detection volume. The light scattered at an angle of $90 \pm 12^\circ$ passes another aperture and two lenses before it is collected by the optical fiber and transported to the detector.

If a particle is not completely inside the detection volume, it will only be partially illuminated and hence its size would be underestimated. Therefore, the optical particle counter welas has a three-dimensional 'T'-shaped optical detection volume instead of a rectangular prism (Fig. 3.10b). This 'T'-shaped volume is defined by two 'T'-shaped apertures of the illumination and detection optics. This results in a complete edge zone correction, for which the recorded pulse shapes of the scattered light are used. Due to the small size of the detection volume (e.g., welas 2300: w x d x h = 144 µm x 227 µm x 227 µm) a homogeneous illumination is ensured.

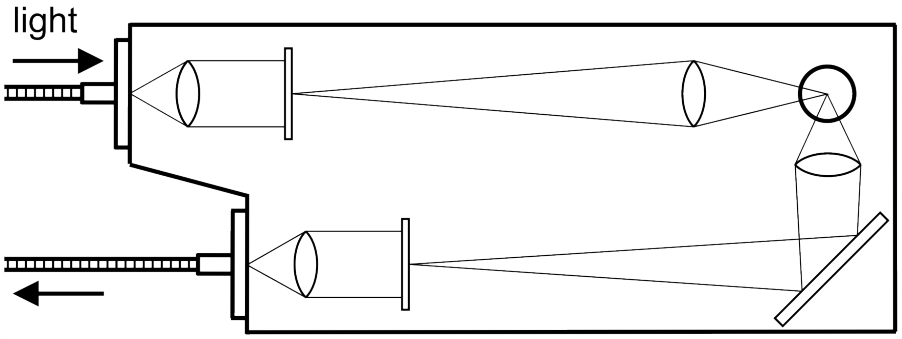

(a) Welas sensor.

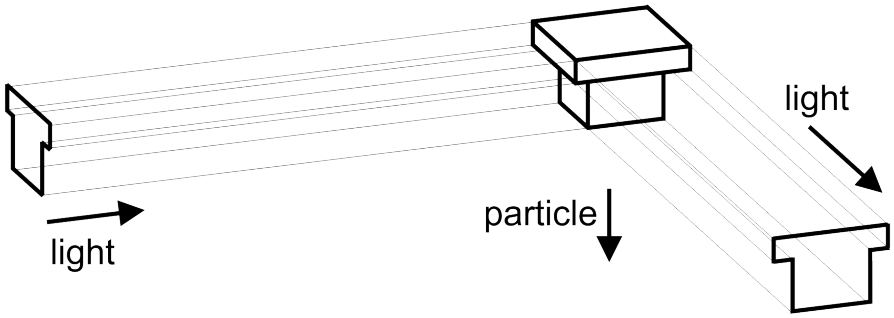

(b) Optical detection volume.

Fig. 3.10.: Schematic of the welas sensor. (a): Optics and optical path of white light inside the welas sensor (view from above). (b): Optical detection volume inside the circular cuvette of the welas sensor. From Schiebel (2014), adapted from PALAS (2010).

Welas is a single particle detector. If there is more than one particle simultaneously present inside the detection volume, they will be counted as one big particle instead of several small particles. This results in an error in both the size and the number concentration. Thus, a threshold for the measured pulse length is set in order to avoid measuring errors due to coincidence. By setting an additional lower pulse length threshold, measurement uncertainties due to for example electrical noise are minimized as well.

The scattered light intensity is related to particle size with the help of Mie calculations (Benz, 2006; Schiebel, 2014). In addition, monodisperse aerosol particles of known size are used to calibrate the instrument regularly to compensate the continuous decrease in the lamp intensity. Setting an individual size threshold for each experiment allows to distinguish between ice particles and other measured particles. The ice particle number concentration $c_{n,ice}$ of the detected particles is then calculated as follows (Benz, 2006):

$$c_{n,ice} = \frac{N_{ice}}{\Delta t \, \bar{v} \, a_{dv}} \qquad [3.11]$$

Here, N_{ice} is the number of measured particles above the ice threshold detected during the time interval Δt. The measured mean velocity of the particles through the detection volume $\bar{v} = l_{dv} \, \tau^{-1}$ is derived from

the length of the detection volume l_{dv} and the measured pulse length τ. a_{dv} is the cross-sectional area of the detection volume. The number concentration of all detected particles is derived analogously from the total particle number.

Since the activated aerosol particles inside the AIDA chamber are acting as condensation nuclei or ice nucleating particle, one can conclude that each formed ice particle contains exactly one aerosol particle. Therefore, the measured ice particle number concentration is interpreted as the INP number concentration. It is determined with an accuracy of $\pm 20\,\%$ (Wagner and Möhler, 2013).

INAS Density

The ice nucleation active surface site (INAS) density n_s (Hoose and Möhler, 2012) describes the temperature- and humidity-dependent ice nucleation particle number N_{ice} normalized by the available aerosol surface s_{aero} (Connolly et al., 2009; Niemand et al., 2012; Ullrich et al., 2017) (see Sec. 2.2.2). Alternatively, it can also be calculated from the INP number concentration $c_{n,ice}$ and the aerosol surface concentration $c_{s,aero}$ (Eq. 2.7):

$$n_s(S,T) \approx \frac{N_{ice}}{s_{aero}} = \frac{c_{n,ice}}{c_{s,aero}} \qquad [3.12]$$

The measurement uncertainty of the AIDA aerosol characterization instrumentation (Sec. 3.1.1) in determining the aerosol surface concentration is $\pm 34\,\%$ (Ullrich et al., 2017). The error propagation of this uncertainty and the uncertainty in the INP measurement of $\pm 20\,\%$ (Wagner and Möhler, 2013) yields then to the uncertainty in the INAS density of about $\pm 40\,\%$ (Ullrich et al., 2017).

3.2.2. Typical Experiment

Prior to an expansion experiment, the AIDA chamber is cleaned. During this 4 h cleaning cycle, the chamber is evacuated to a pressure below about 2 hPa, and then ten times refilled with clean dry air to a pressure of 10 hPa and evacuated again to below 2 hPa. After these flushing cycles between 2 hPa and 10 hPa, the chamber is further evacuated for 1 h to the minimum pressure below about 0.1 hPa. At the same time, the chamber is cooled or warmed to the required starting temperature. After completing the cleaning cycle, pure water vapor is evaporated from a heated reservoir of ultrapure water and added to the evacuated chamber in order to form a thin ice layer on the cold chamber wall, which acts as humidity reservoir during the experiment. Then the chamber is refilled with dry and particle free synthetic air to atmospheric pressure.

When the required conditions are reached and the pressure is at ambient pressure, the aerosol particles are injected into the AIDA chamber (see Sec. 3.1.1 for details). The aerosol particle number concentrations are usually between $100\,\mathrm{cm}^{-3}$ and $350\,\mathrm{cm}^{-3}$ for the experiments of this thesis. The chosen concentration depends on the soil dust sample and on the temperature conditions of the experiment. For experiments at higher temperatures, where the ice nucleation activity is rather low, larger total aerosol surface areas, and as a consequence of this larger number concentrations, are required in order to measure

significant ice number concentrations. As described in Section 3.1.1, aerosol particles are characterized by various instruments or are collected on filters or other substrates for offline analysis.

After completing the aerosol characterization and collection, the actual AIDA expansion experiment is started by connection to the pump system (Fig. 3.11, t = 0 s). With this, the chamber pressure decreases nearly adiabatically and as a result, the gas temperature decreases as well due to expansion cooling (Fig. 3.11, panel 1). This then results in an increasing relative humidity (Fig. 3.11, panel 2).

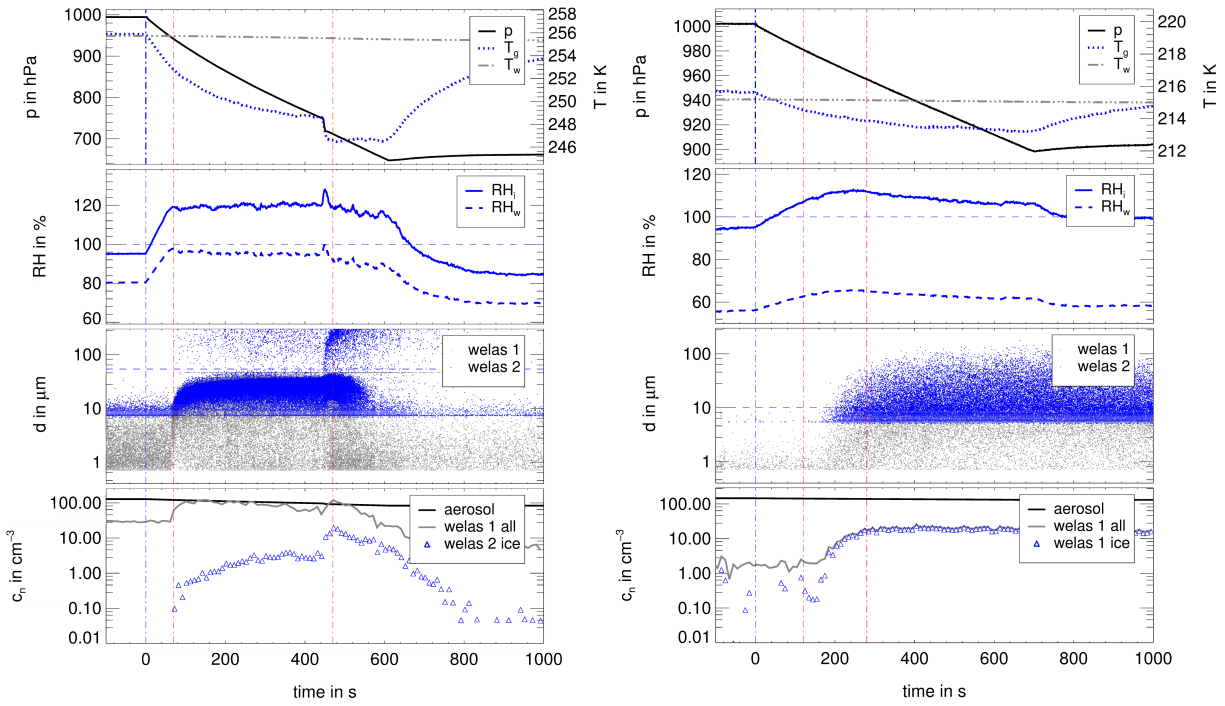

(a) Immersion freezing experiment.

(b) Deposition nucleation experiment.

Fig. 3.11.: Data time series of typical AIDA heterogeneous freezing experiments. Panel 1 shows the chamber pressure (left vertical axis) as well as the gas and the wall temperature (right vertical axis). Panel 2 shows the relative humidity with respect to liquid water and ice, respectively. Panel 3 shows the optical size of the single particles. The horizontal, blue line indicates the ice threshold. Panel 4 shows the aerosol number concentration measured with the CPC as well as the total and ice number concentration calculated from the measured single particle data of the OPC. The vertical blue line indicates the start of the expansion experiment, whereas the two vertical red lines indicate the time interval of the data analysis.

In case of an immersion freezing experiment (Fig. 3.11a), the relative humidity increases until water saturation is reached. At this point, the aerosol particles act as cloud condensation nuclei and start to form a supercooled liquid cloud in the chamber. Due to continued expansion cooling, the droplets grow further by condensing water vapor on their surfaces. With decreasing temperatures, some droplets start to freeze and the first ice particles are detected. The relatively large ice particles are distinguished from the relatively small aerosol particles and droplets by setting a size threshold in the measured OPC signal,

i.e. all particles above a set ice threshold are counted as ice particles (Fig. 3.11, horizontal, blue line in panel 3). As ice particles are of non-spherical shape, they are overestimated in size, which simplifies their identification. In the welas 1 signal, almost all of the forming ice particles are out of the measurement range. Nevertheless, the welas systems counts exceeding particles in the largest channel. This justifies to use the welas 1 sensor for detection of all particles. However, for the detection of the ice particle number, the welas 2 sensor is used. Since it is optimized for larger sizes, it is more precise and more sensitive for this purpose. The number of ice particles increases in the course of the experiment (Fig. 3.11a, panel 4) due to the decreasing gas temperature (Fig. 3.11a, about 7 K decrease). When the temperature is leveling off and the humidity conditions are still constant, AIDA might be connected to the previously evacuated APC chamber (Sec. 3.2.1). This so-called *APC chamber jump* causes a fast pressure and temperature drop and a resulting peak humidity (Fig. 3.11, t = 440 s). In this process, a second ice mode is formed, which is soon followed by the disconnection of the pump system and the thus defined experiment end time.

The data analysis starts as soon as the ice particle number concentration exceeds the ice background value of $0.1\,\mathrm{cm}^{-3}$ (Ullrich et al., 2017) (Fig. 3.11a, first vertical, red line at t = 70 s). As long as this value is increasing and the temperature is decreasing, the experiment can be analyzed for temperature dependent immersion freezing data. Also, in case of an APC chamber jump, this data is analyzed as well and gives additional information for lower freezing temperatures. After the induced strong pressure drop, the data analysis is stopped (Fig. 3.11a, second vertical, red line at t = 470 s). The temperature- and humidity-dependent ice particle number concentration interpreted as immersion freezing is derived from the measured data as described in Ullrich et al. (2017). The defined analysis interval is divided into Δt bins of at least 10 s. With this, data fluctuations are smoothed. For counting statistics reasons, the analyzed time intervals have to include at least five ice particle counts. The differential ice particle number concentration as well as the correlated mean temperature and humidity are then calculated time-bin wise.

In case of a deposition nucleation experiment (Fig. 3.11b), ice particles nucleate already at a relative humidity of a few percent above ice saturation with no observable formation of an intermediate liquid phase (Fig. 3.11b, first vertical, red line at t = 10 s). At the comparable low temperatures of the deposition nucleation regime, the ice crystal growth is relatively slow which results in rather small ice particles. As a consequence, in this type of experiment the welas 1 sensor is used to determine the ice particle number concentration, because its measurement range is more precise for smaller particles.

Similar to the immersion freezing experiments, the data analysis starts when the ice number concentration exceeds the background threshold of $0.1\,\mathrm{cm}^{-3}$. The measured data can then be analyzed as deposition nucleation results as long as the ice particle number concentration is increasing. At a certain point, the humidity reaches a maximum, where the formation rate of new ice crystals levels off and the the data analysis is therefore stopped (Fig. 3.11b, second vertical, red line at t = 140 s). The ice particle number concentration at the peak humidity is interpreted as the deposition nucleation data point for this

particular experiment. The corresponding temperature is a mean temperature calculated between the start of the data analysis and the time of the peak humidity.

With the stop of the expansion, the gas temperature T_g starts to increase and slowly approaches the wall temperature T_w, which remained almost constant during the experiment. This increase in temperature causes a decrease of the relative humidity. During this warming period, some larger ice crystals, formed especially during the immersion freezing experiments at the higher temperatures, are lost by sedimentation to the chamber floor. All crystals shrink in size and later also disappear by evaporation. At this point, the experiment is finished and the chamber needs to be cleaned before the next experiment can be conducted.

3.3. The Continuous Flow Diffusion Chamber INKA

INKA measures the ice nucleation activity of sampled aerosol under well-defined temperature and saturation ratio conditions. Section 3.3.1 will describe the working principle. This includes the INKA flow system, the cooling system, the optical particle counter (OPC) and the data acquisition system. Section 3.3.2 will show a typical INKA experiment and will discuss measurement uncertainties. The validation of the instrument performance is part of Section 3.3.3.

3.3.1. Working Principle

Diffusion tube

Different CFDC designs have been developed using concentric cylinder geometry (Rogers, 1988; Rogers et al., 2001; Glen and Brooks, 2014) or vertically or horizontally orientated parallel chamber walls (Stetzer et al., 2008; Kanji and Abbatt, 2009; Garimella et al., 2016). INKA is based on the cylindrical CFDC design (Archuleta et al., 2005), which will be described in this section. Its main part consists of two vertically-oriented, concentric copper tubes with diameters of 7.91 cm and 10.18 cm and a length of 150 cm. The two cylinders of different diameter form an annular gap with a width of 1.14 cm. The inner walls of this gap are temperature controlled and, during measurements, coated with a thin layer of ice. The sampled aerosol flow enters the annular gap from the top through a thin circular nozzle (Fig. 3.12). There, it is encased by a particle-free, dry sheath air flow to keep it away from the two iced walls and to focus the aerosol near the center of the gap. When entering the diffusion tube (DT), the total flow first passes the activation section (AS). Here, the inner and outer wall have different but constant temperatures below the melting point of water. The temperature difference controls the profiles of temperature and water vapor pressures between the iced walls, and by that also the temperature and relative humidity in the aerosol flow region (AFR). After passing the nucleation and growth section, the here formed ice particles as well as any remaining aerosol particles or droplets enter an evaporation section (ES). Since both walls of this section have the same temperature, the water vapor pressure drops below liquid water

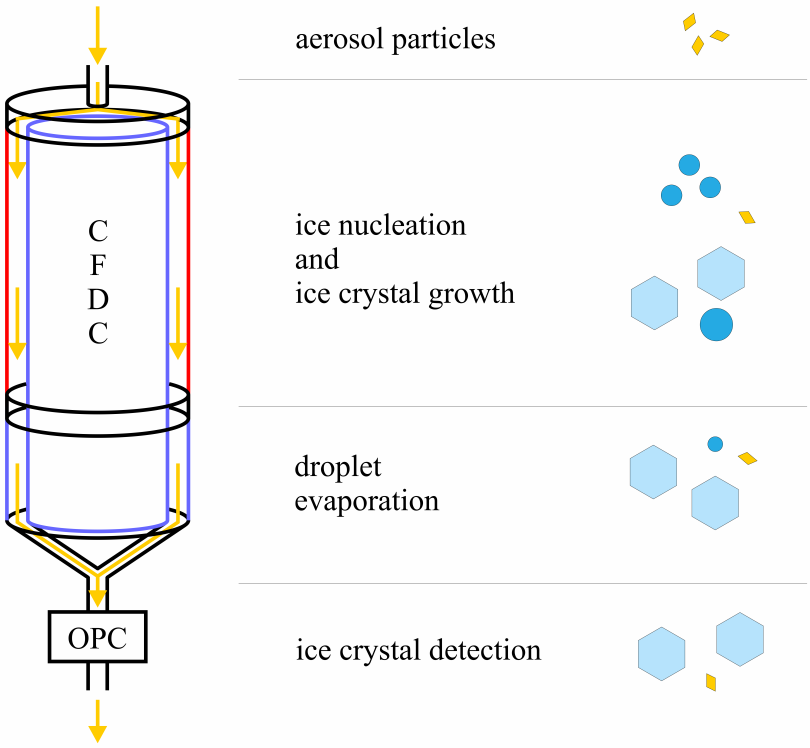

Fig. 3.12.: Schematic of the different cylindrical CFDC sections, which are passed by sampled aerosol (orange arrows): Ice nucleation and ice crystal growth section, droplet evaporation section, and particle detection.

saturation pressure. As a result, the droplets evaporate and the ice crystals continue to grow. Thus, the possible mixture of remaining aerosol particles, droplets and ice crystals is reduced to (small) aerosol and (large) ice particles and can be distinguished by setting a size threshold.

The surfaces of the chamber walls have been chemically treated to carry a thin layer of black copper sulfide. This enables a uniform wetting during the icing procedure and therefore a smooth and homogeneous ice layer. Any inhomogeneity is a preferred starting point for forming frost, especially during measurements, where the temperature difference results in diffusion of water vapor between the two ice-coated walls. The residence time of the particles inside the activation section depends on the flow and temperature settings as well as on the operation mode (with or without ES). Due to its relatively large DT length, INKA has an increased residence time (e.g. $t = 7.34\,\mathrm{s}$ for $\delta T = 18.12\,\mathrm{K}$, $\mathrm{p} = 995.26\,\mathrm{hPa}$ and Q = 12.48 $1\mathrm{min}^{-1}$, with ES), which thereby enhances the possibility of complete activation and sufficient growth of the ice particles.

The wall temperatures, the total flow and the dimensions of the DT determine the velocity profile inside the annular gap and therefore the temperature and humidity conditions the investigated aerosol is

exposed to. Due to the temperature difference between the two walls in the AS, the contribution of free convection is considered for the calculation of the velocity profile (Rogers (1988), Eq. 13):

$$v(z,\delta T) = \frac{3}{2}\bar{v}\left(1-\left(\frac{z}{d}\right)^2\right)+\delta T\,\gamma\left(\left(\frac{z}{d}\right)^3-\frac{z}{d}\right), \qquad [3.13]$$

where v is the velocity as a function of the distance z from the center line of the flow and the temperature difference δT between the two walls. $\bar{v}$ is the mean velocity and d is the half width of the annular gap.

$$\gamma = \frac{\rho_{air}\,g\,d^2}{12\mu\,\overline{T}} \qquad [3.14]$$

is a coefficient, where ρ_{air} is the air density, g is the gravity, μ is the dynamic (shear) viscosity of air and $\overline{T}$ is the mean temperature. When both walls are set to the same temperature ($\delta T = 0$), the velocity shows the typical parabolic profile for a laminar flow described by Hagen-Poiseuille's law (Fig. 3.13, orange dashed line). In the AS, the two walls are held at different temperatures. This temperature difference

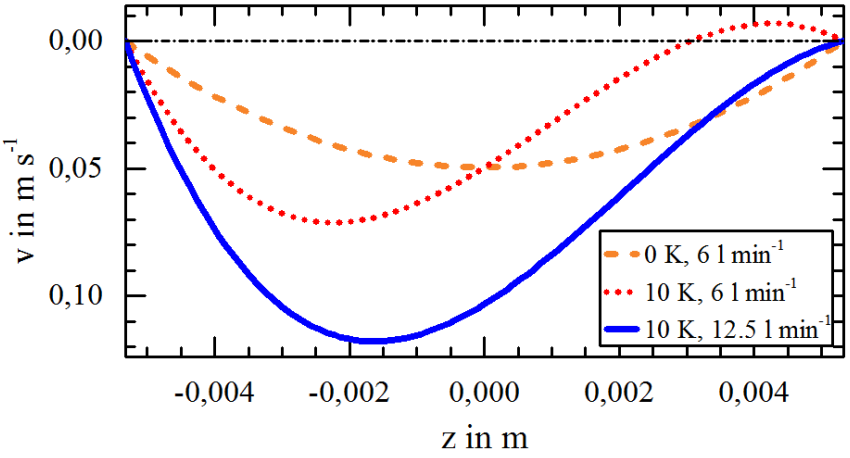

Fig. 3.13.: Velocity profiles for different temperature and flow settings inside the annular gap of the CFDC: Laminar flow (δT = 0 K, Q = 6 l min^{-1}, orange dashed line), reverse flow due to buoyant effect (δT = 10 K, Q = 6 l min^{-1}, red dotted line) and typical flow profile (δT = 10 K, Q = 12.5 l min^{-1}, blue solid line) as a function of the distance z from the center of the gap. Adapted from Rogers (1988).

causes buoyancy so that the laminar flow is superimposed by a buoyant circulation (Fig. 3.13, red dotted line). To avoid a reverse flow close to the warm wall, Equation 3.13 requires:

$$\delta T < \frac{3}{2}\frac{\bar{v}}{\gamma} \qquad [3.15]$$

Thereby, relatively small temperature differences or relatively high flow rates avoid a non-ideal flow behavior inside the annular gap (Fig. 3.13, blue solid line). The calculated velocity profile allows to determine the position of the aerosol flow (typically 10 % of the total flow) ranging from edge a to edge b (Fig. 3.14, *a* and *b*). It is surrounded by dry, synthetic sheath air (typically 45 % of the total flow on both sides). The buoyant effect due to the temperature difference between the two walls slightly shifts

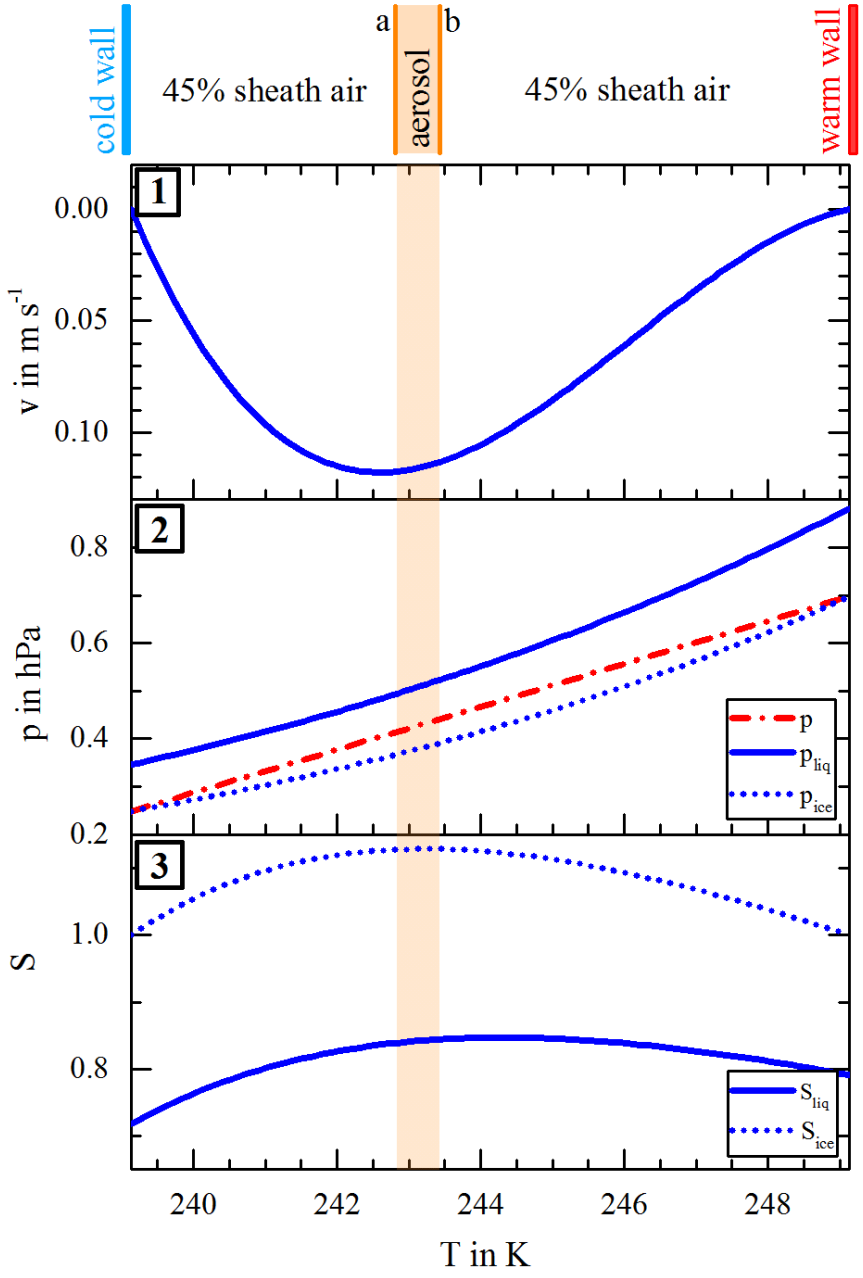

Fig. 3.14.: This figure shows the velocity profile (panel 1), the steady state water vapor pressure, the temperature-dependent saturation vapor pressure with respect to water and with respect to ice (panel 2, calculated with the parametrization by Murphy and Koop (2005)), and the saturation ratios with respect to liquid water and ice (panel 3) inside the annular gap of the CFDC. The orange area indicates the position of the sampled aerosol ranging from edge a to edge b. In this example, the cold wall is set to 239.15 K, the warm wall to 249.15 K and the total flow to 12.51 min^{-1} (90 % sheath air). Since the steady state temperature profile shows a linear gradient, the x-axis is linear to the distance from the cold wall. Adapted from Rogers (1988).

the aerosol flow towards the cold wall (Fig. 3.14, panel 1). In steady state, due to diffusion of heat, the temperature gradient between the two walls of the activation section is linear. Diffusion of water vapor between the two ice-coated walls also results in a linear gradient of the steady state water vapor partial pressure (Fig. 3.14, panel 2). The exponential relationship between the temperature and the saturation vapor pressure (Clausius Clapeyron law) leads to a maximal supersaturation close to the center of the annular gap and near the position where the aerosol passes (Fig. 3.14, panel 3).

Flow System and Operation Modes

Many electronic devices surround the DT in order to control the air and water flows which are required for the different operation procedures of INKA (Fig. 3.15). Besides the DT itself and the OPC, the flow system consists of three pumps: an air pump, a vacuum pump and a water pump. Further, there are two mass flow controllers (MFCs). One to control the sheath air flow and the second for the total flow. Thereby, they indirectly control the sampled air flow. In addition, the flow system is equipped with eight valves. One of these valves is a safety valve to protect the instrument from accidentally occurring over pressure (Fig. 3.15, valve 8). Three pressure sensors allow to monitor the pressure at different sections of the flow system. For interpretation of the data, the CFDC pressure (Fig. 3.15, p_1, MKS e-Baratron, Type 627C) is thereby the most important one. A condensation particle counter (CPC) enables to measure the particle number concentration before and after the DT to determine losses in the sampling line and the DT, respectively (Fig. 3.15, *CPC* via valve 6 or 7, respectively). Moreover, the CFDC is equipped with a movable base plate to which among others the OPC is mounted. Thus, the system can be adjusted to the different operation procedures: *cleaning*, *icing*, and *sampling*.

The cleaning step prepares the instrument for the measurements by removing water vapor and particles from the DT in order to reduce the formation of frost layers which can cause background counts during the measurement. Therefore, the DT bottom is connected to the vacuum pump for about 1 hour, while all other valves to the chamber are closed (Fig. 3.15, valve 1, 2, 3, 6 closed; valve 4 open). When the pressure remains constant and below 1 mbar for at least 30 min, a leak test is conducted.

The icing step generates a thin layer of ice on the chamber walls. Therefore, the CFDC is first cooled to 245.7 K. This ensures that the whole DT remains clearly below the melting point of ice during the entire icing procedure. When the target temperature of 245.7 K is reached, the chamber is re-pressurized with a controlled particle-free, dry air flow of 5 slpm from the top of the DT (Fig. 3.15, *synthetic air* via MFC_{sheath} and valve 2; valve 1, 3, 4 and 6 closed). When the CFDC pressure exceeds the ambient pressure, a valve (Fig. 3.15, valve 3) is opened manually in order to generate a continuous synthetic air flow of 5 slpm out of the chamber. This allows to change the base plate position without contamination by ambient air entering the system. During icing, this flow is maintained while the pre-cooled chamber is flooded from the bottom by pumping 5 l highly purified water into the chamber (Fig. 3.15, via valve 5). In the future, the icing procedure will be extended by a second water pump, which immediately pumps out the water after flooding the chamber. In the current INKA version, water drains only by gravity. This

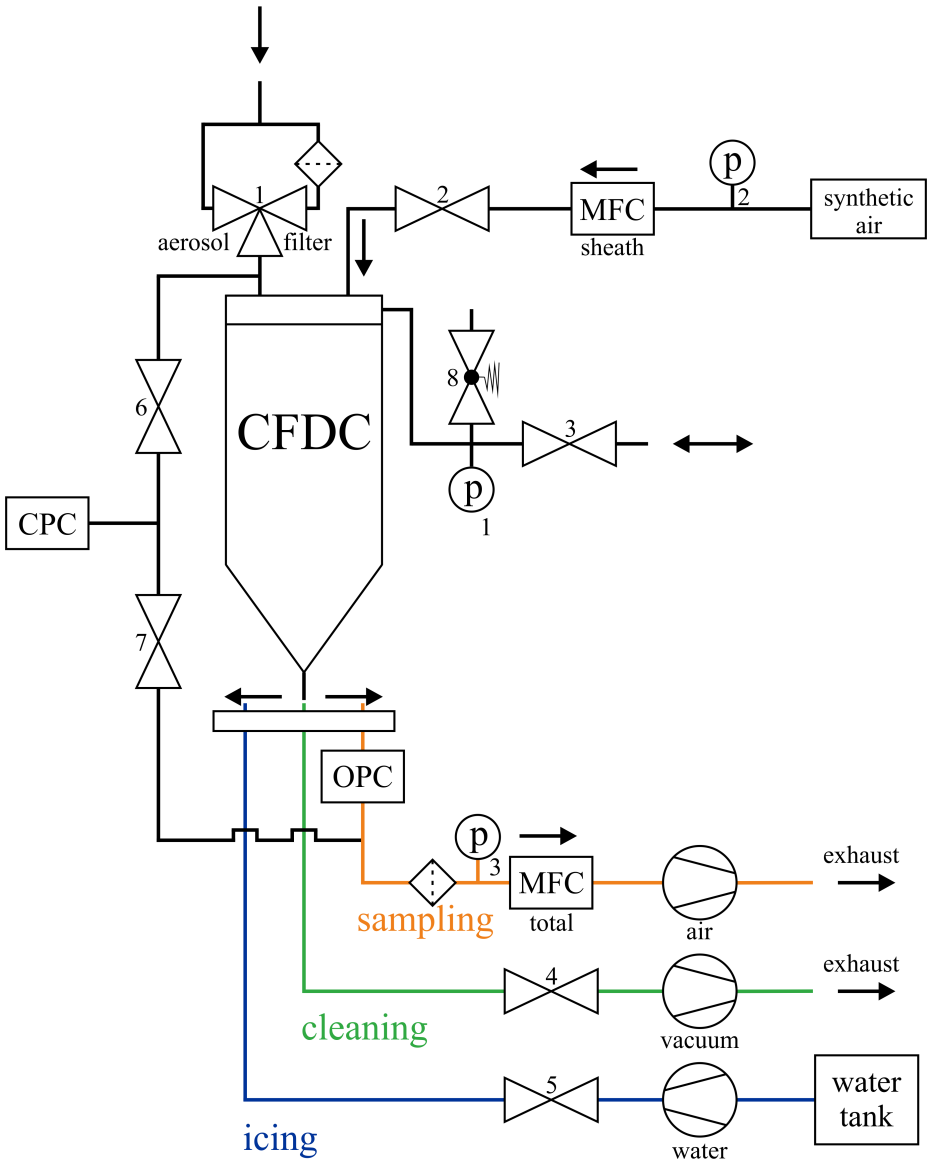

Fig. 3.15.: Schematic of the INKA instrument setup. The base plate of the diffusion tube is movable and thereby allows to adjust the air and water flow systems to the different operation procedures: sampling, cleaning and icing (see Sec. 3.3.1 for details).

might lead to a slightly thicker ice layer at the bottom of the chamber and therefore might result in a inhomogeneous gap width over the DT length. When the remaining liquid from the icing procedure is drained and the temperature of both walls is back to 245.7 K, the chamber is evacuated for another 5 min. This lowers the water vapor and helps to smooth the ice layer.

During the sampling and measurement cycles, the aerosol flow enters the top of the DT via an annular nozzle (Fig. 3.15, *aerosol* via valve 1). Inside the annular gap, it is surrounded on both sides by particle-free, dry sheath air (Fig. 3.15, *sheath air* via valve 2). INKA is usually operated with a total flow of 10-12.5 l min^{-1}. Thereby, the aerosol flow is confined to the central 10 % of the total flow (1-1.25 l min^{-1}). For dilution of high aerosol concentrations, INKA is sometimes operated with a reduced sample flow of 5 % of the total flow. In addition, as an alternative to using fresh synthetic air, INKA can be operated in a circulation mode where the total flow is recycled with dryers and filters and is re-used as sheath air. The aerosol sample flow can also be passed through a highly efficient aerosol filter. This allows to determine the background counts which are caused by frost break-up from the ice layer of the chamber walls. Such frost forms on the cold walls with an increasing amount during the course of the measurement. Downstream of the DT, ice particles, remaining droplets, and larger aerosol particles are detected by an optical particle counter (OPC, see Sec. 3.3.1 for details).

After about four hours measurement time, the ice layer of the DT is used up or the background from the frost artifacts are too high for continuing the measurements. Before sampling can be proceeded, the cleaning and icing procedure needs to be repeated.

Cooling System

The chamber walls of the DT are temperature controlled to set the temperature and humidity conditions for the aerosol activation. The inner cylinder, the upper two thirds of the outer cylinder and the lower third of the outer cylinder can independently be cooled. For thermal insulation, the two sections of the outer cylinder are separated by a Delrin ring. This setup allows to operate INKA in two different modes: In the ice nucleation mode, the CFDC is operated with the upper two thirds as the activation section and the lower third as the evaporation section. Thereby, the lower section enables the ice particles to grow on the expense of evaporating droplets. In the ice growth mode, the full length of the cylinders is operated as one long activation section. This might impede the identification of ice crystals by setting an ice threshold, but on the other hand the droplet information, and therefore the information on the frozen fraction, is maintained. For all measurements shown here, INKA is operated in the ice nucleation mode.

INKA's cooling system consists of two cryostats (LAUDA Proline RP 890). They transport the tempered cooling medium ethanol through cooling coils attached to the tubes. One of them cools the inner tube and then the lower part of the outer wall (Fig. 3.16, schematic on the right-hand side). The second cryostat cools the upper section of the outer tube to either the same temperature as the other walls in the preparation and icing periods, or to a somewhat higher temperature during the actual measurement

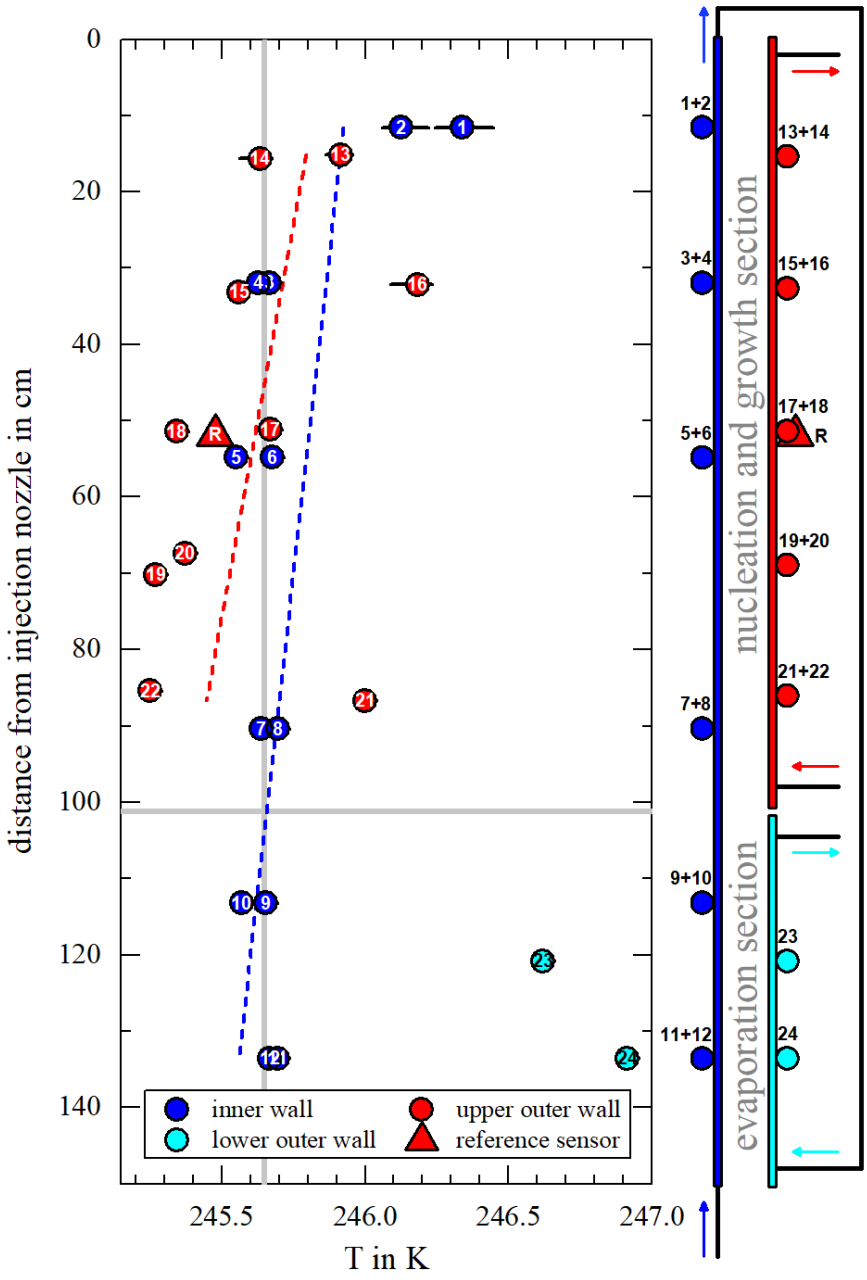

Fig. 3.16.: Height-dependent temperature distribution of INKA during static conditions at a set temperature of 245.65 K (vertical grey line) based on five different experiments. The circular data points show the mean values of the sensors whereas the horizontal black bars show the minimum and maximum values of the different experiments. The triangle indicates a Pt100 reference sensor. Fits to the height-dependent temperature of the inner wall (blue circles) and the upper outer wall (red circles) are given by dashed lines (colors accordingly). The horizontal grey line indicates the height where the nucleation and growth section ends and the evaporation section begins. The schematic on the right demonstrates the flow system of the two cryostats cooling the INKA columns.

periods, depending on the humidity settings. In all sections, the cooling liquid enters the coils from the bottom.

The wall temperatures are monitored with a 1 Hz time resolution by 24 temperature sensors (T-type thermocouples). The thermocouples are positioned at different heights inside the inner cylinder as well as outside the outer cylinders, whereby usually two sensors are located at the same height on opposite sides of the cylinder wall (Fig. 3.16). At half-height of the upper outer cylinder, additionally a Pt100 reference sensor is placed (Fig. 3.16, red triangle). Under static conditions at 245.65 K, the measured temperatures agree well to each other with a deviation to the set temperature of smaller than 0.5 K. The upper two sensors of the inner wall are thereby considerably warmer by about 0.6 K compared to the other sensors of the inner wall (Fig. 3.16, sensors 1 and 2). This might be caused due to poor thermal insulation. In addition, the two thermocouples of the lower outer wall have a deviation of more than 1.0 K (Fig. 3.16, sensors 23 and 24). This is caused by the fact that the lower outer tube is connected downstream of the inner tube (Fig. 3.16, schematic on the right-hand side). The agreement of the two thermocouples placed at the same height as the reference sensor is very good, with a deviation to the reference sensor of less than 0.2 K. The flow direction of the cooling liquid causes a height-dependent temperature trend with minimum temperatures at the bottom of the different sections and maximum temperatures at the top. The chillers of the INKA cooling system have operation temperatures as low as 183 K, this allows for ice nucleation studies with INKA to aerosol temperatures as low as about 213 K.

Depending on the aim of the experiment, the measurement conditions of INKA can be set and controlled in a wide range of temperatures (263 to 213 K) and relative humidities (e.g. RH_{ice} = 100 % to RH_{liq} = 114 % at 243 K). A typical operation procedure is a so-called RH scan, where the wall temperature difference is increased over time by keeping the aerosol temperature constant. The INKA cryostats are equipped with temperature control units for the purpose of an automated wall temperature change (see above for details). Measurements at steady temperature and humidity conditions are also possible if required, e.g. when sampling from the AIDA chamber during aerosol processing or for increasing the counting statistics at low INP concentrations.

OPC

An optical particle counter (OPC) is mounted to the movable plate below the chamber for measuring the size and number concentration of particles exiting the chamber. As in the evaporation section the formed droplets are evaporated for the benefit of the growing ice particles, particle size differences can be used to distinguish between (small) aerosol and (large) ice particles by setting a size threshold.

The INKA OPC system consists of a sensor (Climet CI-3100) and a multifunction data acquisition device (National Instruments X series). The sensor detects and amplifies the scattered light signal of the single particles, while the data acquisition device converts the analog signal of the sensor into a digital signal. A custom-made LabVIEW program processes, displays, and stores the digital data during the measurements. For every single particle, the time stamp, the pulse signal height, and the pulse signal

length are logged. The lower detection limit of the OPC is approximately 0.5 µm particle diameter. Particles exceeding the size range of the OPC are detected and counted in the largest size bin. The OPC covers the required size range for a size distinction between the aerosol and the forming ice particles.

Data Acquisition and Automation

A custom-made LabVIEW program controls the INKA instrument and processes, displays and logs all relevant data at a rate of 1 Hz during the various operating cycles. A cRIO micro-controller (National Instruments) provides the communication between the electronic devices and the LabVIEW software. The OPC data is transferred via an additional data acquisition interface (see above for details). A third interface (LAUDA command) enables the LabVIEW program to control the cooling system. With this control unit, the bath temperatures of the two cryostats can be read and changed according to a preset, linear slope. For this purpose, the LabVIEW software automatically computes the wall temperature changes required for a continuously increasing saturation ratio at a preset, constant aerosol temperature. The start and end points of the relative humidity ramp can also be chosen and preset, which defines the start and end point of the wall temperature ramps. A constant aerosol temperature in the diffusion tube requires slightly non-linear temperature ramps for the walls. Because the LAUDA command unit is limited to linear temperature changes, the calculated wall temperature changes are approximated by linear sections. Comprehensive test runs have shown that good results are achieved with just one linear ramp for the cold wall. The non-linear temperature increase of the warm wall temperature is approximated by either one or two linear fits depending on the desired saturation ratio range of the experimental run. Two linear fits to the warm wall temperature lead to an accurate sample temperature within a few tenths of a Kelvin.

3.3.2. Typical Experiment

A typical INKA experiment starts with a background measurement (Fig. 3.17, orange-shaded area before t = 0 s), where the incoming sample air is filtered (HEPA Capsule, PN 12144). This allows to determine the background counts the actual measurements have to be corrected for (Fig. 3.17, panel 2, blue-striped area). The background is additionally used for a significance check: Only ice number concentrations which are twice the background concentration are considered as significant values. For measurements of large aerosol particles, the background data can also be taken from the beginning of the RH scan, where the inlet is already switched from filter to aerosol and INKA is operated at low saturation ratios close to ice saturation. Thereby, not only the ice background, but also the aerosol background can be determined, which prevents their erroneous counting as ice particles.

Switching the INKA inlet from the filter to aerosol sampling starts the actual experiment (Fig. 3.17, t = 0 s). The INKA wall temperatures are changed during the course of a single experimental run. In order to keep the aerosol temperature constant, the warm wall temperature is increased faster than the cold wall

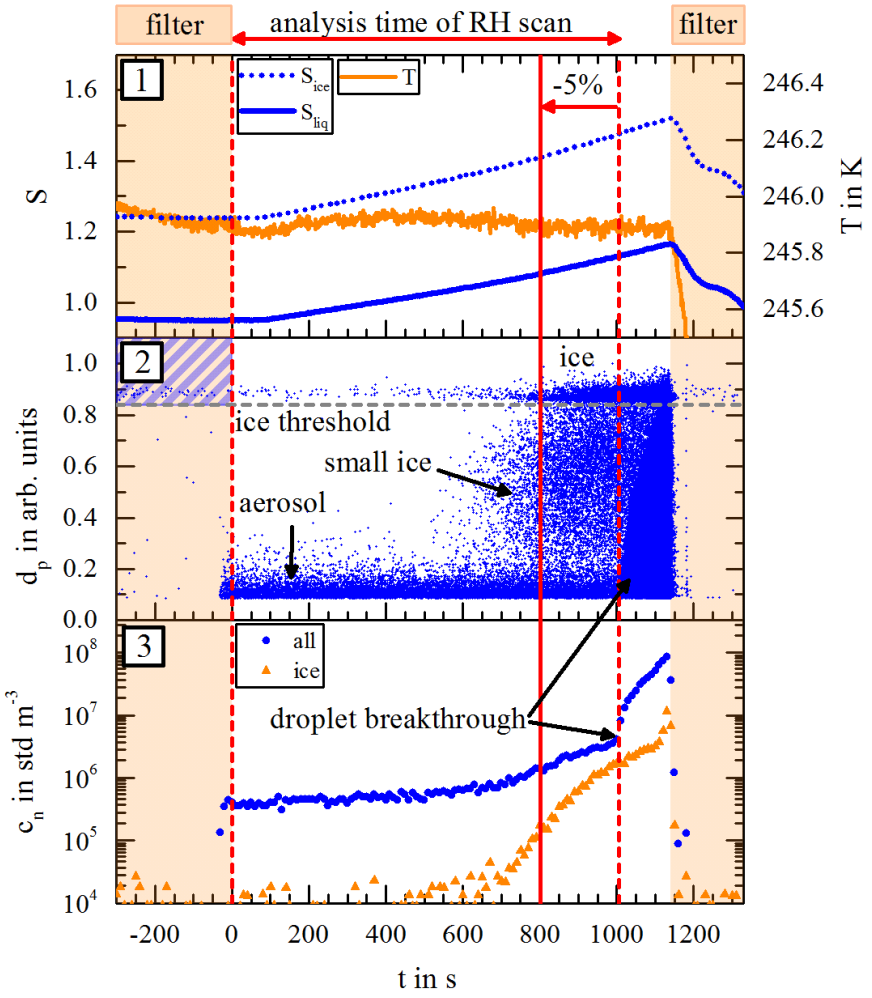

Fig. 3.17.: Time series of the INKA data for an automated relative humidity scan at 245.65 K aerosol temperature. Panel 1 shows the conditions the aerosol is exposed to: the saturation ratio with respect to liquid water and ice at the center of the aerosol flow (left axis) as well as the aerosol temperature (right axis). Panel 2 shows the single particle data of the OPC. The grey horizontal line indicates the set ice threshold and the blue-striped area shows the time and size interval for determining the measurement background. Panel 3 shows the calculated particle number concentration of all detected particles (blue circles) and of all ice particles (orange triangles). The orange-shaded bars indicate the time periods where the inlet of INKA is covered by a particle filter. The two vertical red dashed lines show the time period where the INKA RH scan is analyzed and the red solid line indicates the values which are interpreted as immersion freezing result.

temperature is decreased. This increasing temperature difference results in a continuously increasing saturation ratio at the center of the aerosol flow (Fig. 3.17, blue solid and dashed lines of panel 1).

At the beginning of the experiment, the OPC just detects the larger particles of the aerosol size distribution in the lower channels (Fig. 3.17, panel 2, *aerosol*). With increasing relative humidity, additionally, large ice particles are detected in the higher channels of the OPC (Fig. 3.17, panel 2, *ice*). The evaporation section evaporates droplets that could be misinterpreted as ice crystals of the same optical size and therefore allows for setting a size threshold to only distinguish between large ice crystals and small aerosol particles. Thereby, the ice particle number concentration can be determined. At a certain, temperature-dependent humidity, the water droplets are getting too large for complete evaporation in the evaporation section. With further increasing relative humidity, an increasing number of droplets are detected in the size range between aerosols and large ice crystals or, at some point, even at the same optical size as the ice crystals (Fig. 3.17, panel 2 and 3). This phenomenon is called *droplet breakthrough* (Stetzer et al., 2008). The droplet breakthrough onset depends on the instrument geometry, the flow rates (DeMott et al., 2015), and the temperature settings (Richardson, 2009). All OPC data shown in this thesis is normalized to the largest OPC size bin and is therefore in arbitrary units.

From the single particle data of the OPC, the ice particle number concentration $c_{n,ice}$ is calculated as follows:

$$c_{n,ice}(S,T) = \frac{N_{ice}}{Q_{aer}\,dt} \qquad [3.16]$$

where N_{ice} is the ice particle number, i.e. all particles above the set ice threshold counted in the time interval dt. Q_{aer} is the aerosol sample flow. The total particle number concentration $c_{n,all}$ can be determined analogously (Fig. 3.17, panel 3). With the assumption that the activated aerosol particles inside the CFDC are acting as condensation nuclei, one can conclude that each formed droplet contains exactly one aerosol particle. Therefore, the ice particle number concentration is interpreted as the INP number concentration.

When the breakthrough droplets reach the size range of the ice particles, the INKA experiment is finished. The inlet is then immediately switched back to filter and the wall temperatures are set to their starting temperatures in order to reduce the diffusional flux of water molecules from the warm to the cold wall (Fig. 3.17, orange-shaded area after t = 1140 s). This saves the ice layer on the warm wall for subsequent runs, and reduces frost formation and related background artifacts on the cold wall (see Sec. 3.3.1 for details about the INKA icing procedures).

The data is usually analyzed from the time where the INKA inlet is switched from filter to aerosol (Fig. 3.17, red dashed line at t = 0 s). Background corrected ice particle concentrations are calculated in preset time intervals as a function of the aerosol temperature and aerosol saturation ratio. With the onset of the droplet breakthrough, the data analysis of INKA is stopped (Fig. 3.17, red dashed line at t = 1005 s). Since the total particle concentration considers all particles detected by the OPC, it is an important parameter for determining the droplet breakthrough onset (Fig. 3.17, panel 3, sudden increase of the blue dots at t = 1005 s).

Beside setting the ice threshold, the most challenging part of the INKA data analysis is to select the relative humidity above water saturation where the INP concentration is interpreted as immersion freezing result. Further studies have already discussed this instrument specific issue (Petters et al., 2009; DeMott et al., 2015, 2017a) that the CFDC RH needs to be above the expected RH in clouds in order to measure immersion freezing. Also, continuously increasing ice number concentrations are usually observed for increasing relative humidities. Choosing an oversized relative humidity for the data analysis could result in erroneous counts of droplets as ice particles for CFDCs with a droplet evaporation section. On the other hand, the selection of an undersized relative humidity might result in an underestimation of counted ice particles. Most CFDCs, especially when operated in the field, are measuring at a constant RH of a few percentage above water saturation, usually 105 % (DeMott et al., 2015; Garimella et al., 2016). INKA on the other hand has the advantage of automated RH scans in combination with a continuous and stable aerosol source from the AIDA chamber. Thereby, the onset of droplet breakthrough can be determined for each individual measurement. This enables us to detect the maximum immersion freezing activity, while being in a range where the droplet breakthrough is very likely not going to influence the measurement. For the INKA analysis of immersion freezing experiments, the INP concentration and the temperature at the time where the relative humidity with respect to water is 5 % less than the relative humidity at droplet breakthrough onset is chosen. For a RH scan at 245.65 K, this would be at a liquid-water supersaturation of 8 % (Fig. 3.17, vertical red solid line).

Temperature Uncertainty

The ice nucleation process is strongly temperature-dependent (Riechers et al., 2013), in some regimes the relationship is even reported to be exponential (e.g., Ullrich et al. (2017)). Therefore, it is important to determine and consider the uncertainty of the temperature measurement.

For the calculation of the aerosol temperature, the cold and warm wall temperatures are required. Due to the cooling system of INKA, there is a temperature distribution along the chamber with slightly lower temperatures at the bottom. The nucleation process is expected to occur further downstream of the ice nucleation section and therefore only the lower positioned sensors are included in the mean value of the wall temperatures (51 cm to 90 cm from INKA chamber injection nozzle). Otherwise the upper sensors would falsely shift the nucleation event to a slightly higher temperature. The mean value of the lowest four sensors of the inner wall in the nucleation section is taken for the cold wall temperature (Fig. 3.16 and 3.18, sensor 5-8) and the mean of the lowest six sensors of the upper outer wall for the warm wall temperature (Fig. 3.16 and 3.18, sensor 17-22).

Comparison measurements with a Pt100 sensor have shown that the accuracy of the INKA temperature sensors is better than 0.2 K. To get information on the uncertainty in the wall temperature, it is important to determine the temperature deviation of the single INKA sensors to the mean wall temperatures. Under dynamic conditions, during a RH scan at 243.15 K, most of the sensors, which are used for calculation of the wall temperatures, have a deviation of less than 0.2 K (Fig. 3.18). However, one sensor deviates more

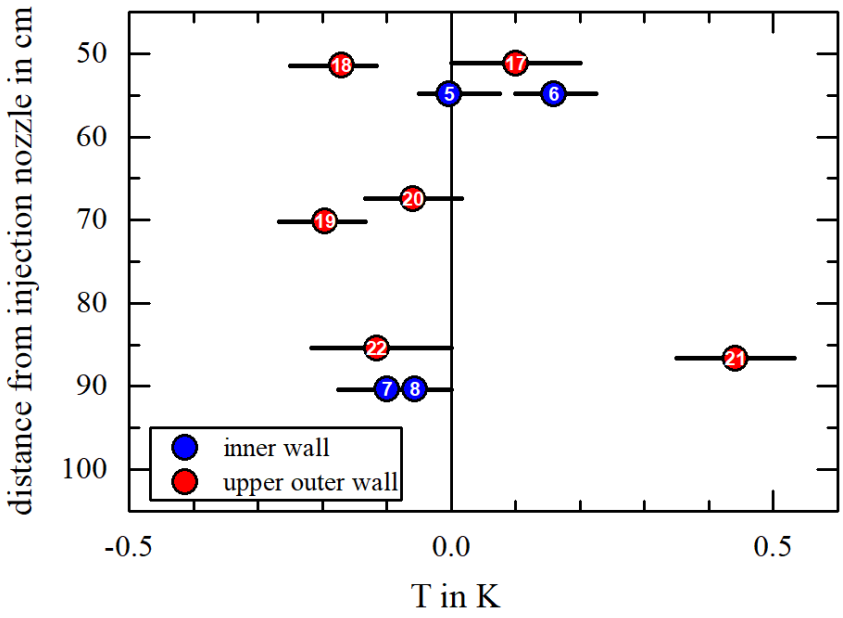

Fig. 3.18.: Height-dependent temperature deviation of the INKA sensors to the mean wall temperatures during a relative humidity scan at 243.15 K. The circular blue and red data points show the mean values of the inner and the upper outer wall sensors, respectively, whereas the horizontal black bars show the minimum and maximum values during the scan.

than 0.4 K from the mean value (Fig. 3.18, sensor 21). Another parameter influencing the temperature determination is the gap width ($2d$) of the CFDC. Depending on whether the cylinder dimensions of the technical drawing are used or the thickness of the ice layer is also considered, this value can vary between 0.99 and 1.14 cm (Fig. 3.19). This difference in d causes a relatively large difference in the temperature T_{aero} at the center of the aerosol lamina of 0.78 K (Fig. 3.19, orange triangles), in case of a cold wall temperature of 237.7 K, a warm wall temperature of 253.5 K, a total flow of 12.51 min^{-1} and a chamber pressure of 995.6 hPa. The thickness of the ice layer considered for the calculation is 700 µm, which is a mean value at the beginning of an experiment based on the assumption that the ice layer is homogeneously distributed. Nevertheless, due to the icing procedure, the ice layer at the bottom of the chamber is expected to be thicker than at the top. In addition, the thickness of the ice layer is decreasing in the course of the experiment. Therefore, there is a systematic increase of the gap width which causes a systematic shift of the temperature. For the INKA data analysis, the mean out of the minimum and maximum d values is used in order to consider its change over the course of an experiment. All these uncertainties in the gap width $2d$ of the CFDC chamber makes it difficult to determine the resulting measurement uncertainties. Therefore, in the following, an uncertainty ΔT of 0.5 K in determining the wall temperature is considered as a rather conservative estimate.

The influence of the wall temperature uncertainty on the aerosol lamina temperatures has been systematically evaluated (Fig. 3.14, a to b). The highest influence is given, when both wall temperatures

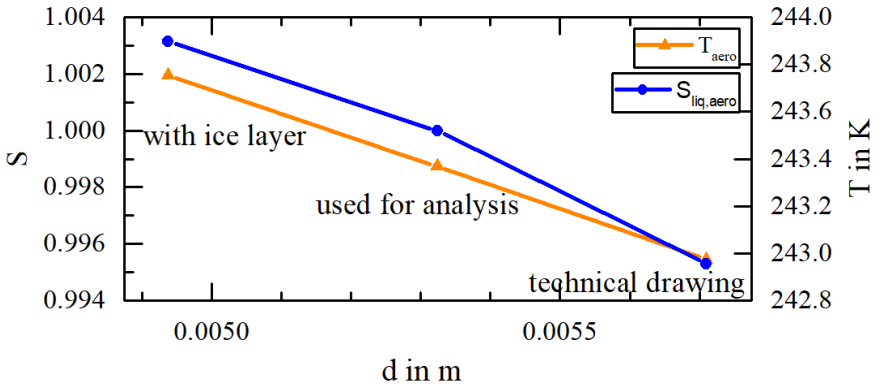

Fig. 3.19.: Dependence of the INKA temperature T_{aero} and saturation ratio $S_{liq,aero}$ with respect to liquid water at the center of the aerosol lamina on the half of the gap width d. The variation in T_{aero} (orange triangles) and $S_{liq,aero}$ (blue circles) is shown for the extreme cases where the dimensions of the technical drawing is used for the calculation or where the thickness of ice layer at the beginning of the experiment is considered. The d used for the data analysis is the mean out of the minimum and maximum values. The cold wall is 237.7 K and the warm wall is 253.5 K in this case, whereas the total flow is 12.51 min^{-1} and the pressure 995.6 hPa.

are increased or decreased by ΔT. The decrease of both wall temperatures by ΔT thereby results in a minimum temperature at the cold edge a of the aerosol lamina $T_{a,min}(T_{cold}-\Delta T, T_{warm}-\Delta T)$ (Fig. 3.20, lower blue line). Analogously, the increase of both wall temperatures results in a maximal increase of the temperature at the warm edge b of the lamina $T_{b,max}(T_{cold}+\Delta T, T_{warm}+\Delta T)$ (Fig. 3.20, upper blue line). The mean temperature difference between the center of the lamina T_{aero} and the edges T_a and T_b is ± 0.43 K for an INKA RH scan at 243.15 K (Fig. 3.20, orange lines enveloping the orange-shaded, striped area). The possible minimum and maximum lamina edge temperatures $T_{a,min}$ and $T_{b,max}$, resulting from the wall temperature uncertainty, differ on average by ± 0.51 K from T_a and T_b for the same example (Fig. 3.20, blue lines enveloping the blue-shaded area).

To reflect the fact that the aerosol lamina even for perfect flow behavior and without any wall temperature variances covers a range of thermodynamic conditions, the range from T_a to T_b is used as INKA's ice nucleation temperature rather than the temperature at the center T_{aero}. The difficulty in determining the temperature uncertainty due to the variation in the gap width $2d$ in combination with the temperature sensor deviation of up to 0.4 K justifies the selection of a rather conservative uncertainty in the wall temperature ΔT of 0.5 K. Therefore, the possible minimum and maximum temperatures based on this wall temperature uncertainty ΔT are used as uncertainty of the INKA temperature measurement.

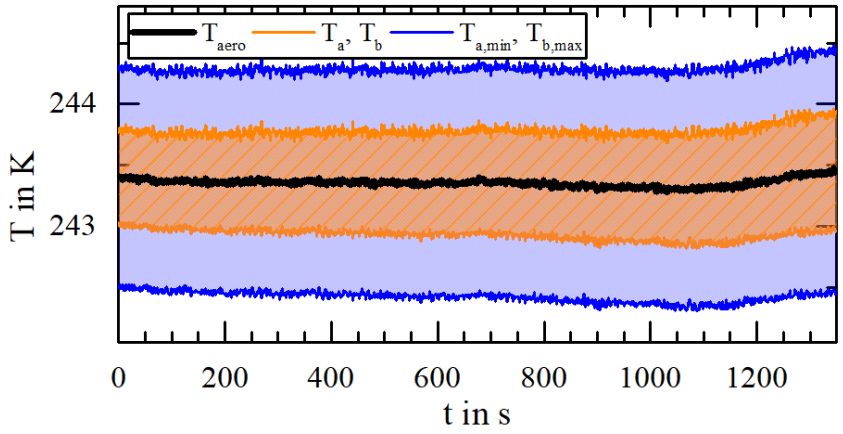

Fig. 3.20.: Temperatures during an INKA RH scan at 243.15 K. This figure shows the temperature T_{aero} at the center of the aerosol flow (black line), the temperatures T_a and T_b at the edges of the aerosol lamina (lower and upper orange line enveloping the orange-shaded, striped area) and the minimum and maximum temperatures, $T_{a,min}(T_{cold}-\Delta T, T_{warm}-\Delta T)$ and $T_{b,max}(T_{cold}+\Delta T, T_{warm}+\Delta T)$, at the edges of the lamina due to the uncertainty in the wall temperature ΔT (lower and upper blue line enveloping the blue-shaded area).

Humidity Uncertainty

The ice nucleation mode and the number of nucleating particles depends on the saturation ratio, which again is influenced by wall temperature irregularities. In this chapter, the uncertainty in water vapor concentrations based on the derived wall temperature uncertainty ΔT of 0.5 K will be calculated.

As for the temperature of the aerosol lamina, the influence of temperature irregularities on the water vapor saturation ratios along the lamina have also been carefully evaluated. Hereby, the simultaneous increase or decrease of the wall temperatures, which had the main influence on the lamina temperature, has only a minor influence on the saturation ratio, as water vapor concentrations are related to the equilibrium conditions at the now shifted lamina temperatures. The cold lamina edge saturation ratio $S_{liq,a,min}(T_{cold}+\Delta T, T_{warm}-\Delta T)$ is maximally decreased by increasing the cold wall temperature while decreasing the warm wall temperature (Fig. 3.21, lower blue line). The warm lamina edge saturation ratio $S_{liq,b,max}(T_{cold}-\Delta T, T_{warm}+\Delta T)$ is influenced the most by decreasing the cold wall temperature while increasing the warm wall temperature (Fig. 3.21, upper blue line). The mean difference in the saturation ratio $S_{liq,aero}$ between the center of the lamina and the edges $S_{liq,a}$ and $S_{liq,b}$ is less than $\pm 0.5\,\%$ for an INKA RH scan at 243.15 K (Fig. 3.21, orange lines enveloping the orange-shaded, striped area). When taking into account the wall temperature uncertainty ΔT, the possible minimum and maximum values $S_{liq,a,min}$ and $S_{liq,b,max}$ differ on average by $\pm 3.9\,\%$ from $S_{liq,aero}$ for the same example (Fig. 3.21, blue lines enveloping the blue-shaded area).

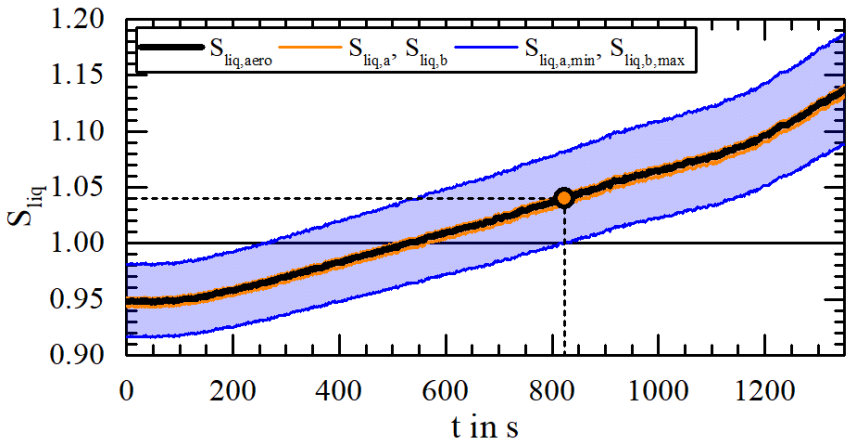

Fig. 3.21.: Saturation ratios with respect to liquid water during an INKA RH scan at 243.15 K. This figure shows the saturation ratio $S_{liq,aero}$ at the center of the aerosol flow (black line), the saturation ratios $S_{liq,a}$ and $S_{liq,b}$ at the edges of the aerosol lamina (lower and upper orange line enveloping the orange-shaded, striped area) and the minimum and maximum saturation ratios, $S_{liq,a,min}(T_{cold}+\Delta T, T_{warm}-\Delta T)$ and $S_{liq,b,max}(T_{cold}-\Delta T, T_{warm}+\Delta T)$, at the edges of the lamina due to the uncertainty in the wall temperature ΔT (lower and upper blue line enveloping the blue-shaded area). The orange circle indicates the time of the RH scan and the aerosol saturation ratio at the center of the lamina, where all particles of the lamina are exposed to water saturation considering the wall temperature uncertainty.

The wall temperature uncertainty has a significant influence on the interpretation of the INKA data. Even if all sampled particles are inside the aerosol lamina, the wall temperature uncertainty ΔT causes a large spread over the scanning time until all particles are exposed to water saturation (Fig. 3.21, 265 s<t<824 s). Further, in case of a RH scan at 243.15 K, a liquid-water supersaturation of 4 % at the center of the aerosol lamina is required until all particles are surely exposed to a relative humidity above water saturation and one can interpret the ice nucleation process as immersion freezing (Fig. 3.21, orange circle). Since INKA's ΔT is relatively small compared to CFDCs without automated temperature control, the saturation ratio uncertainty of those CFDCs might be even higher.

The variation of the CFDC gap width $2d$ causes a rather slight difference in the saturation ratio with respect to liquid water of 0.8 % (Fig. 3.19), in case of a cold wall temperature of 237.7 K, a warm wall temperature of 253.5 K, a total flow of 12.51 min^{-1} and a chamber pressure of 995.6 hPa. Nevertheless, a mean out of the minimum and maximum d values is used for the data analysis in order to consider its change over the course of an experiment.

Due to the relatively small difference between the saturation ratio at the edges a and b of the aerosol lamina, the saturation ratio at the center of the aerosol lamina $S_{liq,aero}$ is used for data analysis. For the INKA saturation ratio measurement, a rather conservative uncertainty of ± 5 % is determined. This value considers the possible minimum and maximum values resulting from the wall temperature uncertainty ΔT and the saturation ratio variation due to the uncertainty in the chamber gap width $2d$.

INP Measurement Uncertainty

Setting the ice threshold properly is very crucial for the INKA data analysis, because it can cause differences of orders of magnitudes in the INP concentration. During the RH scan, INKA sometimes does not only detect ice particles in the larger channels of the OPC but to some aerosol-dependent amount also in the lower channels (Fig. 3.17, panel 2, *small ice*). These *small ice particles* might be formed from small droplets which partly survive the evaporation section (DeMott et al., 2015). There, they might experience a temperature drop of up to a few Kelvin since the evaporation section temperature equals the cold wall temperature. This then possibly induces additional immersion freezing of droplets prior to evaporation, but at the temperature of the evaporation section rather than at the relatively higher temperature analyzed by the INKA RH scan. This effect is more prominent for higher saturation ratios (Fig. 3.22), because the possibility of small droplets surviving the evaporation section is larger and the temperature drop in the evaporation section is getting more pronounced (DeMott et al., 2015). Further, this artifact occurs more

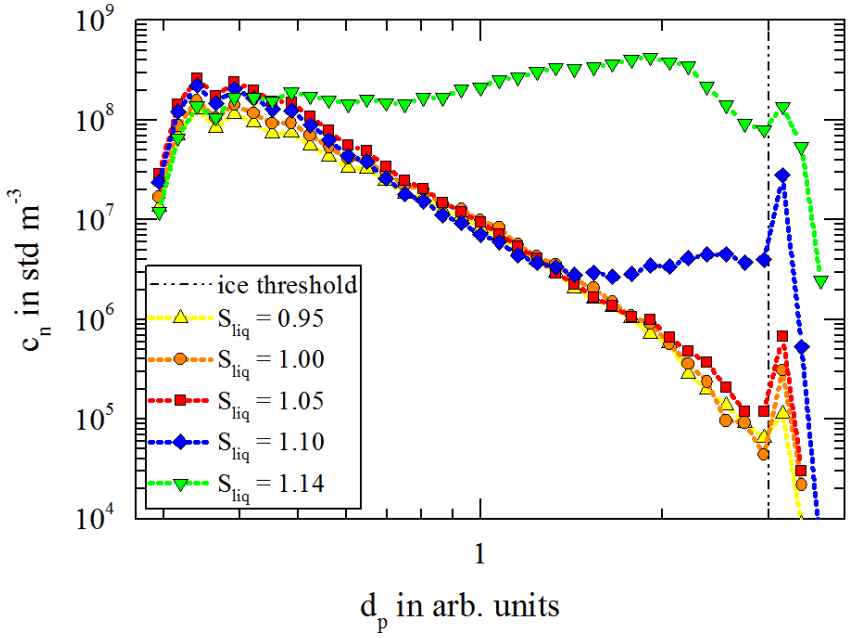

Fig. 3.22.: Size distribution of detected particles during a stepwise RH scan at 248.15 K aerosol temperature of illite NX. The vertical, black line indicates the set ice threshold. The particle number concentrations c_n are not background corrected in this case. At S_{liq} = 1.10 *small ice* is visible between the aerosol and the ice mode. At S_{liq} = 1.14 the droplet breakthrough is already very advanced and influences the whole size range.

prominent for samples with a strong temperature-dependent freezing activity such as feldspar (Atkinson et al., 2013). To avoid erroneous counts of ice formed at lower temperatures than investigated, the ice threshold is set above these particles and they are not considered in the INKA data analysis (Fig. 3.17 and Fig. 3.22). Due to this conservative approach, the minimum INP number concentration is reported with the possibility of underestimating the ice nucleation activity. This possible uncertainty in INP number

concentration is difficult to predict and will not be quantified in this thesis. Further discussions related to this topic can be found in DeMott et al. (2017b).

The INKA analysis is stopped at a liquid-water supersaturation of 5 % prior to the droplet breakthrough. This also might cause an underestimation of the INP number concentration, but the uncertainty is difficult to quantify and will not be considered in the INKA INP uncertainty. Analogously to other optical particle counters, the uncertainty of the Climet OPC in detecting ice particles is assumed to be ±20 % (Wagner and Möhler, 2013). The ice background of each single INKA measurement is determined. Although, this value is already considered in the data analysis and is already used as significance check, it is additionally considered as INP measurement uncertainty.

Altogether, the uncertainty of the INKA INP measurement is a combination of the Climet OPC uncertainty and the measurement background.

INAS Density Uncertainty

For INKA studies, the aerosol characterization of the AIDA facility is used. The measurement uncertainty of this instrumentation in determining the aerosol surface concentration is ±34 % (Ullrich et al., 2017). The error propagation of this uncertainty and the uncertainty in the INP measurement yields then to the uncertainty in the INAS density obtained from INKA measurements.

3.3.3. Validation of Instrument Performance

Immersion freezing results of illite NX are used to validate the INKA measurement against other INP measurement methods in the literature (Broadley et al., 2012; Hiranuma et al., 2015). Therefore, the temperature range between T_a and T_b, at the edges a and b of the aerosol lamina, is interpreted as freezing temperature (see Sec. 3.3.2). The INP concentration at the liquid-water supersaturation of 5 % prior to the droplet breakthrough is used to calculate the INAS density which is interpreted as immersion freezing result (see Sec. 3.3.2 for details). The results together with the measurement uncertainties are listed in Table 3.2. The intercomparison shows that INKA is in very good agreement with the two

Tab. 3.2.: INKA immersion freezing results for illite NX, which are shown in Figure 3.23. T_{aero} is the temperature at the center of the aerosol flow, T_a and T_b are the temperatures at the edge of the aerosol lamina and $T_{a,min}$ and $T_{b,max}$ are the possible minimum and maximum temperatures at the edges of the lamina due to the uncertainty in the wall temperature. n_s is the INAS density with its uncertainty Δn_s.

T_{aero} in K	T_a in K	T_b in K	$T_{a,min}$ in K	$T_{b,max}$ in K	n_s in m^{-2}	Δn_s in m^{-2}
248.42	247.95	248.89	247.44	249.40	4.17E+08	3.54E+08
245.91	245.43	246.38	244.92	246.89	2.92E+09	1.49E+09
243.34	242.87	243.81	242.36	244.32	1.29E+10	5.10E+09

well-established methods AIDA and CSU-CFDC (Fig. 3.23). The three methods suggest a similar tem-

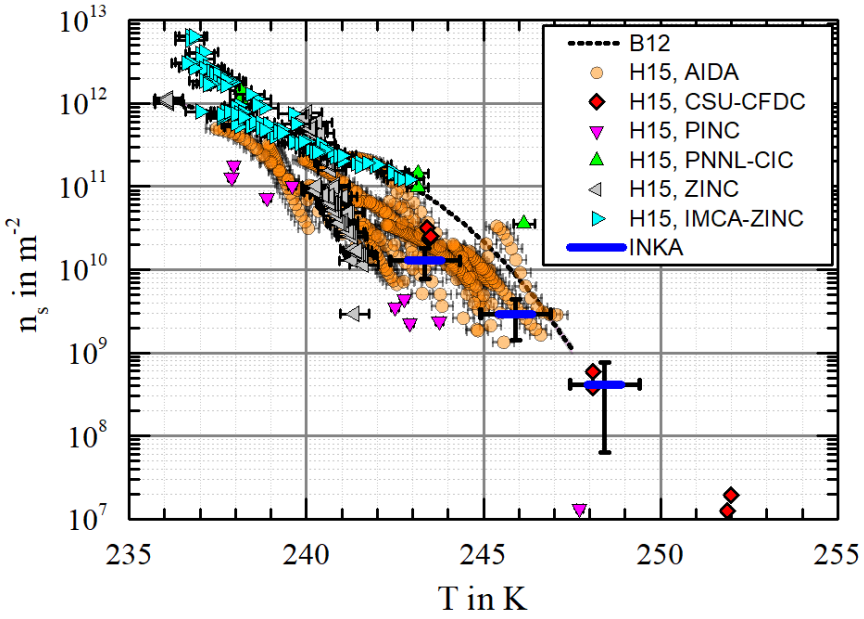

Fig. 3.23.: INKA immersion freezing results (blue bars, Tab. 3.2) for illite NX in intercomparison with other INP counters and other methods from the literature (B12: Broadley et al. (2012), H15: Hiranuma et al. (2015)).

perature dependency of the ice nucleation activity as well as INAS densities in the same range. Since the CSU-CFDC usually uses the measured INP concentration at 5 % supersaturation with respect to liquid water, one would expect lower values compared to INKA, which usually uses higher supersaturations. But for the measurements in Hiranuma et al. (2015), the ice threshold of the CSU-CFDC was set to a smaller value than in the RH scans of FIN-2. This might explain why the CSU-CFDC values are after all higher than the INKA results. Most of the INP measurement methods (AIDA, PINC, PNNL-CIC, ZINC and IMCA-ZINC) report also immersion freezing data at temperatures far below 243.15 K. For INKA, immersion freezing results below this temperature are not reported, because of the possibility of homogeneous freezing in the evaporation section of the CFDC. In addition, for temperatures higher than 248.15 K, INKA does not detect significant ice particle numbers for illite NX.

3.4. The Freezing Array INSEKT

The ice nucleation spectrometer of the Karlsruhe Institute of Technology (INSEKT) is an offline immersion freezing method, where collected aerosol particles are suspended in clean water and small volumes of this aerosol suspension are investigated on their ice nucleation activity in order to obtain INP temperature spectra. The instrument is based on the CSU-IS design, which was originally developed by Hill et al. (2014, 2016) and will be described in Section 3.4.3.

3.4.1. Working Principle

The main part of INSEKT consists of two 96-well aluminum incubation blocks for PCR plates (VWR). These blocks are modified by milling of 13 mm wide channels into the bottom part, through which cooling liquid (ethanol) from a chiller (LAUDA Proline RP 890 in combination with a LAUDA command module) is pumped. The aluminum blocks ensure a good heat transfer to inserted sterile PCR plates, which contain small volumes of the aerosol suspension. The long sides of the blocks are interconnected and the whole part is placed in a custom-made PVC (polyvinyl chloride) box (Fig. 3.24). At the sides and at the bottom, the space between the blocks and the box is filled with 2 cm of Armaflex insulation material. The box has a removable lid with an antireflection coated glass pane. The lid prevents the samples from external contamination. A cooled, synthetic air flow of about $1\,\mathrm{l\,min^{-1}}$ passes over the samples, in the space between the PCR trays and the glass, in order to prevent condensation. This facilitates enclosing the samples within a dry and clean environment. The temperature during the experiment is monitored with several temperature sensors (see below). Further, a second dry synthetic air flow is passed over the glass pane in order to prevent condensation and thus to enable a clear visualization of the samples. The temperature is controlled and monitored by a custom-made LabVIEW program.

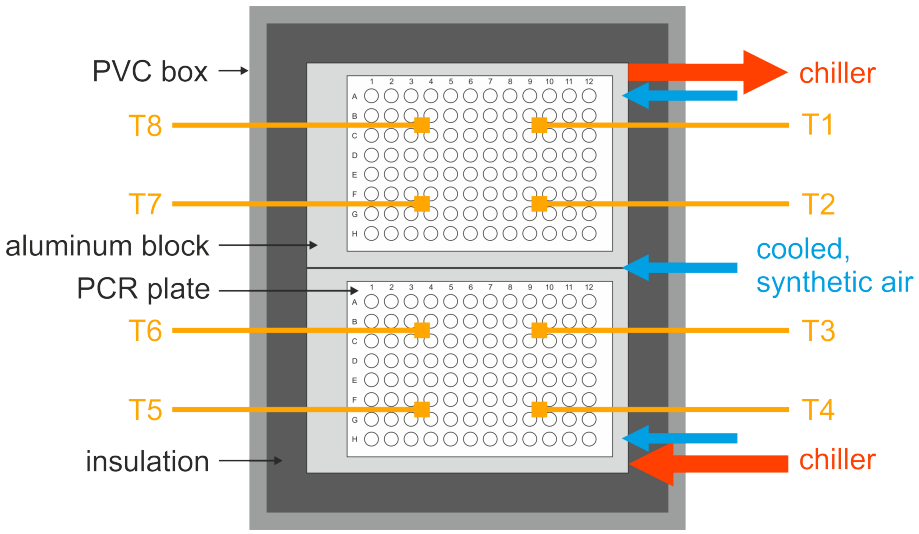

Fig. 3.24.: Schematic of the INSEKT top view. The main part of INSEKT, the two 96-well aluminum blocks, are placed inside a closed PVC box. The red arrows indicate the flow direction of the chiller. The temperature is monitored by eight temperature sensors (orange squares).

Temperature Measurement

The temperature of INSEKT is measured with a 1 Hz resolution by eight temperature sensors (Pt100). In the aluminum blocks, the sensors are vertically positioned inside holes, which are drilled between the cooling channels and the sample, at a height directly below the wells (Fig. 3.25). Horizontally, they are

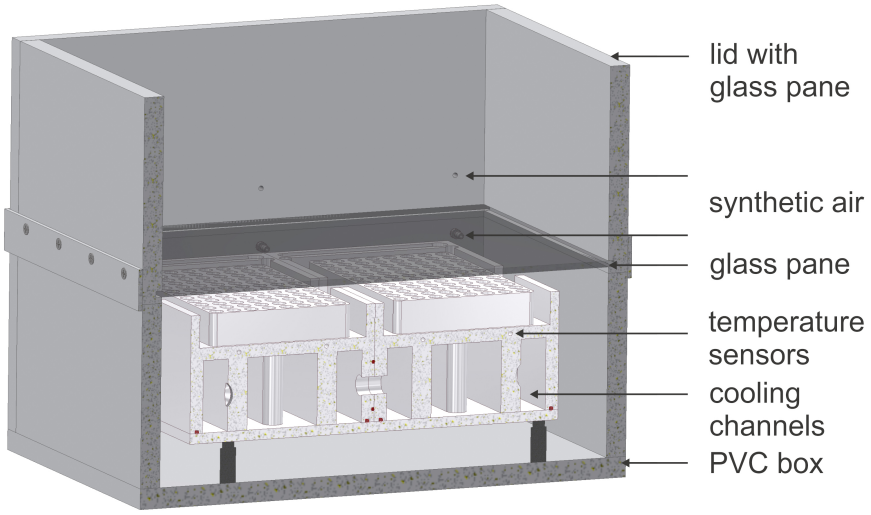

Fig. 3.25.: Schematic of the INSEKT side view. The main part of INSEKT, the two 96-well aluminum blocks, are placed inside a closed PVC box. The lid is equipped with a glass pane so that the freezing of the aerosol samples can be monitored. Technical drawing courtesy of Steffen Vogt.

shifted 4 cm towards the center of the aluminum block (Fig. 3.24).

To achieve high accuracy, the temperature sensors are calibrated against a certificated reference sensor (Lake Shore, PT-103-14L) (Dietel, 2017). For this purpose, the INSEKT temperature sensors are placed together with the reference sensor inside the cooling liquid of a chiller. To ensure a proper heat transfer, the sensors are additionally placed in holes drilled in a custom-made aluminum block. The temperature of the chiller is then stepwise decreased in 10 K steps starting at about 273.15 K and is kept at the set temperature for about 30 min. The temperatures are then averaged for the last 25 min, where the bath temperature of the chiller is stabilized.

Compared to the reference sensor, the raw temperature readings of all INSEKT sensors was lower in the entire temperature range. This deviation increased with decreasing temperature and reached a value of up to 0.6 K for the typical INSEKT minimum temperature of 248 K (Fig. 3.26, panel 1). However, the fluctuation between the individual sensors compared to a fit to all sensors is rather low with a maximum of 0.05 K (Fig. 3.26, panel 2).

Linear fits to the individual INSEKT sensors were then used to quantify the deviation from the actual temperature T_{ref} measured by the reference sensor. The raw temperature T_{raw} from the individual sensors is then corrected with the following equation:

$$(T_{corr} - 273.15\,K) = a + b(T_{raw} - 273.15\,K) \qquad [3.17]$$

The intercept a and the slope b of the individual sensors are listed in Table 3.3. Since the calibration measurement was conducted after the INP measurements shown in this thesis, the mean fit of all sensors

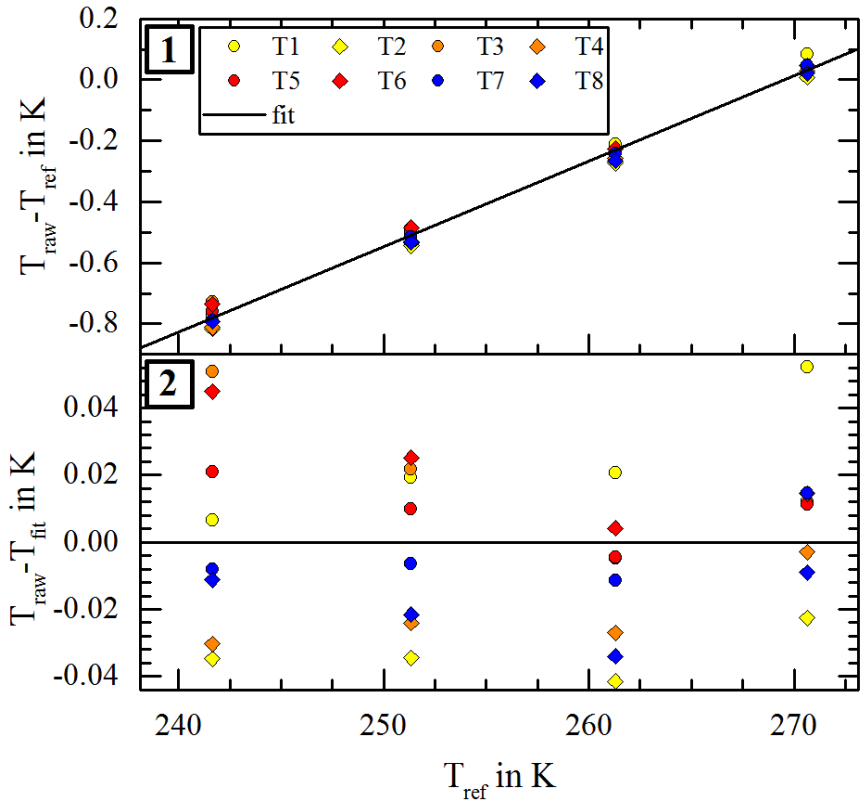

Fig. 3.26.: Temperature calibration of the INSEKT sensors. Panel 1 shows the deviation of the individual sensors (colored symbols) from the actual temperature measured by the reference sensor together with a fit to all sensors (sold, black line). Panel 2 shows their deviation from the fit. Data from Dietel (2017).

(Tab. 3.3, T_{all}) was used for a post-correction of the INSEKT data shown in this thesis.

Since the temperature is continuously changing in the course of the experiment, it is important to determine the temperature deviation of the single INSEKT sensors from the mean temperature under dynamic conditions. This deviation is caused by a non-uniform cooling rate throughout the freezing array of INSEKT and may therefore increase with decreasing temperature and depend on the cooling rate. For a typical immersion freezing experiment with a cooling rate of -0.33 K min^{-1}, the individual sensors typically deviate less than 0.1 K from the mean temperature. In the course of the experiment, this deviation might rise to a maximum of 0.3 K deviation at the very end of an experiment (Fig. 3.27). The temperature of the aluminum block (Fig. 3.24; T3 to T6), where the cooling liquid is entering the instrument, is slightly lower than the average temperature, whereas the other block (Fig. 3.24; T1, T2, T7 and T8) has a slightly higher temperature over the entire time of the experiment. This has also been seen in INP measurements (Dietel, 2017), where pure water samples froze earlier in the block where the cooling liquid is entering than in the other one. Further, the ice nucleation process might also contribute to

Tab. 3.3.: Linear fit parameters for the INSEKT temperature correction based on a temperature calibration with a reference sensor.

sensor	intercept a	sigma of intercept Δa	slope b	sigma of slope Δb
T1	-0.146	0.009	0.9714	0.0004
T2	-0.071	0.008	0.9725	0.0004
T3	-0.09	0.02	0.9742	0.0008
T4	-0.091	0.008	0.9720	0.0004
T5	-0.10	0.01	0.9732	0.0005
T6	-0.10	0.01	0.9739	0.0005
T7	-0.11	0.01	0.9722	0.0005
T8	-0.08	0.01	0.9728	0.0006
T_{all}	-0.10	0.01	0.9728	0.0005

the temperature deviation due to heat of crystallization. In the measurement data, a correlation between the fluctuation in temperature and a rapid onset of ice formation can be observed (Fig. 3.27 starting at 50 min, Fig. 3.28 starting at 3000 s).

Based on the deviation of the individual temperature sensors from their mean value under dynamic conditions, the temperature uncertainty ΔT of INSEKT is considered to be ± 0.3 K.

INP Measurement

For investigations of the ice nucleation activity of the sampled aerosol particles, the number of frozen samples is counted every 0.5 K.

The cumulative numbers of INP per volume of aerosol suspension, $c_{n,INP,liq}$, can be calculated from the number of unfrozen samples N_u as follows (Vali (1971), Eq. 15):

$$c_{n,INP,liq}(T) = -\frac{\eta}{V_{drop}} ln\left(\frac{N_u(T)}{N_{all}}\right) \quad [3.18]$$

Whereby η is the dilution, V_{drop} the droplet volume per investigated sample and N_{all} the number of all samples.

For the INP concentration, the INP number per sampled air volume results from:

$$c_{n,INP}(T) = -\frac{\eta}{V_{drop}} \frac{V_{wash}}{V_{air}} ln\left(\frac{N_u(T)}{N_{all}}\right) \quad [3.19]$$

Whereby V_{wash} is the volume of water used to suspend the aerosol particles and V_{air} is the volume of sampled air.

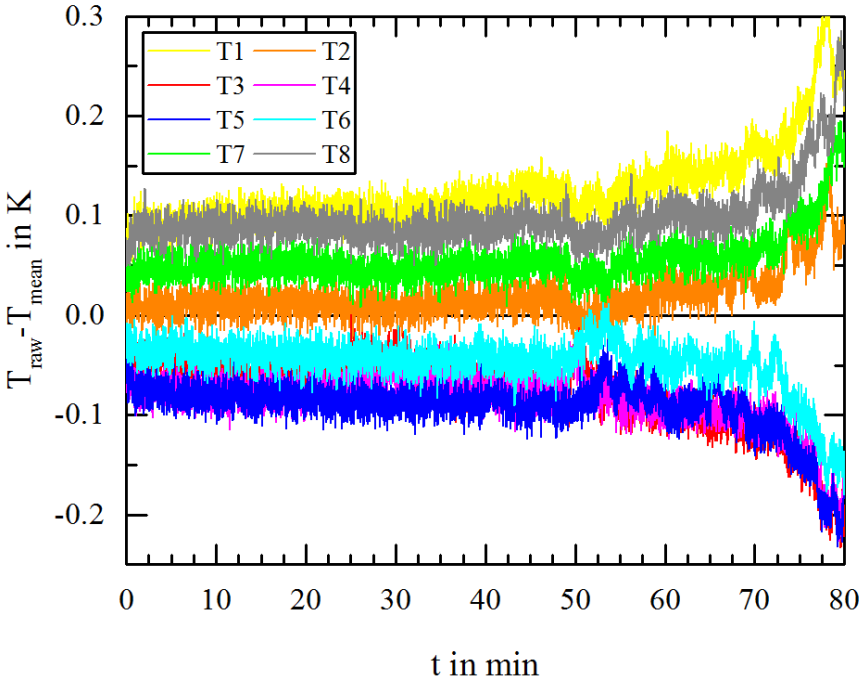

Fig. 3.27.: Dynamic deviation of the individual INSEKT sensors from the mean temperature in the course of an immersion freezing experiment with a cooling rate of -0.33 K min^{-1} starting at 273.15K (same experiment as shown in Fig 3.28).

Due to the relatively large droplet volumes of 50 µl, cleanliness in every sense is of great importance for INSEKT measurements. This means not only using clean water for the aerosol suspensions and dilutions, but also the preparation and the pipetting needs to be conducted in a clean environment. In addition, the PCR tray itself can cause ice nucleation on its surface or due to contaminates already introduced in the production process. These background INPs are for obvious reasons operator and day dependent and lower the sensitivity of INSEKT to detect the ice nucleation activity of the aerosol sample. To determine these background INPs, for each single experiment, a 6th or an 8th of the total number of aliquots are investigated with the cleaned water only. Considering the measured background leads to the following equation for the corrected INP concentration:

$$\begin{aligned} c_{n,INP,corr}(T) &= -\frac{\eta}{V_{drop}}\frac{V_{wash}}{V_{air}}\left(ln\left(\frac{N_u(T)}{N_{all}}\right) - ln\left(\frac{N_{u,bgr}(T)}{N_{all,bgr}}\right)\right) \\ &= -\frac{\eta}{V_{drop}}\frac{V_{wash}}{V_{air}}ln\left(\frac{N_u(T)}{N_{all} - \left(N_{f,bgr}\frac{N_{all}}{N_{bgr}}\right)}\right) \end{aligned} \quad [3.20]$$

$N_{u,bgr}$ is the number of unfrozen and $N_{f,bgr}$ the number of frozen samples, whereas $N_{all,bgr}$ is the number of all samples, all referring to the background measurement.

In addition to the background measurement with clean water, background filters are also collected and analyzed. They enable to determine the contamination due to the whole sampling and measurement procedure. These background filters undergo the very same processes as the normal sample filters. They

are pre-cleaned, placed in the filter holder at the measuring site, are packaged and stored frozen and are analyzed with INSEKT. For field measurements, the filters are placed inside the filter holder for a few minutes without pumping air through. In the laboratory, air from the clean chambers is sampled for the usual sampling time. For example, the INP concentration of the background filters during the particle collection at the CAO is in the order of $10^{-3}\,\mathrm{std}l^{-1}$ at an investigation temperature of 253.15 K, whereas the ambient INP concentration is in the order of $10^{-1}\,\mathrm{std}l^{-1}$ (based on CSU-IS measurements). The AIDA background filter shows a INP concentration in the order of $10^{-2}\,\mathrm{std}l^{-1}$ at 253.15 K, while the sampled INP concentration is in the order of $10^{2}\,\mathrm{std}l^{-1}$ (based on CSU-IS measurements). These background INPs are usually rather low, but nevertheless they are considered in the INSEKT data analysis.

For estimating the INP measurement uncertainty, 95 % binomial sampling confidence intervals $CI_{95\%}$ are derived using the Wilson interval (Agresti and Coull (1998), Eq. 2), which is especially appropriate for small sample numbers (n≤40, Brown et al. (2001)):

$$CI_{95\%,upper,lower} = \frac{1}{1+\frac{z^2_{\alpha/2}}{N_{all}}}\left(\hat{p}+\frac{z^2_{\alpha/2}}{2N_{all}} \pm z_{\alpha/2}\sqrt{\frac{\hat{p}(1-\hat{p})}{N_{all}}+\frac{z^2_{\alpha/2}}{4N^2_{all}}}\right) \qquad [3.21]$$

$\hat{p}$ is thereby the sample proportion of success, in case of INSEKT measurements the frozen fraction $\frac{N_f}{N_{all}}$. The $z_{\alpha/2}$ value is 1.96 for a 95 % confidence interval, which is determined by the (1-$\alpha/2$) quantile of the standard normal distribution (α=0.05 for a 95 % CI).

INAS Density

For INSEKT studies, the aerosol characterization of the AIDA facility is used. The measurement uncertainty of this instrumentation in determining the aerosol surface concentration is ±34 % (Ullrich et al., 2017). The error propagation of this uncertainty and the uncertainty in the INP measurement yields then to the uncertainty in the INAS density obtained from INSEKT measurements.

3.4.2. Typical Experiment

The investigated aerosol particles are first collected on filters in the laboratory or in the field (see Sec. 3.1.1 and 3.1.2 for details). These particles are then suspended in clean water (Sec. 3.1.2). The thus obtained aerosol suspension is diluted a few times, usually with 15- or 20-fold volumes of clean water. This allows measurement of the ice nucleation activity over a wide temperature range, down to temperatures as low as 248.15 K. The two 96-well PCR trays are partitioned into sections for the different samples: the neat aerosol suspension, the different dilutions and pure water (see Sec. 3.4.1 for details about the background measurement). Small volumes, usually 50 µl, of each of these samples are then pipetted into 24 to 32 wells of the 192 available wells of the PCR trays. The number of wells per partition depends on the number of dilutions. The prepared PCR trays are then placed in the aluminum blocks of INSEKT.

In order to investigate the ice nucleation behavior, the samples are cooled inside INSEKT. First, the temperature is lowered with a rather fast cooling rate of -1 K min^{-1} from room temperature to 273.15 K (Fig. 3.28, panel 1). Then, the actual immersion freezing experiment starts. Here, the cooling rate is lowered to -0.33 K min^{-1} in order to give the INPs inside the relatively large samples volumes time to initiate freezing.

The ice nucleation activity of the investigated sample is observed in 0.5 K steps. Depending on its ice nucleation efficiency, the first sample volume freezes already at a few degrees below 273.15 K, e.g. 266.25 K in case of the soil dust aerosol SDGe01, which is shown in Fig. 3.28. The most concentrated aerosol suspension freezes first, followed by the different dilutions from less diluted to more diluted (Fig. 3.28, panel 2). This results in an INP temperature spectrum showing the temperature-dependent INP concentration from freezing onset until temperatures as low as 248.15 K.

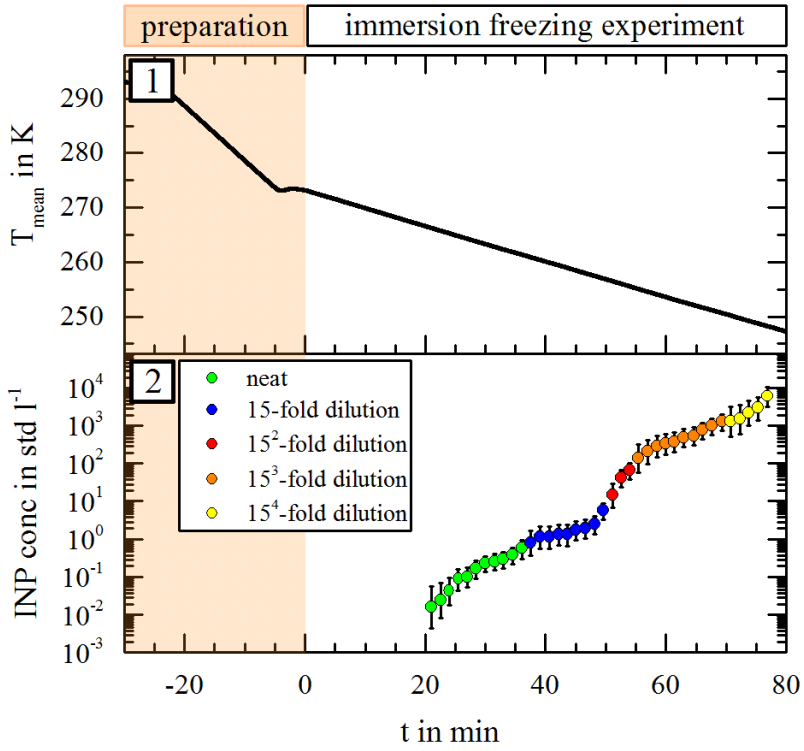

Fig. 3.28.: Data time series of a typical INSEKT experiment. Panel 1 shows the averaged temperature. Panel 2 shows the measured INP concentration achieved through the different dilutions of the aerosol sample.

3.4.3. CSU-IS and MINA

In addition to INSEKT, two further immersion freezing methods have contributed to the INP results shown in the scope of this thesis: the Colorado State University Ice Spectrometer (CSU-IS) (Hill et al., 2014, 2016) and the mono ice nucleation assay (MINA) (Pummer et al., 2015). Both instruments are based on the same method as INSEKT in a way that they also investigate comparable volumes of aerosol

suspensions by cooling them in PCR trays. In addition, the INP concentrations (Eq. 3.19) and uncertainties (Eq. 3.21) are derived with the same equations. Also, dilutions of the samples are prepared to broaden the accessible temperature ranges.

CSU-IS

The CSU-IS consists of two PCR aluminum blocks which are connected end-to-end and are surrounded by cold plates (see supplement of Hiranuma et al. (2015) for details). An acrylic plastic cover is placed above the samples and a dry, synthetic air flow between the samples and the glass guarantees a dry and clean environment during the measurement. The CSU-IS investigates the ice nucleation activity in 0.5 K steps with a cooling rate of -0.33 K min^{-1}, whereby it achieves INP concentrations for temperatures as low as 246.15 K. These INP results are corrected with INP measurements of background filters (see Sec. 3.4.1 for details).

MINA[3]

MINA consists of a single PCR aluminum block, which is temperature controlled by cooling liquid passing through channels inside the block. The block is placed in a closed insulation box with a window. Silica gel placed inside the box prevents condensation. For particle collection, quartz fiber filters are used. They can be easily pre-cleaned with heat, but they do not allow immersion freezing experiments below 258.15 K since at that temperature the fibers of the filters themselves start to nucleate ice. The samples are investigated by stepwise cooling in 2 K increments between 268.15 K and 258.15 K. For this purpose, MINA is kept at a set temperature for 12 min before the instrument is cooled down further. The MINA INP results are not corrected with background filters since the INP background is negligible for temperatures higher than 258.15 K.

3.4.4. Validation of Instrument Performance

For validation of the INSEKT performance, three different soil dust samples have been analyzed and are compared with the well-established CSU-IS.

For this purpose, the soil dust samples were dry-dispersed into the AIDA chamber. Aerosol particles were collected on filters and were shipped on dry ice to the Colorado State University. There, the particles were suspended and part of this aerosol suspension was analyzed with the CSU-IS. Afterwards, the rest of this generated aerosol suspension was shipped back to KIT on dry ice and were analyzed with INSEKT. Therefore, both instruments investigated the very same aerosol samples.

The comparison of the results obtained in this way show that the two instruments are, within measurement uncertainties, in very good agreement over the whole temperature range (Fig. 3.29a to 3.29c).

[3] All MINA measurements courtesy of Bernhard Pummer and Petya Yordanova (Max Planck Institute for Chemistry, Mainz, Germany).

The data slightly deviate where the measurement uncertainty is larger and come closer together where better statistics are available. One needs to keep in mind that even results from repeated measurements with the same instrument differ slightly from each other (Fig. 3.29d). The investigated temperature range of the two instruments is similar except that the CSU-IS usually is able to measure INP concentrations at temperatures about 2 K lower than INSEKT. Possible reasons for that could be a cleaner preparation environment at CSU or the use of different PCR trays. Both measurements have been conducted by the author of this thesis, so differences due to the operator can be ruled out.

3.5. Intercomparison of the Different Measurement Methods

To extend the temperature and humidity range of the INP results of this thesis, the different INP measurement methods which are described in this chapter are combined. In order to justify this, the different methods need to be compared first.

For this purpose, the German soil dust sample from Gottesgabe was dry dispersed into the AIDA chamber. Then, all methods sampled or collected the thus generated aerosol particles from the chamber and investigated the ice nucleation activity online or offline, respectively. Afterwards, the AIDA expansion experiment was conducted. By doing so, it is ensured that all methods investigated the identical aerosol sample. Since the measurements for the comparison are based on more than one AIDA experiment, the results are converted to an INAS density.

The comparison of the five different methods shows that all methods are in very good agreement over the whole temperature range (Fig. 3.30). The offline method MINA contributes results at higher temperatures between 266 K and 258 K. The two online methods AIDA and INKA have in general a higher detection limit and measure INP number concentrations at lower temperatures between 255 K and 247 K and between 253 K and 243 K, respectively. The two offline methods CSU-IS and INSEKT cover the whole temperature range starting at 266 K and measuring to temperatures as low as 246 K and 248 K, respectively. Thus, they fill the gap between the other methods and can be compared to all other methods. In general, the detection limit of the freezing arrays is relatively low due to their relatively large droplet volumes and the long particle collection time. This enables the instruments to detect the low ice nucleation activity at higher temperatures. Dilutions of the sample extend their temperature range. At 258 K, the MINA result is increased compared to the CSU-IS and the INSEKT result. One difference between MINA and the other two methods is that the freezing time in MINA is much larger, which gives the INPs more time to nucleate. Since the instruments agree very well at other temperatures this difference is unlikely to cause the discrepancy. A possible reason could be, that impurities that origin from the quartz fiber filter, which is used by MINA to collect the particles, already start to influence the measurement at this temperature.

Altogether, the very good agreement of the different measurement methods justifies combining their data in order to broaden the measurement range.

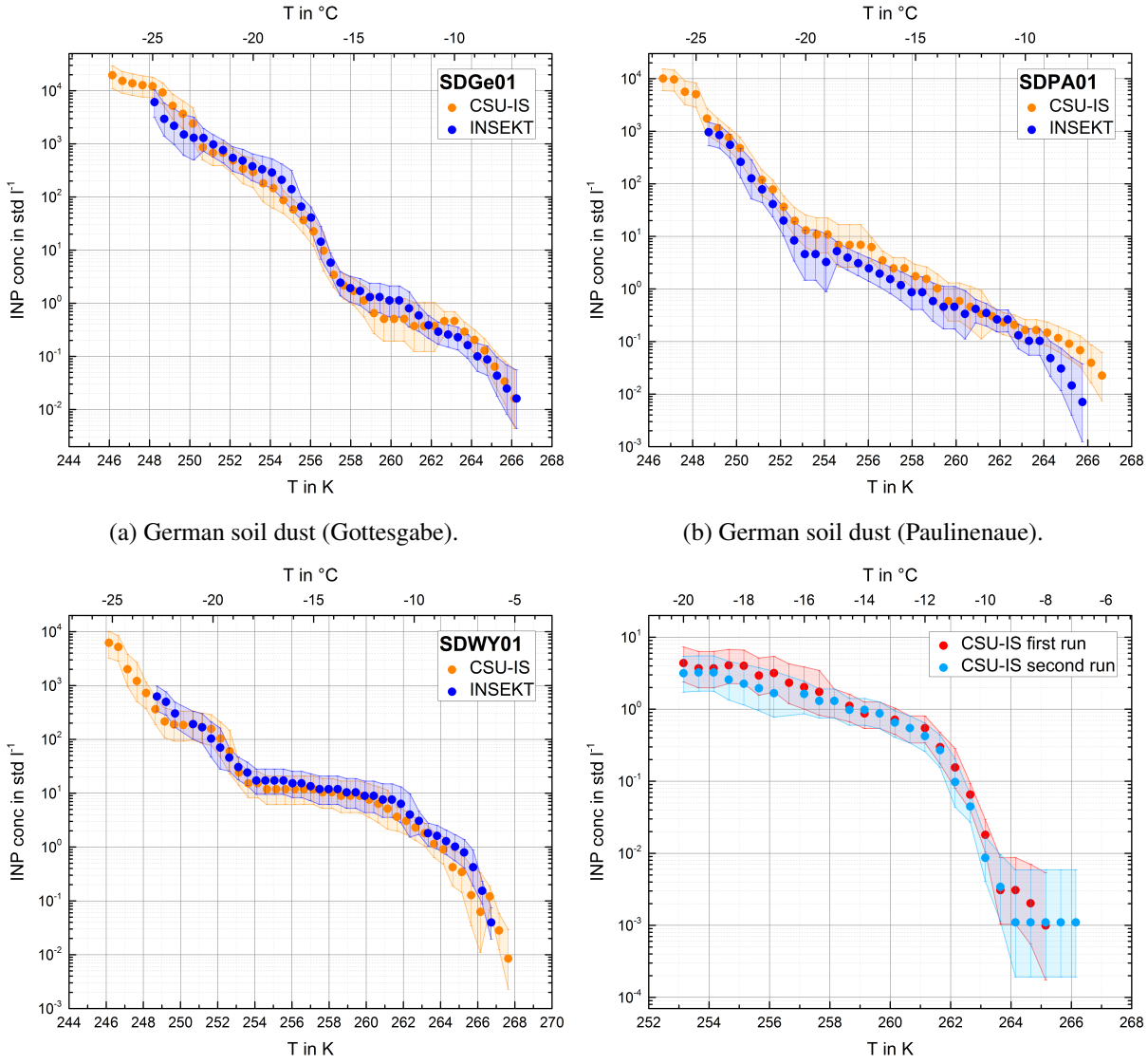

(a) German soil dust (Gottesgabe).

(b) German soil dust (Paulinenaue).

(c) Wyoming soil dust.

(d) Ambient sample from the CAO.

Fig. 3.29.: Intercomparison of CSU-IS and INSEKT measurements. (a)-(c) shows INP temperature spectra of both instruments for three different soil dust samples. For comparison, (d) shows two CSU-IS repeated measurements with the identical ambient aerosol sample.

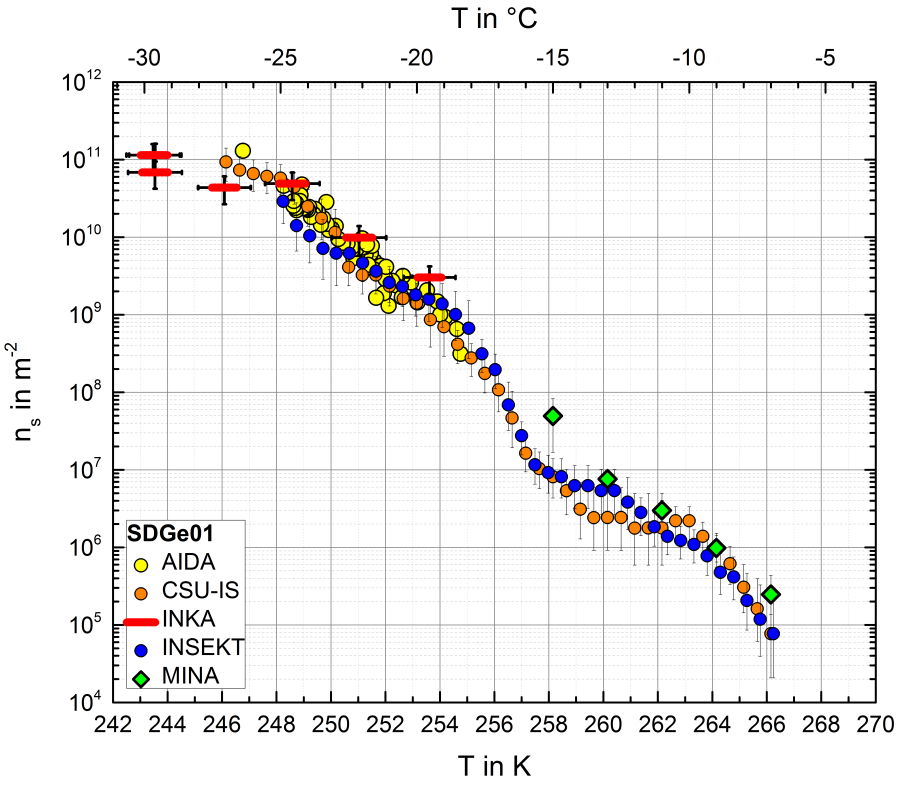

Fig. 3.30.: Intercomparison of the different INP measurement methods for the German soil dust from Gottesgabe. MINA measurements courtesy of Bernhard Pummer and Petya Yordanova (MPIC).

4. Ice Nucleation Activity of Arable Soil Dust Aerosol Particles

4.1. Introduction

Arable soil dust particles are originated from land, which is capable of being ploughed and used to grew crops, and are mainly emitted into the atmosphere by wind erosion or tillage operations. Single wind erosion events can thereby loft up to $100\,\mathrm{t\,ha^{-1}}$ (Buschiazzo and Funk, 2015), whereas tillage activities can lead to even larger dust emissions (Funk et al., 2008). During the last decades, the change of agricultural land use caused a significant increase in soil dust emission. Especially the tendency to larger fields and the destruction of the vegetation due to overgrazing strongly contribute to this change. Since the amount of arable soil dust emission varies according to location and season and also strongly depends on chemical and physical properties of the soil, it is difficult to quantify (Buschiazzo and Funk, 2015; Funk et al., 2008). During the aerosolization process, the coarse particles remain inside the soil, whereas very fine particles, such as particles of silt and soil organic matter, are lofted into the atmosphere. As a result, the emitted aerosol particles have a higher concentration in organic matter than the original soil (Buschiazzo and Funk, 2015).

Soil mineral dust aerosol INPs, mostly from deserts, are widely acknowledged to be important for ice formation in clouds. On the other hand, recent investigations with the cloud simulation chamber AIDA (Steinke et al., 2016) have shown that agricultural soil dust has an enhanced ice nucleation activity of up to a factor of 10 compared to similar experiments with desert dust (Ullrich et al., 2017), especially at temperatures above 247 K (Fig. 4.1). This enhancement appears to be caused by very ice-active primary biological particles, such as bacteria, fungal spores and pollen, as well as their cell-free INP proteins and other macromolecules (Hoose and Möhler, 2012; Fröhlich-Nowoisky et al., 2012; Pummer et al., 2015). Compared to desert dust particles, arable soil dust aerosol also contains a considerably higher amount of organic matter, derived from plants and the soil microflora, which further increases its ice nucleation activity (O'Sullivan et al., 2014; Tobo et al., 2014; Hill et al., 2016). Because of its complex mixture of mineral, biological and organic compounds, arable soil dust aerosol might be an important contributor to the ice formation in warm clouds.

To be able to assess the influence of arable soil dust aerosol on natural cloud formation, there is a need for more quantified information on its ice nucleation behavior and its origin. Here, comprehensive laboratory investigations will be presented, which aim to fundamentally understand and quantify the contribution of soil organics to aerosol ice nucleation activity. For this purpose, four different arable soil samples from different locations in the world have been investigated on their ice nucleation activity

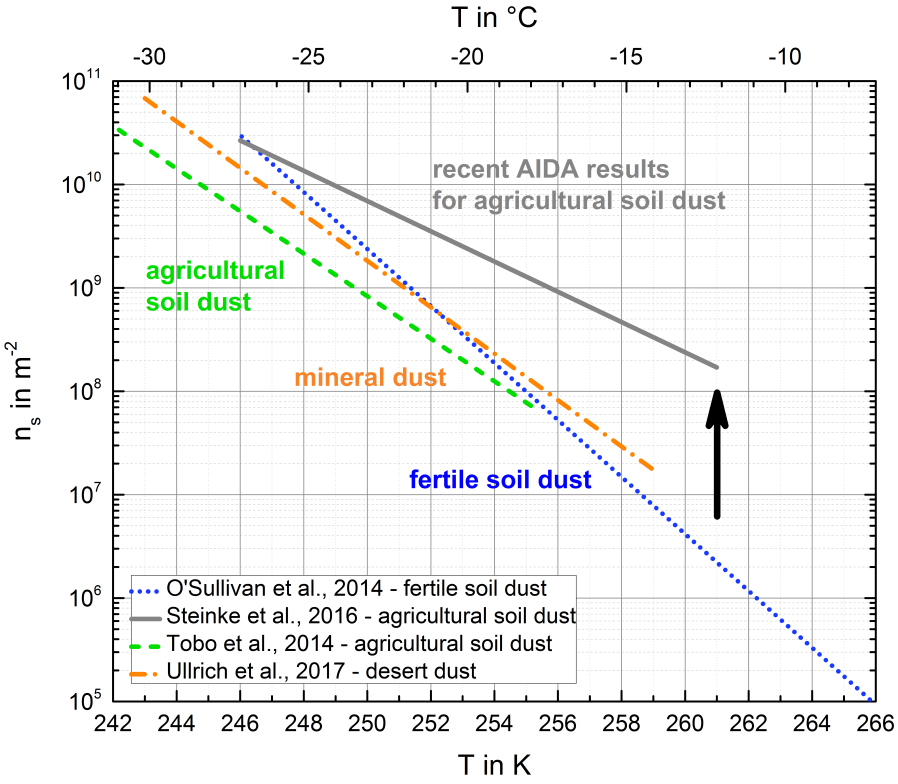

Fig. 4.1.: A recent study from (Steinke et al., 2016) suggested that agricultural soil dust has an enhanced ice nucleation activity compared to mineral dust and other agricultural and fertile soil dust parametrizations (Ullrich et al., 2017; O'Sullivan et al., 2014; Tobo et al., 2014).

(Sec. 4.2). Five different INP measurement methods have been combined in order to cover the entire temperature range of the mixed-phase cloud regime (Sec. 4.3.1). Those measurements have been supplemented by investigations on the contribution of soil organic matter on the ice nucleation activity of arable soil dust (Sec. 4.3.2) and a comparison with other results from the literature (Sec. 4.3.3). In addition, the ice nucleation behavior in the cirrus cloud regime has been investigated (Sec. 4.4), including the contribution of soil organic matter. The findings will be summarized in the last part of this chapter (Sec. 4.5).

4.2. Soil Dust Samples

For the comprehensive study of the ice nucleation activity of arable soil dust aerosol, four different soil dust samples have been investigated (Tab. 4.1). All of them are arable soil samples collected from the topsoil. They were dried and sieved (<75 µm), before they were aerosolized into the AIDA or APC chamber.

They origin from different locations in the world. The Argentinian soil dust (SDAr08) was collected from the Agricultural Experimental Station (INTA) in Anguil, La Pampa Province. The predominantly

Tab. 4.1.: Overview of the arable soil dust samples used for the ice nucleation experiments. The origin, the soil texture as well as the chosen particle density ρ_p and the dynamic shape factor χ of the four samples are listed. The soil samples from Germany and Argentina were provided by Roger Funk (ZALF), whereas the sample from the United States was provided by Thomas C. J. Hill (CSU).

Abbreviation	Origin	Latitude in °	Longitude in °	Soil Texture	ρ_p in $\mathrm{g\,cm^{-3}}$	χ
SDAr08	Argentina	-36.60	-63.96	silt	2.7	1.1
SDGe01	Germany	52.65	14.19	sand	2.6	1.3
SDPA01	Germany	52.69	12.74	peat	2.1	1.3
SDWY01	United States	41.03	−106.00	sand	2.7	1.1

silty soil origins from aeolian deposits. The German soil dust from Gottesgabe (SDGe01) was collected in Brandenburg from an arable, sandy land and origins from fluvial deposits (see Steinke et al. (2016) sample *GS* for further details). The second German soil dust (SDPA01) is from Paulinenaue, Brandenburg. This organic-rich degraded peat soil is from a former marsh area. The American soil dust from Wyoming (SDWY01) is collected from a sagebrush shrubland and consists of fine, loose sand (see Hill et al. (2016) for details).

In order to combine the aerosol size distributions measured by SMPS and APS (see Sec. 3.1.1 for details), different particles densities ρ_p and dynamic shape factors χ have been chosen. The values are close to or within the range of those observed for atmospheric mineral dust aerosol (Kaaden et al., 2009).

For organic matter pyrolysis, the soil samples have been exposed to 673 K dry heat in an oven (Sec. 3.1.3). The untreated as well as the heat-treated aerosol was then analyzed on its ice nucleation activity. Possible differences in the ice nucleation behavior provides information on the role of the organic matter to the ice nucleation activity of arable soil dust.

In order to investigate chemical changes in the samples caused by the heating, the untreated as well as the heat-treated aerosol particles have been analyzed with the single particle mass spectrometer LAAPTOF (Sec. 3.1.1). The relative change of the characteristic mass peak intensities due to the heat treatment has been categorized into three different size ranges of the aerosol particles: for vacuum aerodynamic diameters d_{va} smaller than 700 nm, between 700 nm and 1200 nm and larger than 1200 nm (Fig. 4.2). Independent of the soil sample and the particle size, the single particle mass spectrometer measurements show a significant increase of nitrogen-containing organic compounds with the marker peak at a mass-to-charge ratio m/z of 26 CN, while oxygenated organic compounds, such as organic acids with the marker peak at m/z 45 COOH, are reduced by more than 90 %. The relative increase of elemental carbon (C1-C7) is for most of the samples size-dependent with a higher significance for smaller particles. Thus, it is important to keep in mind that, although the heating significantly reduced the amount of

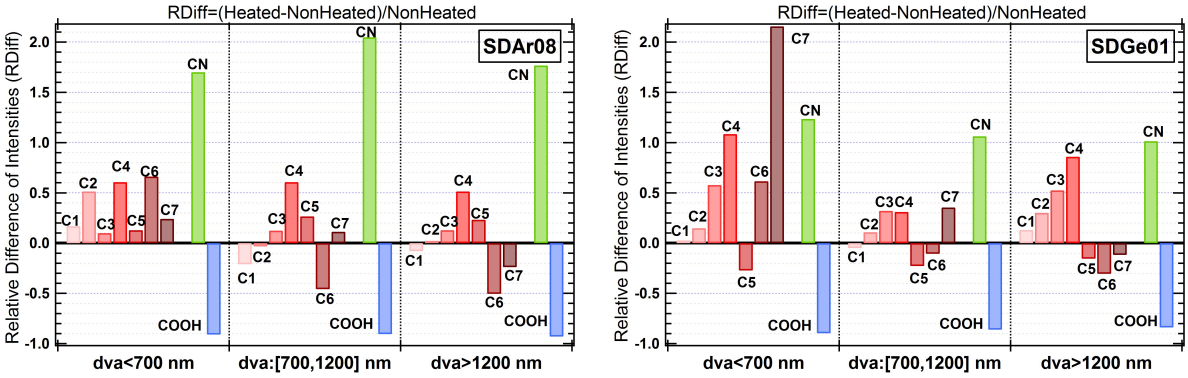

(a) Argentinian soil dust.

(b) German soil dust (Gottesgabe).

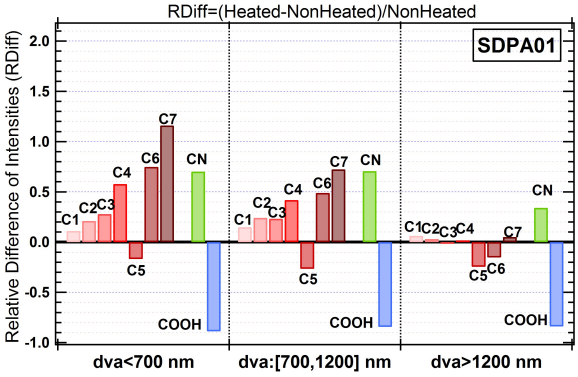

(c) German soil dust (Paulinenaue).

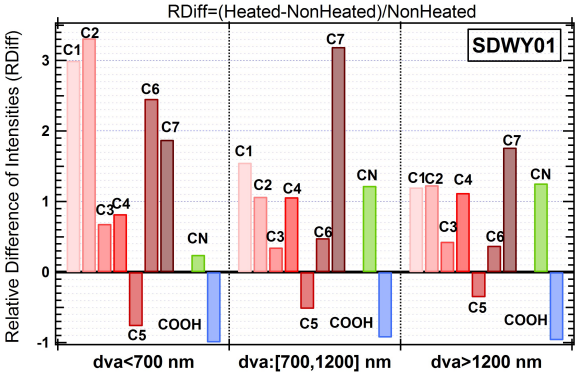

(d) Wyoming soil dust.

Fig. 4.2.: Relative change of the characteristic mass peak intensities due to the bulk heat treatment for three different size ranges of the aerosol particles. Measurements and diagrams courtesy of Xiaoli Shen.

organic compound in the samples, it produced a variety of pyrolysis products, which are still abundant in the samples. These products, like elemental carbon, might be present as separate particles or as a coating on other aerosol particles.

In addition to the heat treatment of the bulk material, 673 K aerosol heat treatment and 368 K aerosol suspension heat treatment have been applied on the soil dust samples, but there are no chemical analyses available.

4.3. Mixed-Phase Cloud Regime

To investigate the ice nucleation activity of arable soil dust in the mixed-phase cloud regime, numerous AIDA cloud expansion experiments at different starting temperatures have been conducted (Tab. 4.2). Other INP measurement methods sampled and collected aerosol particles for their analysis directly from the AIDA chamber prior to the expansion (Fig. 3.1).

Tab. 4.2.: Overview of the AIDA cloud expansion experiments conducted in the mixed-phase cloud regime. Name of the campaign, experiment number and start time are listed. The extension _ *ht300* indicates that the bulk sample was dry heated to 673 K, whereas _ *fh300* indicates that the aerosol heating tube was used with an aerosol temperature of 673 K. p_0, T_0 and $c_{n,0}$ are the pressure, temperature and aerosol number concentration at the beginning of the expansion.

Campaign	Experiment	Start time	Aerosol Type	p_0 in mbar	T_0 in K	$c_{n,0}$ in cm^{-3}
SOIL02	2	29.02.2016 13:48	SDPA01	1001.14	258.62	98
SOIL02	3	29.02.2016 20:04	SDWY01	1005.95	258.88	176
SOIL02	7	02.03.2016 13:33	SDGe01	988.28	258.53	148
SOIL02	8	02.03.2016 21:26	SDWY01	988.65	258.69	113
SOIL02	12	04.03.2016 14:35	SDGe01	984.18	260.49	93
SOIL02	17	08.03.2016 12:22	SDGe01_ ht300	1002.74	247.73	140
SOIL02	19	09.03.2016 12:16	SDGe01	994.35	255.89	128
SOIL02	20	09.03.2016 18:53	SDGe01_ ht300	993.40	256.18	163
SOIL02	21	10.03.2016 12:28	SDWY01	1003.35	255.95	172
SOIL02	30	16.03.2016 09:57	SDAr08	1009.27	255.90	331
SOIL02	34	18.03.2016 10:59	SDPA01	1007.67	255.93	96
SOIL02	36	21.03.2016 11:54	SDGe01	1005.49	258.65	185
SOIL02	37	21.03.2016 20:00	SDGe01_ fh300	1004.05	258.73	143

4.3.1. Ice Nucleation Activity

The combination of the five different INP measurement methods AIDA, CSU-IS, INKA, INSEKT and MINA (Chap. 3) allows to investigate the ice nucleation behavior of the four soil dust samples over a wide temperature range in the mixed-phase cloud regime. For this purpose, the measured ice particle number is normalized by the available aerosol surface. With the so-called INAS density n_s (see Sec. 3.2) different AIDA experiments and the different methods can be directly combined. In addition, this value accounts for the polydisperse aerosol size distribution and the related different aerosol sizes and aerosol surface areas of the single particles.

Depending on the soil sample, AIDA usually provides results for temperatures between 245 K and 256 K (Fig. 4.3, yellow circles). For the Wyoming soil dust (SDWY01) the AIDA data is scattering more than for the other samples (Fig. 4.3d). The CSU-IS covers the entire temperature range starting from ice nucleation onset to temperatures as low as 246 K and brings the measurement methods at higher and lower temperatures together (Fig. 4.3, orange circles). For the American soil dust from Wyoming, there is a second, smaller increase in the INP temperature spectrum visible at a temperature of about

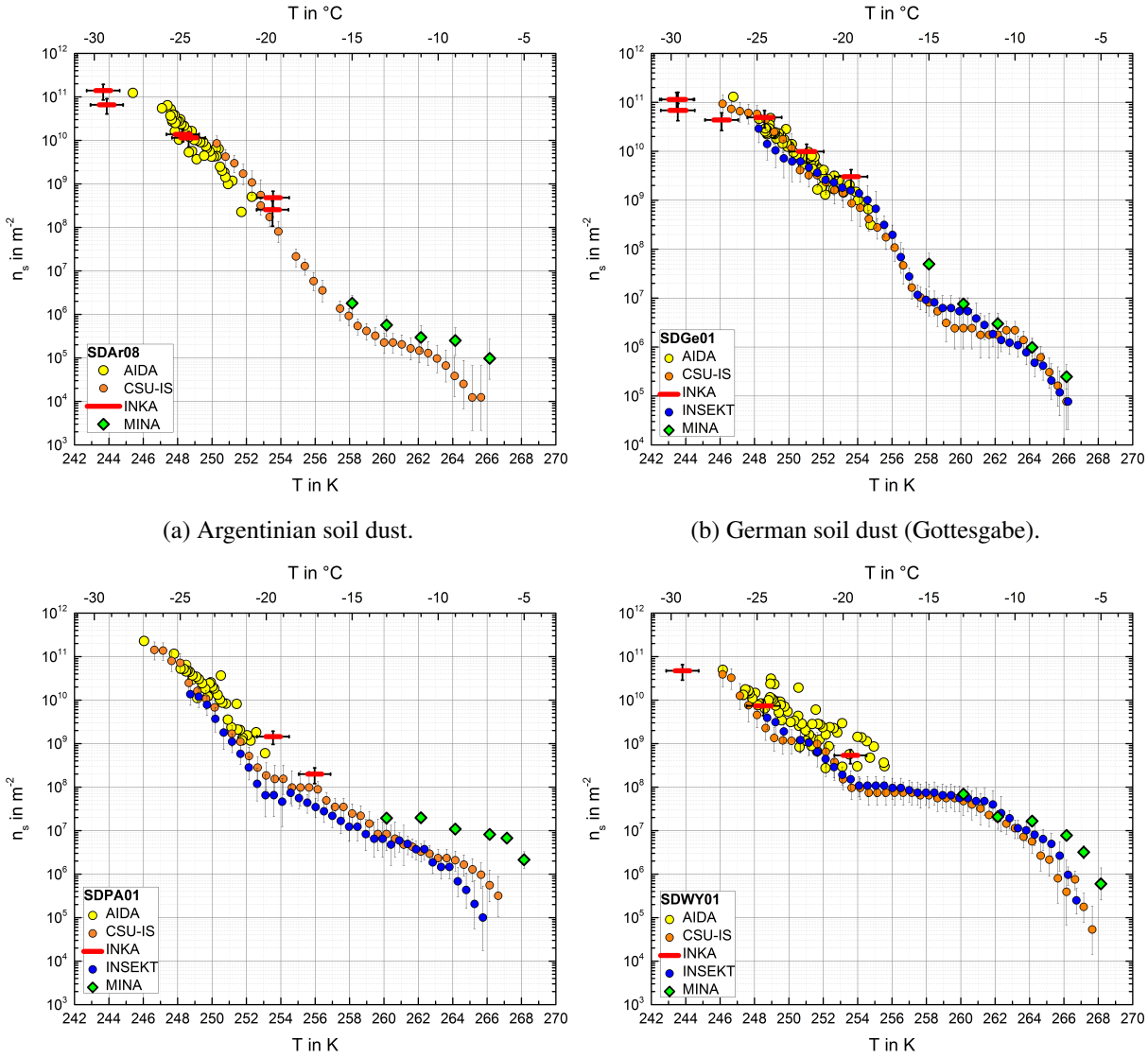

(a) Argentinian soil dust.

(b) German soil dust (Gottesgabe).

(c) German soil dust (Paulinenaue).

(d) Wyoming soil dust.

Fig. 4.3.: Temperature-dependent ice nucleation activity of four different arable soil dust aerosols. The combination of five different INP measurement methods allows to cover a wide temperature range. MINA measurements courtesy of Bernhard Pummer and Petya Yordanova (MPIC).

251 K. This enhancement is most likely caused by measurement inaccuracy, because it is not visible in the other methods (Fig. 4.3d). INKA is able to detect the ice nucleation activity of the soil dust samples for temperatures between 243 K and 253 K (Fig. 4.3, red bars). The results have a tendency to higher INAS density values at higher temperatures, but within error bars the data is in good agreement with the other methods. MINA covers a temperature range between 260 K and 268 K (Fig. 4.3, green diamonds). Especially at higher temperatures, MINA measures slightly increased n_s values. A possible reason could be the step-wise cooling method of the instrument and the thereby related longer residence time at the different temperatures. Another reason could be the increased collection volume compared to CSU-IS and INSEKT. This results in higher INP concentrations and might lead to better statistics. In general, the methods are in very good agreement (see also Sec. 3.5).

For all samples, the ice nucleation activity over the investigated temperature range consists of two regimes. This can be seen in the temperature spectra of INAS densities, when the near-log-linear curve at low temperatures changes to an increased curve at higher temperatures. At lower temperatures, the different soil dust aerosols seem to have comparable ice nucleation activities and the n_s values are relatively narrow. In this temperature range, the dominating INP is thought to be mineral dust particles. For higher temperatures, there is a larger variance between the four soil samples. The ice nucleation in this temperature range is thought to be dominated by organics. Especially SDPA01 and SDWY01 show an enhanced ice nucleation activity in this temperature range, whereas the activity of SDAr08 and SDGe01 is less pronounced. The transition from the one to the other temperature regime is at about 258 K for the Argentinian soil dust (SDAr08) and the German soil dust from Gottesgabe (SDGe01) (Fig. 4.3a and 4.3b). For the German soil dust from Paulinenaue (SDPA01) and the American soil dust from Wyoming (SDWY01), it is at about 253 K (Fig. 4.3c and 4.3d). Further investigations on the possible origin of the two temperature regimes will be discussed in Section 4.3.2).

4.3.2. Contribution of Soil Organic Matter

Different heat treatment methods have been applied in order to investigate the contribution of soil organic matter on the ice nucleation activity of arable soil dust aerosol. 673 K bulk and aerosol heating have been used as well as a more moderate conditioning at 368 K for the aerosol suspension (see Sec. 3.1.3 for details). The different INP measurement methods then probed the untreated and the heat-treated samples to determine possible influence on the ice nucleation activity.

The course of such intercomparison experiments will be discussed for the example of two AIDA expansion experiments both starting at 256 K and investigating the German soil dust from Gottesgabe untreated (Fig. 4.4, blue symbols) and bulk heat-treated prior to the experiment (Fig. 4.4, red symbols). Due to comparable starting pressures and identical initial pumping speeds, the decrease in pressure and temperature and the related increase in humidity are similar (Fig. 4.4, panel 1 and 2). While for the

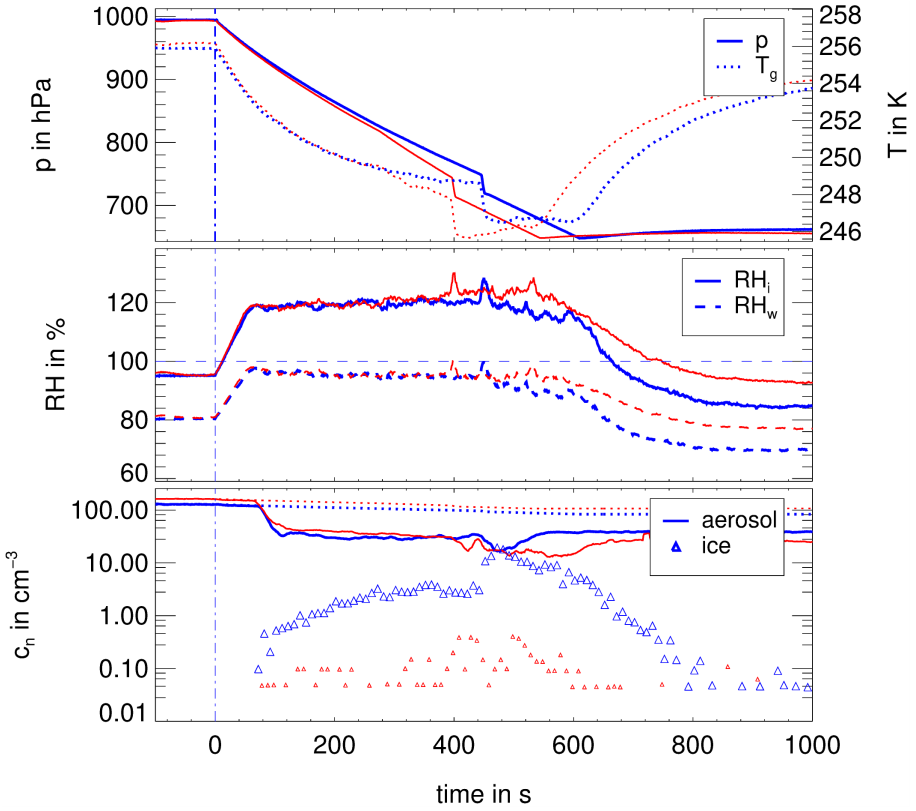

Fig. 4.4.: Data time series of two AIDA experiments in the mixed-phase cloud regime, both started at 256 K showing the German soil dust from Gottesgabe (SDGe01) with (red symbols) and without (blue symbols) heat treatment. Panel 1 shows the chamber pressure (left vertical axis) as well as the gas temperature (right vertical axis). Panel 2 shows the relative humidity with respect to liquid water and ice, respectively. Panel 3 shows the aerosol number concentration measured with the CPC as well as the total and ice number concentration calculated from the measured single particle data of the OPC. The vertical blue line indicates the start of the expansion experiments.

original sample already significant ice formation was observed 80 s after the start of the expansion, the ice formation of the bulk heated sample hardly exceeded the background threshold (Fig. 4.4, panel 3). This is why the pump speed needed to be increased (Fig. 4.4, panel 1, red curve at t = 280 s). After 400 s and 440 s respectively, a strong pressure and temperature drop was performed by opening the connection to the evacuated APC chamber (see Sec. 3.2.2 for details). This *APC jump* led to a sharp increase in ice formation for the original sample but nearly did not affect the heat-treated one. These two immersion freezing experiments started at 256 K show that the bulk heat treatment with 673 K strongly reduces the formation of ice (Fig. 4.4, panel 3).

To quantify the influence of the heat treatment methods over a wider temperature range, the results of the different INP measurement methods are combined. For the German soil dust from Gottesgabe, the 673 K bulk heat treatment causes a strong reduction of the ice nucleation active site density of two

orders of magnitude over the whole investigated temperature range (Fig. 4.5). Against expectations, the

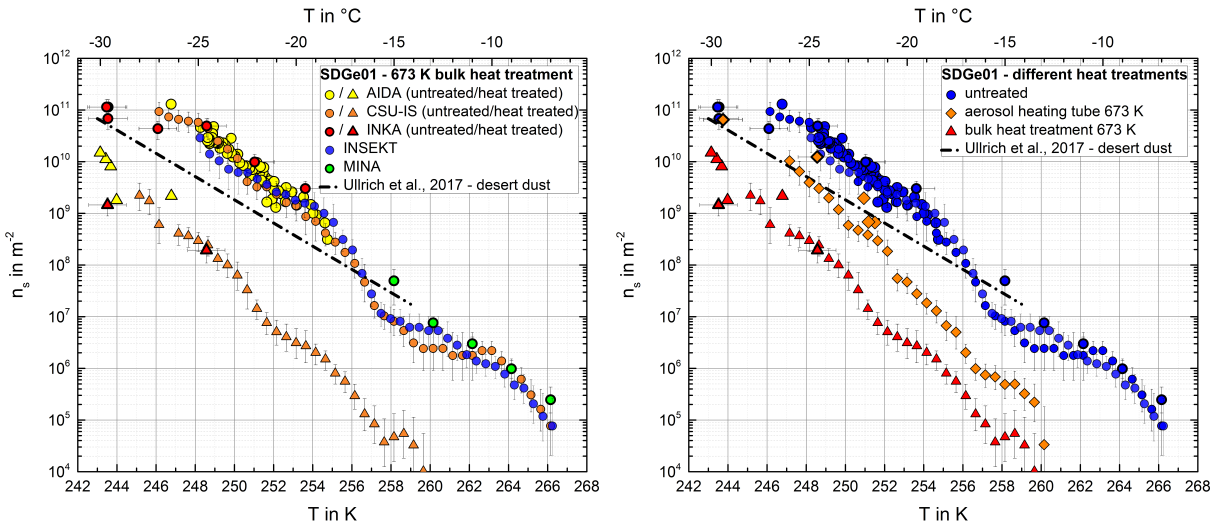

(a) Bulk heat treatment at 673 K.

(b) Aerosol heating tube at 673 K.

Fig. 4.5.: Influence of organic matter pyrolysis on the ice nucleation activity of the German soil dust from Gottesgabe in the mixed-phase cloud regime. (a) shows the difference between the untreated aerosol (circles) and the bulk heat-treated aerosol (triangles). (b) shows the untreated sample (blue symbols) in intercomparison with the sample, where the aerosol or the bulk was heat-treated prior to the experiment (orange symbols and red symbols, respectively). MINA measurements courtesy of Bernhard Pummer and Petya Yordanova (MPIC).

organic matter pyrolysis affects even temperatures below 253 K. Here, mineral dust particles are believed to dominate the ice nucleation, thus one would not expect the INAS densities to decrease below values suggested for mineral dust particles (Ullrich et al., 2017). To receive further information on this effect, bulk material of the untreated and the heat-treated soil sample have been analyzed on their mineralogy with X-ray diffraction (XRD). The analysis indicates that the rather strong heat treatment with 673 K has no effect on the minerals (personal communication with Peter Weidler). The LAAPTOF on the other hand detected an increase of elemental carbon due to the heat treatment. Based on these findings, the heat-treated sample seems to be a mixture of ash and minerals rather than pure mineral. This might influence the aerosol surface concentration and might therefore cause the unexpected impact on the INAS density below 253 K. Another possible reason could be that the bulk heat treatment not only removes the organics but also modifies the aerosol surface of the remaining particles, e.g. combusted material might cover ice nucleation active surface sites on the aerosol particles.

In addition, another heat treatment method has been used. Here, the aerosol rather than the bulk material is exposed to 673 K dry heat. The use of this aerosol heating tube reduces again the overall ice nucleation activity, but the decrease is less compared to the bulk heating method (Fig. 4.5b). In case of aerosol heat treatment, the reduction is in the order of one magnitude. This might be caused by the

relatively short exposure time in the order of seconds compared to the two hours of bulk heat treatment. It might also indicate that changes of the surface properties of the non-organic particles due to pyrolysis products is less compared to the bulk heating method, which would make the aerosol heating method more appropriate for the investigations conducted in the scope of this thesis. To confirm this, chemical analysis of the aerosol particles would be required.

For temperatures below 253 K, the INAS density drops to values close to those expected for mineral dust (Ullrich et al., 2017). The ice nucleation activity after the aerosol heat treatment is reduced to a log-linear curve, whereas especially the pronounced ice nucleation activity at higher temperatures is significantly reduced. After the organic matter pyrolysis, the dominating INPs are assumed to be mineral dust particles. Even if the heat-treated measurements are in good agreement with the mineral dust parametrization suggested by Ullrich et al. (2017) for temperatures below 253 K, they show an overall higher temperature dependence.

Since even the aerosol heat treatment method reduces the overall ice nucleation activity, a more moderate heat treatment method is applied as well to receive further information on the INPs. For this purpose the aerosol suspension of the CSU-IS sample is heated to 368 K prior to the analysis in order to denature proteinaceous INPs. The thus conducted heat treatment strongly influences the ice nucleation activity at higher temperatures for all four soil dust samples (Fig. 4.6), whereas for lower temperatures the procedure seems to have no effect on the INPs. Irregularities during the sample preparation caused errors in the dilutions and shift the heat-treated measurement of the Argentinian soil dust sample towards lower temperatures (Fig. 4.6a). When taking this into account, the heat treatment strongly reduces the ice nucleation activity at temperatures above 258 K. The German soil dust from Gottesgabe shows a similar ice nucleation behavior, but the temperature, above which the heat sensitive INPs dominate the nucleation is 259 K (Fig. 4.6b). The German soil dust from Paulinenaue has a different temperature spectrum. From its origin it is known that this sample is organic-rich (Sec. 4.2, personal communication with Roger Funk (ZALF)). This also shows a very pronounced ice nucleation activity down to temperatures as low as 253 K (Fig. 4.6c). Most of the enhanced INPs are resistant to the 368 K heat treatment, which only reduces the ice nucleation activity for temperatures above 260 K. The American soil dust from Wyoming also shows a very pronounced ice nucleation behavior for temperatures above 254 K (Fig. 4.6d). In contrast to the German soil dust from Paulinenaue, here, the ice nucleation is dominated by heat sensitive INPs. The rather moderate heat already has a strong influence on this temperature range. For all of the four different soil samples, the high temperature ice nucleation activity is controlled by heat sensitive INPs, which are possibly proteins or other macromolecules.

4.3.3. Comparison with Literature Data

In order to obtain an overview of the ice nucleation behavior of soil dust aerosol particles, the results for from this study are compared to soil dust parametrizations from the literature (Tab. 4.3). This in-

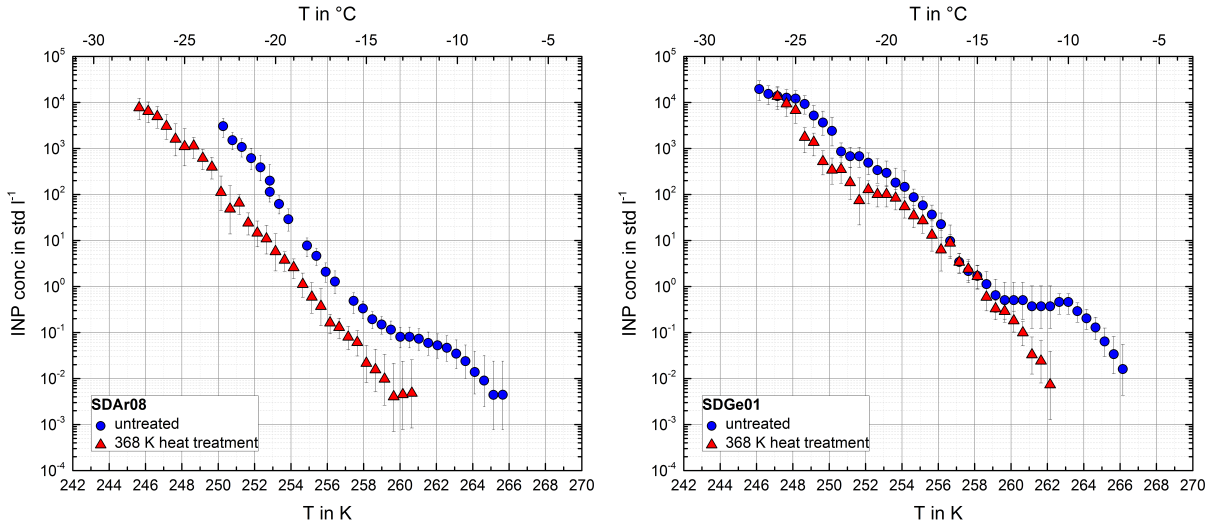

(a) Argentinian soil dust.

(b) German soil dust (Gottesgabe).

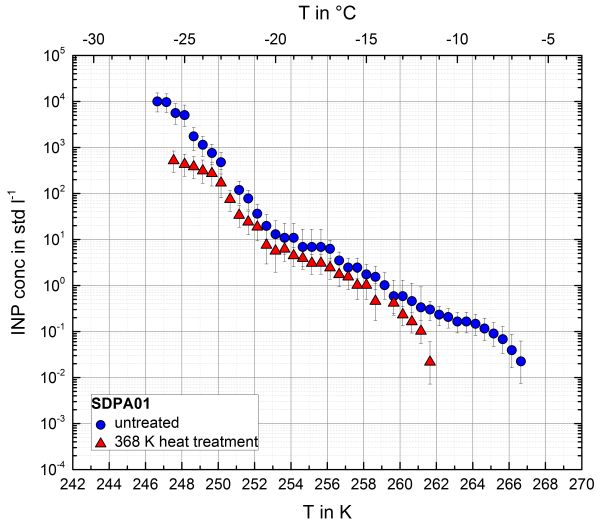

(c) German soil dust (Paulinenaue).

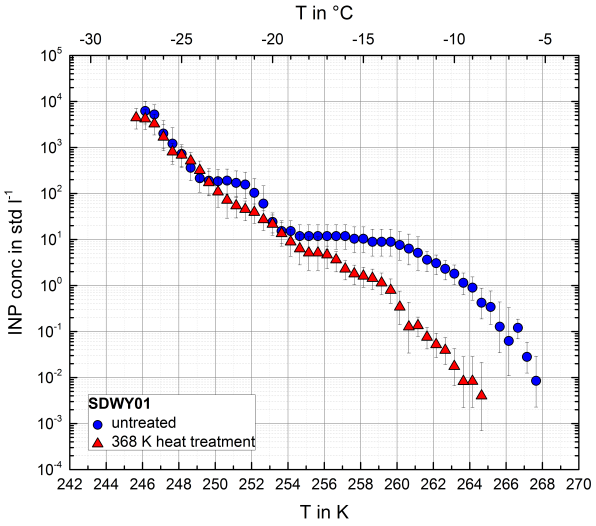

(d) Wyoming soil dust.

Fig. 4.6.: Influence of 368 K heat treatment on the ice nucleation activity of four different arable soil dust aerosols. The INP temperature spectra of both, the untreated (blue circles) as well as the heat-treated aerosol (red triangles), are shown.

Tab. 4.3.: Overview of soil dust parametrizations in the literature.

Publication	Sample	Instrumentation
O'Sullivan et al. (2014)	fertile soil dust	cold stage
Steinke et al. (2016)	agricultural soil dust	cloud chamber
Tobo et al. (2014)	agricultural soil dust	CFDC
Ullrich et al. (2017)	mineral dust	cloud chamber

cludes the fertile soil dust parametrization by O'Sullivan et al. (2014), which is derived from cold stage measurements. Tobo et al. (2014) provide an agricultural soil dust parametrization based on CFDC measurements. Steinke et al. (2016) recently investigated agricultural soil dust in the cloud simulation chamber AIDA, where also the mineral dust parametrization from Ullrich et al. (2017) is originated.

The combination of the INP measurements shows that for temperatures lower than 253 K, where the ice nucleation activity is most likely controlled by mineral components, the four different samples have a comparable temperature dependency and are lying within one order of magnitude of a log-linear fit (Fig. 4.7). This fit would have a higher temperature dependency of the ice nucleation activity compared to previous parametrizations from the literature (O'Sullivan et al., 2014; Tobo et al., 2014) as well as to the mineral dust parametrization by Ullrich et al. (2017). Even recent AIDA measurements with agricultural soil dust (Steinke et al., 2016) suggest a flatter slope. The AIDA measurements at higher temperatures contributing to their parametrization are conducted close to the detection limit of AIDA. It is possible that the slope is dominated by the most ice-active samples, which might be still detectable in this temperature range. An indication for this possible explanation is also that the individual samples of their study have a steeper slope compared to the parametrization, which is based on four different samples. Contrary to this is the fact that one sample, which was measured in the scope of both investigations (SDGe01, *GS* in Steinke et al. (2016)), shows a higher ice activity in Steinke et al. (2016) than in the present investigation. For 262 K, the difference between the AIDA measurement of Steinke et al. (2016) and the CSU-IS, INSEKT and MINA results from the present study is more than one order of magnitude. A possible explanation for this discrepancy could be that Steinke et al. (2016) used larger particle sizes for measurements at higher temperatures to increase the available surface area. Even if the ice nucleation is normalized by the surface area, the size difference might explain the higher values.

For temperatures above 253 K, the INAS density of the different samples show a highly individual behavior and vary by more than two orders of magnitude. In this temperature range, the ice nucleation activity seems to be strongly dependent on the soil composition and can no longer be described by a log-linear fit. To be able to observe such trends, the new results point out the importance to investigate the entire temperature range. Especially for weather and climate models, it would be of great importance to quantify the origin of the INPs active at temperatures above 253 K in order to predict the INP concentration precisely.

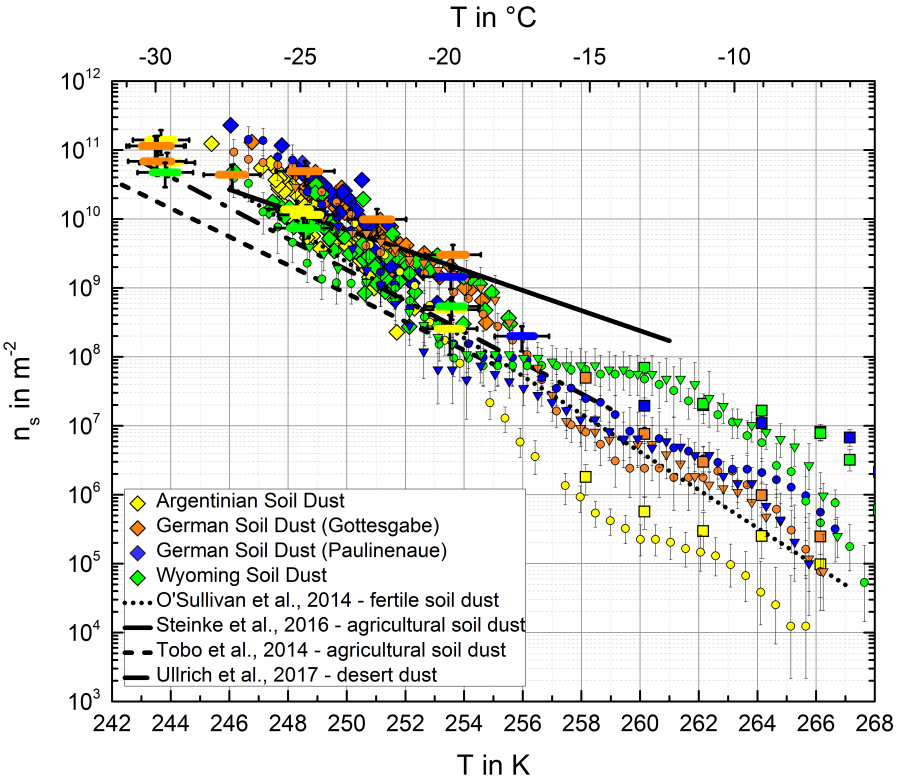

Fig. 4.7.: Temperature-dependent ice nucleation activity of four different arable soil dust aerosols in comparison with literature results (O'Sullivan et al., 2014; Steinke et al., 2016; Tobo et al., 2014; Ullrich et al., 2017). The combination of five different INP measurement methods (AIDA diamonds, CSU-IS circles, INKA bars, INSEKT triangles, MINA squares) allows to cover a wide temperature range. MINA measurements courtesy of Bernhard Pummer and Petya Yordanova (MPIC).

4.4. Cirrus Cloud Regime

To investigate the ice nucleation activity of arable soil dust in the cirrus cloud regime, numerous AIDA cloud expansion experiments at different starting temperatures have been conducted (Tab. 4.4) with two different soil dust samples, the Argentinian soil dust and the German soil dust from Gottesgabe (Sec. 4.2).

4.4.1. Ice Nucleation Activity

The cloud simulation chamber AIDA allows for ice nucleation experiments at upper tropospheric temperatures. Here, the ice nucleation activity is expressed as INAS densities n_s (see Sec. 3.2). Resulting data points with the same n_s values are then examined in the ice saturation ratio-temperature plane. The arable soil dust from Germany (Gottesgabe) shows a u-shaped isoline for INAS densities between $5\times10^{11}\,\mathrm{m}^{-2}$ and $5\times10^{12}\,\mathrm{m}^{-2}$ and temperatures between 190 K and 226 K (Fig. 4.8, blue circles). Ullrich et al. (2017) discussed that the ice nucleation in the deposition nucleation mode is controlled by different

Tab. 4.4.: Overview of the AIDA cloud expansion experiments conducted in the cirrus cloud regime. Name of the campaign, experiment number and start time are listed. The extension _ *ht300* indicates that the bulk sample was dry heated to 673 K, whereas _ *fh300* indicates that the aerosol heating tube was used with an aerosol temperature of 673 K. p_0, T_0 and $c_{n,0}$ are the pressure, temperature and aerosol number concentration at the beginning of the expansion.

Campaign	Experiment No.	Start time	Aerosol Type	p_0 in mbar	T_0 in K	$c_{n,0}$ in cm^{-3}
CIRRUS01	37	07.07.2016 14:11	SDGe01	1007.28	204.68	101
CIRRUS01	39	08.07.2016 09:22	SDGe01	1003.80	223.65	145
CIRRUS01	41	08.07.2016 16:30	SDGe01	1002.08	215.64	146
CIRRUS01	45	11.07.2016 12:55	SDGe01	998.77	194.17	105
CIRRUS01	48	12.07.2016 09:13	SDGe01	1001.08	198.46	95
CIRRUS01	54	14.07.2016 09:14	SDGe01	1004.73	234.57	140
SOIL02	14	07.03.2016 16:10	SDGe01	990.36	228.48	106
SOIL02	15	07.03.2016 21:57	SDGe01_ ht300	993.88	228.69	159
SOIL02	18	08.03.2016 19:09	SDGe01	1004.34	248.05	134
SOIL02	26	14.03.2016 12:38	SDAr08	1015.00	228.36	176
SOIL02	27	14.03.2016 17:45	SDAr08_ ht300	1012.84	228.83	260
SOIL02	29	15.03.2016 16:39	SDAr08	1009.18	248.14	367
SOIL02	39	22.03.2016 17:38	SDAr08_ fh300	997.93	248.16	310

mechanisms, which will here only be summarized. The lower temperature regime (< 220 K) is determined by the classical deposition nucleation theory, which results in decreasing n_s values for increasing temperatures. At higher temperatures, close to the extrapolated liquid water equilibrium line, the increasing ice nucleation activity with increasing temperature might be explained by the pore condensation and freezing mechanism (Marcolli, 2014). The humidity conditions control the transition regime between these two mechanisms. To confirm the u-shaped n_S isolines of the Argentinian soil dust as well, more data points especially at lower temperatures will be necessary (Fig. 4.8, triangles).

Both arable soil dust samples investigated in the scope of this thesis are in very good agreement with previous AIDA measurements of agricultural soil dust (Steinke et al. (2016); Fig. 4.8, green solid line, $5\times10^{10}\,m^{-2} < n_s < 5\times10^{11}\,m^{-2}$). This is not surprising since one of the four soil samples Steinke et al. (2016) used for their parametrization is the identical German soil dust which was also used for the present study. The results from Steinke et al. (2016) cover a smaller temperature range (233 K to 246 K), but they are based on a larger number of dusts samples.

The tendency to u-shaped isolines has also been observed by AIDA cloud simulation experiments with desert dust samples (original work by Ullrich et al. (2017), modified fit parameters by Vogel (2016);

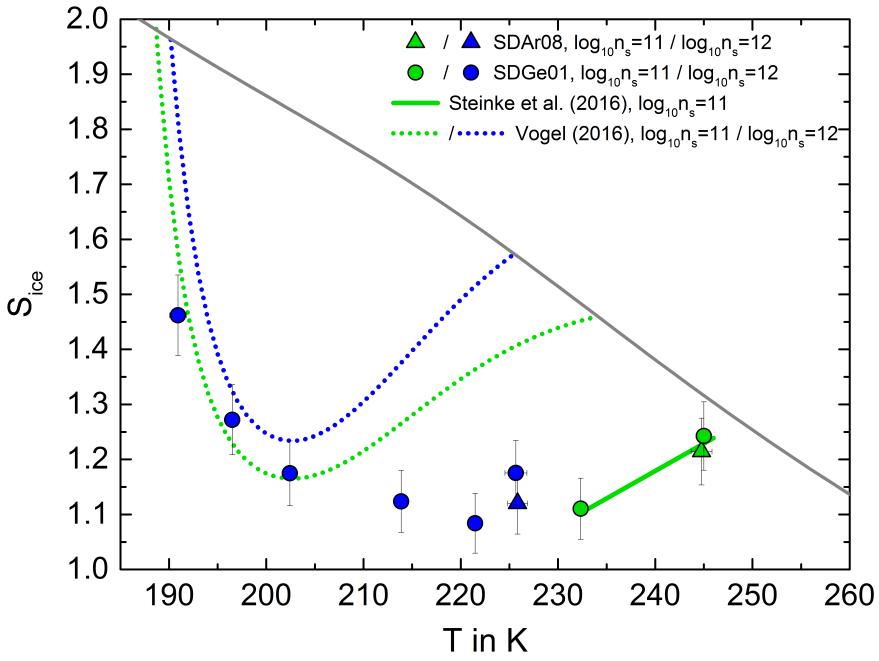

Fig. 4.8.: Temperature- and humidity-dependent ice nucleation activity of two different arable soil dust aerosols, the Argentinian soil dust (triangles) and the German soil dust from Gottesgabe (circles), in comparision with literature data for agricultural soil dust (Steinke et al. (2016), green solid line) and mineral dust (Vogel (2016), dotted lines). The grey solid line indicates liquid water saturation.

Fig 4.8, dotted lines). For temperatures above 210 K, the mineral dust particles seem to require higher ice saturation ratios in order to nucleate ice. But in this temperature range, the mineral dust data scatters so that individual measurements are in the same range of the arable soil dust results. At temperatures below 210 K, the arable and the mineral dust partciles show, within error bars, a similar ice nucleation behavior. But in this temperature range, the present study is based on only one arable soil dust sample, whereas Ullrich et al. (2017) and Vogel (2016) used various desert dust samples for their parametrization. Further investigations with other arable soil dust samples are required to confirm the findings of the present study for temperatures as low as 190 K.

4.4.2. Contribution of Soil Organic Matter

Comparable to the experiments done in the mixed phase cloud regime, 673 K bulk heat-treated samples have been investigated to evaluate the influence of soil organic matter on the ice nucleation ability in the cirrus cloud regime. For this purpose, two identical AIDA expansion experiments with (Fig. 4.9, red symbols) and without (Fig. 4.9, blue symbols) heat treatment on the soil samples provide information on changes in the ice nucleation activity. The starting temperature and pressure of both experiments are thereby comparable (228 K for Fig. 4.9). An identical initial pumping speed ensures that also the pres-

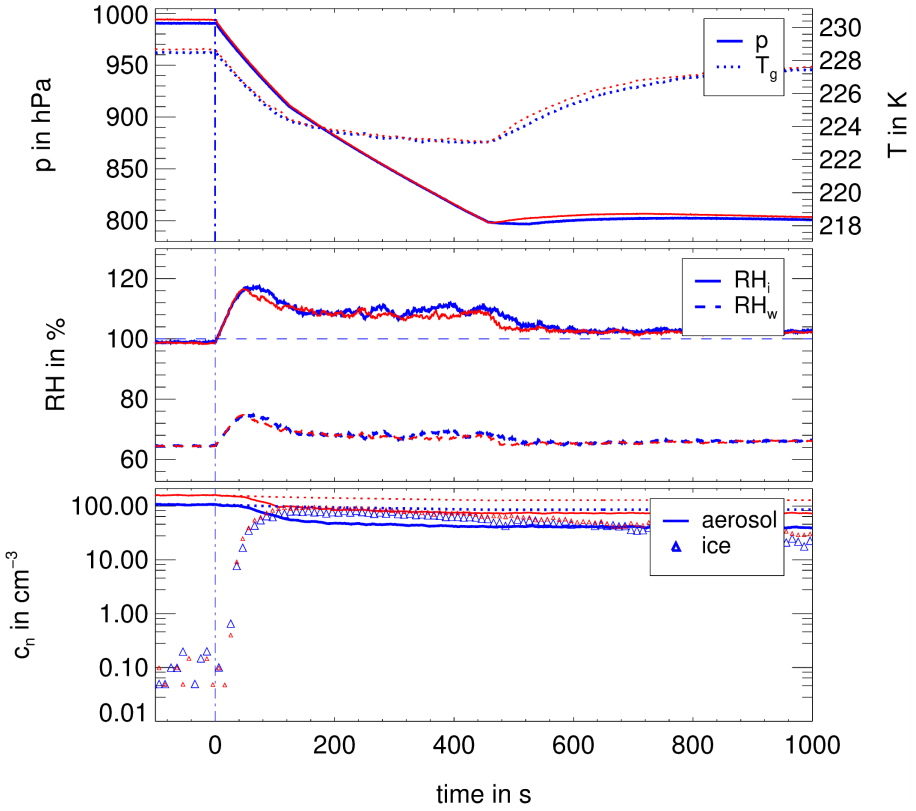

Fig. 4.9.: Data time series of two AIDA experiments in the cirrus cloud regime, both started at 228 K showing the German soil dust from Gottesgabe (SDGe01) with (red symbols) and without (blue symbols) heat treatment. Panel 1 shows the chamber pressure (left vertical axis) as well as the gas temperature (right vertical axis). Panel 2 shows the relative humidity with respect to liquid water and ice, respectively. Panel 3 shows the aerosol number concentration measured with the CPC as well as the total and ice number concentration calculated from the measured single particle data of the OPC. The vertical blue line indicates the start of the expansion experiments.

sure and temperature drop due to the expansion and the related increase in humidity are similar (Fig. 4.9, panel 1 and 2). In contrast to the immersion freezing experiments (compare Fig. 4.4), the bulk heat treatment with 673 K has no measurable effect on the ice nucleation activity of a deposition nucleation experiment started at 228 K (Fig. 4.9, panel 3).

To quantify the influence of the heat treatment methods, the resulting INAS densities need to be examined as a function of temperature and humidity. For the Argentinian soil dust, the deposition nucleation activity at 226 K of the untreated sample is identical to the one of the 673 K bulk heated sample (Fig. 4.10, red, framed triangle). Further, the 673 K heat treatment with the aerosol heating tube does not influence the behavior of the INPs, which are active at 245 K (Fig. 4.10, red, solid triangle). For the German soil dust from Gottesgabe, the 673 K bulk heat treatment also has no effect on the ice nucleation behavior at 226 K (Fig. 4.10, red, framed circle).

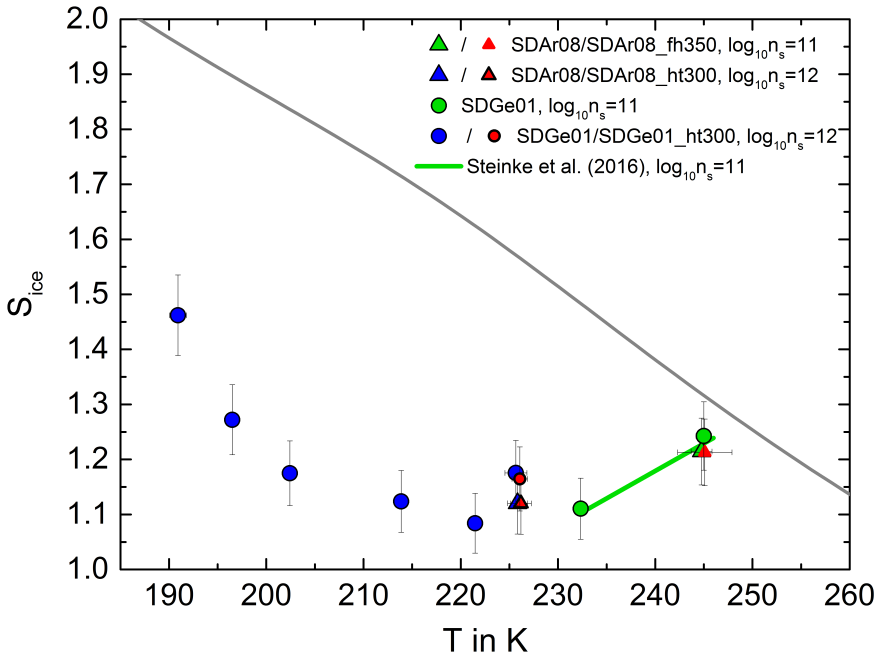

Fig. 4.10.: Influence of organic matter pyrolysis on the ice nucleation activity of the German soil dust from Gottesgabe and the Argentinian soil dust in the cirrus cloud regime. The difference between the untreated aerosol (green and blue symbols) and the bulk heat-treated (red, framed symbols) as well as the aerosol heat-treated (red solid symbol) samples. The grey solid line indicates liquid water saturation.

This shows that the ice nucleation mechanism in the cirrus cloud regime is different compared to the one in the mixed-phase cloud regime. For deposition nucleation, the contribution of soil organic matter to the ice nucleation process seems to be negligible. These findings might confirm the suggestion by Ullrich et al. (2017) that the ice nucleation below water saturation and at relatively high temperatures (here between 226 K and 245 K) might be explained by the pore condensation and freezing mechanism, and is thus controlled by particle microphysics rather than composition.

4.5. Summary

The ice nucleation behavior of arable soil dust was comprehensively investigated in series of laboratory experiments in order to assess their contribution to the ice formation in atmospheric clouds. A central focus was to elucidate the source of the enhanced ice nucleation efficiency of organic-rich arable soil dust originating from more vegetated areas compared to pure mineral dust originate from desert areas. For this purpose, four different arable soil samples from different locations in the world have been investigated both in the mixed-phase cloud immersion freezing regime and the deposition nucleation cirrus cloud regime.

For the mixed-phase cloud regime, the results from five different INP measurement methods have been combined in order to cover a wide temperature range from 243 K to 268 K. In general, the results from all INP methods agree well to each other. At all temperatures, the immersion freezing activity of arable soil dust is markedly enhanced compared to pure mineral dust particles (Ullrich et al., 2017). The temperature dependence of the INAS density is somewhat steeper than the one reported by Steinke et al. (2016) for four agricultural soil dusts. The temperature spectra of INP concentrations or INAS densities show two distinct regimes. In the lower temperature regime, the ice nucleating particles are most likely mineral dust particles and the results from the different samples agree very well with each other. At higher temperatures, the ice nucleation activity varies by up to two orders of magnitudes between the different samples and seems to be strongly dependent on the soil composition. The transition from the one to the other temperature regime is between 253 K and 258 K, depending on the arable soil dust aerosol.

The contribution of soil organic matter to the ice nucleation activity of arable soil dust was investigated by heat treatment of either the bulk material, the aerosol added to the AIDA or APC chamber or the aerosol-water suspensions used for the CSU-IS measurements. The bulk material as well as the dispersed aerosol were heated to 673 K, where the soil organic matter gets pyrolyzed. The aerosol suspensions used for the CSU-IS measurements were heated to only 368 K where most soil organic matter is not affected but proteinaceous INPs are denaturized. Both treatment methods to 673 K markedly reduced the overall INAS density at all temperatures, the bulk heat treatment by about two orders of magnitude and the aerosol heat treatment by about one order of magnitude. The 368 K aerosol suspension heating reduced the ice nucleation activity only at temperatures above 254 K or 260 K, depending on the sample, thereby indicating that at these temperatures the ice nucleation activity of the arable soil dust aerosols is controlled by heat-sensitive INPs, which are possibly proteins or other macromolecules.

In the cirrus cloud temperature regime, two different arable soil dust aerosols were investigated. Here, the ice formation occurs far below water saturation and depends on both the temperature and the relative humidity with respect to ice. A series of deposition nucleation experiments with one soil dust sample between 190 K and 245 K showed u-shaped isolines of the INAS density parameter in the temperature-saturation ratio diagram, similar to recent literature results for pure mineral dust aerosols (Ullrich et al., 2017). The here investigated soil dust is more ice active at low ice supersaturations than pure mineral dust aerosols investigated in previous AIDA studies. At lower temperatures, the INAS density isoline rises with decreasing temperatures, which can be explained by classical nucleation theory. The increasing INAS density isolines with increasing temperatures above about 220 K may be due to the occurrence of the pore condensation and freezing mechanism (Marcolli, 2014) at these higher temperatures. In the transition regime, the ice nucleation activity is almost independent of the temperature (horizontal INAS density isolines in the RH_i-T-diagram) and only depends on the relative humidity.

For the two samples investigated in the cirrus temperature regime, neither the bulk nor the aerosol heat treatment to 673 K affected the ice nucleation behavior. This leads to the conclusion that soil organic matter has a minor contribution to the ice nucleation of arable soil dust aerosol in cirrus clouds.

5. Atmospheric Ice Nucleating Particle Concentrations Measured During Dust Events in the Mediterranean

5.1. Introduction

Since many years, mineral dust is in the focus of atmospheric science. It is a globally prevalent aerosol species, which has not only an impact on weather but also directly and indirectly on the climate.

Mineral dust is the most abundant aerosol species on the global scale with emissions of hundreds to thousands $\mathrm{Mt\,year^{-1}}$ (Huneeus et al., 2011). Strong surface winds over arid and semi-arid regions loft soil dust into the atmosphere (Prospero et al., 2002). The most important aerosol production mechanism is called sandblasting. Here saltating soil dust particles either separate, when they are agglomerates, or mobilize surrounding surface particles (Shao et al., 2011). Both cases result in an emittion of fine dust particles. Large desert areas in Northern Africa, the Middle East, Central and South Asia as well as China are known as major sources of atmospheric dust particles (Fig. 5.1), whereas the Sahara with the Bodélé Depression is the world's largest source (Prospero et al., 2002; Koren et al., 2006) contributing up to 50 % to the total dust load (Engelstaedter et al., 2006). But there is also dust emission at high latitudes, e.g. in Greenland (Bullard and Austin, 2011) or Iceland (Arnalds et al., 2016). Those dust sources are often associated with fine particles lofted by strong winds into the atmosphere from glaciers. Those dust emissions are very seasonal and the contribution to the global aerosol mass is rather low. Fine mineral dust aerosol particles (with diameters of a few µm or less) emitted from North Africa can be lifted by atmospheric motion to great heights and are then transported over long distances not only to the Mediterranean and to Central Europe but also via horizontal trade winds over the Atlantic Ocean to the Caribbean forming the Saharan Air Layer (Weinzierl et al., 2017; Knippertz, 2017). On its transatlantic transport, the dust particles undergo physical and chemical aging, such as agglomeration, weathering and oxidation. Removal of mineral dust aerosol particles occurs either by dry deposition caused by settling, molecular or turbulent diffusion, or by wet deposition via scavenging through clouds or precipitation. Recent model results suggested dust aerosol lifetimes of up to 15 days for submicrometer dust particles (Kok et al., 2017). The lifetime is longer than previously estimated and strongly decreases with increasing particle size.

Mineral dust aerosol has a direct radiative effect on the global climate. It interacts with the incoming short-wave solar radiation and the outgoing long-wave terrestrial radiation. Small dust particles preferably scatter the solar radiation, which results in a cooling effect. Larger particles on the other hand absorb terrestrial radiation and thereby are expected to have a heating effect (Mahowald et al., 2014). The total

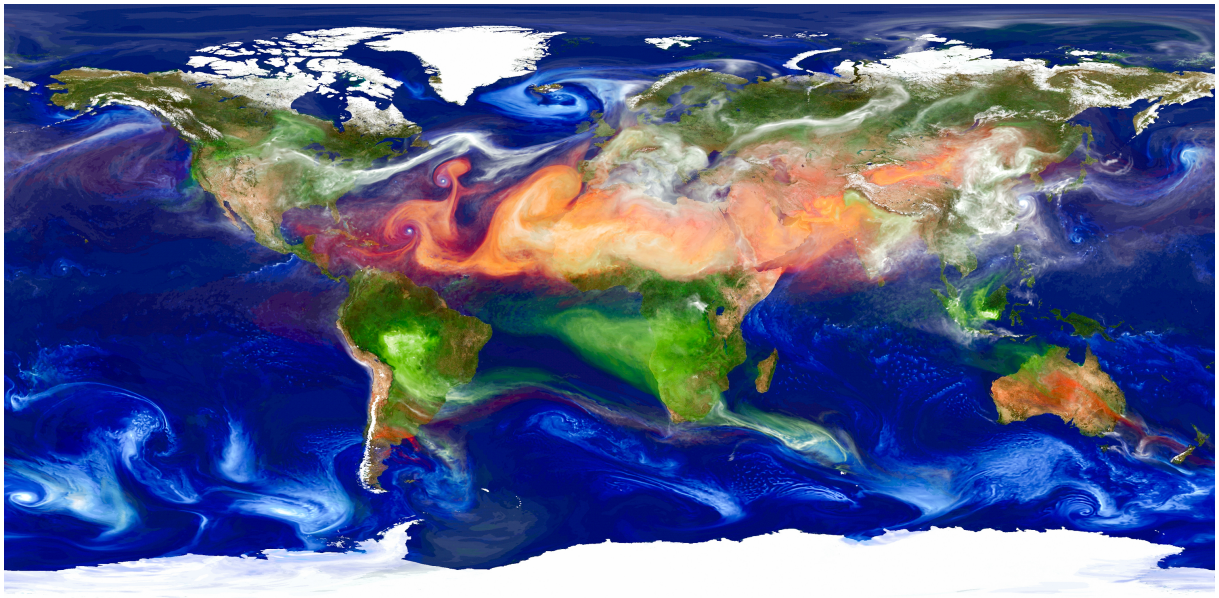

Fig. 5.1.: The global distribution of mineral dust aerosol particles. GEOS-5 (Goddard Earth Observing System Model, Version 5) simulations showing the four most important atmospheric aerosol species: minerals dust from deserts (red), sea salt from sea spray (blue), smoke from fires (green) and sulfate particles from volcanoes and fossil fuel combustion (white). From NASA/Goddard (2016).

impact of dust particles strongly depends on the particle size distribution and on its abundance (Tegen and Lacis, 1996; Mahowald et al., 2014) as well as on the particle shape, the mineralogy and the mixing state (Sokolik and Toon, 1999; Kandler et al., 2009), all of which influence their optical properties. The total direct impact of dust aerosol on the radiation, whether the heating or the cooling effect of atmospheric dust particles is dominating, is still not well understood and contains large uncertainties (Stocker et al., 2013).

Mineral dust aerosol also has an aerosol-cloud indirect effect on the climate. Numerous laboratory investigations have already shown that mineral dust is an efficient ice nucleating particle in the immersion freezing and deposition nucleation regime (Koehler et al., 2010; Broadley et al., 2012; Niemand et al., 2012; Augustin-Bauditz et al., 2014; Ullrich et al., 2017), whereby especially K-feldspar seems to have an enhanced ice nucleation activity (Atkinson et al., 2013; Peckhaus et al., 2016). This has also been observed in field observations (DeMott et al., 2003b; Ardon-Dryer and Levin, 2014; Boose et al., 2016b). Measurements of atmospheric ice particle residuals (IPRs) also suggested a preference for ice particles to form on dust particles (Kamphus et al., 2010; Cziczo et al., 2013). Further, space observations suggest that dust particles might be important for cloud glaciation due to an observed negative correlation between its concentration and the supercooled water fraction (Choi et al., 2010). Due to its ice nucleation efficiency in combination with its abundance, mineral dust aerosol is assumed to be one of the most important INP types on the global scale (Hoose et al., 2010). Aging by coating with sulfate and other soluble materials (Levin et al., 1996) during its transportation in the atmosphere makes it unlikely

to find pure mineral dust particles in the atmosphere, at least when they have already a residence time of more than a few hours in the atmosphere. These coatings might influence the ice nucleation activity of dust particles (Möhler et al., 2006; Boose et al., 2016c). To refine the formulation of heterogeneous ice nucleation in weather and climate models, an extended data set on atmospheric INP properties is required.

For the monitoring of atmospheric soil dust dominated INP concentrations during the four-week INUIT-BACCHUS-ACTRIS campaign in April 2016, the location of the Cyprus Atmospheric Observatory (CAO) (Sec. 3.1.2) has been chosen, since this field site is frequently influenced by dust from the Sahara and the Middle East. Aerosol particles were collected on 0.2 µm pore diameter filters for immersion freezing analysis with the Ice Spectrometer of the Colorado State University (CSU-IS). Atmospheric INP concentrations measured during time periods with high dust levels in the Mediterranean will be presented (Sec. 5.2), including the discussion on the contribution of soil organic matter to the ice nucleation activity, the comparison with predictions from laboratory based parametrizations and the comparison with INP measurements conducted at other locations. In the last part of this chapter, the findings will be summarized (Sec. 5.3).

5.2. Measurements at the Cyprus Atmospheric Observatory (CAO)

Atmospheric aerosol particles have been collected at the CAO during the four-week INUIT-BACCHUS-ACTRIS campaign in April 2016 for offline immersion freezing experiments.

The meteorological conditions during the campaign has already been described in Schrod et al. (2017) and is only summarized here. During the entire campaign, Cyprus was mainly influenced by a westerly flow. The local wind direction at the station was also typically westerly with wind speeds usually below $6\,\mathrm{m\,s^{-1}}$ (Fig. 5.2). The first week (01/04/16 to 08/04/16) was dominated by warm, anticyclonic conditions, which resulted in a daily increasing maximum temperature of up to 303 K and a decreasing relative humidity down to 20 % at the station. Afterwards, an approaching low-pressure system changed the weather situation. The relative humidity strongly increased to values around of 70 %, whereas the maximum temperature dropped below 293 K combined with rain (12/04/16). This rather cold and humid days were followed by anticyclonic conditions with an again increasing temperature and decreasing relative humidity (14/04/16 to 20/04/16). In the last days of the campaign (21/04/16 to 27/04/16), the station was influenced by a cyclonic pattern bringing again a decrease in temperature and an increased humidity but no rain.

Backward trajectories from the HYSPLIT model (Hybrid Single Particle Lagrangian Integrated Trajectory model, Stein et al. (2015); Rolph et al. (2017)) indicate that Cyprus was episodically influenced by mineral dust particles from the Sahara or surrounding areas during the time of the campaign.

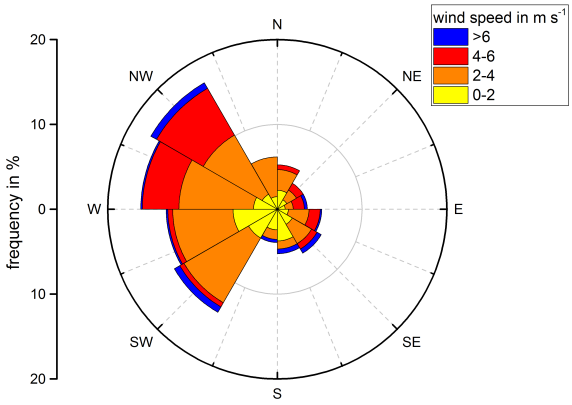

Fig. 5.2.: Relative frequency of wind speed and wind direction measured at CAO for the entire time period of the Cyprus 2016 campaign, starting with the first CSU-IS sample at 04/04/16 11:57 LT to the end of the last sample at 26/04/16 17:33 LT. Hourly averages of wind speed and direction courtesy of the Department of Labour Inspection (DLI).

5.2.1. Atmospheric Ice Nucleating Particle Concentrations

In order to investigate the ice nucleation activity of soil dust dominated atmospheric aerosol particles, 18 ambient filters have been analyzed with the immersion freezing method CSU-IS (see Sec. 3.1.2 and Sec. 3.4.3). The filters were collected during daytime covering the time period from 04/04/16 to 26/04/16 (Tab. 5.1), whereby each sample provides information about the atmospheric INP concentration from ice nucleation onset (usually around 263 K) to temperatures as low as 246 K. Due to the sampling time of several hours per day, the measured INP temperature spectra represent an averaged ice nucleation activity for the respective period. As a consequence, the time resolution is rather low, but the instrument is able to cover the entire temperature range important for immersion freezing, including the low INP concentrations at higher temperatures.

For reasons of clarity, the time series of single ice nucleation temperatures will be discussed rather than the whole INP temperature spectrum (Fig. 5.3). For this purpose, two temperatures have been chosen: 251 K and 261 K.

During the course of the campaign, the mean INP concentration at 251 K was 2.71^{-1} (Fig. 5.3, left axis, red diamonds show daily averaged concentrations). Most of the time, the measured values were very close to the mean value, only two days (09/04/16 and 12/04/16) show a significant deviation. The laboratory measurements shown in this thesis already suggested that the ice nucleation activity at temperatures below 253 K is dominated by mineral dust particles. Even after transportation in the atmosphere, mineral dust particles still have sizes of several micrometers (Prospero, 1999) and are therefore larger than other aerosol particles. This was also observed in an increase of the number concentration of large aerosol particles during high dust level loads (Schwikowski et al., 1995). Since the aerosol mass is con-

Tab. 5.1.: Overview of the analyzed samples from the INUIT-BACCHUS-ACTRIS campaign in Cyprus in April 2016 with the sampling date, the start time t_{start} and the stop time t_{stop} in local time (LT). $T_{ambient}$ and $p_{ambient}$ are the mean ambient temperature and pressure during the sampling time. V_{air} is the volume of sampled air. For all measurements, the sample flow was 16.71min^{-1}. The indicated samples were treated with 95 °C heat and H_2O_2, respectively.

date	t_{start}	t_{stop}	$T_{ambient}$ in °C	$p_{ambient}$ in mbar	V_{air} in l	95 °C treatment	H_2O_2 treatment
04/04/16	11:57	19:32	23.8	950.4	7599		
05/04/16	10:36	18:26	25.3	947.6	7849		
07/04/16	09:34	18:05	25.5	952.1	8534	x	x
08/04/16	09:49	17:29	26.7	951.3	7682		
09/04/16	10:06	17:38	28.1	945.6	7548	x	x
10/04/16	09:51	17:33	20.8	947.6	7715		
11/04/16	11:28	18:56	19.8	946.6	7482		
12/04/16	10:23	18:27	16.1	945.3	8083		
13/04/16	11:03	18:34	18.4	947.5	7532	x	x
15/04/16	09:23	17:21	24.8	953.9	7983		
16/04/16	09:20	18:10	24.4	956.7	8851		
17/04/16	09:23	16:45	25.7	956.6	7381		
18/04/16	11:08	18:47	26.2	955.7	7665		
19/04/16	11:08	17:07	29.4	954.5	5995	x	x
20/04/16	09:30	17:35	29.2	954.0	8100		
22/04/16	10:06	18:12	24.5	953.8	8116		
24/04/16	10:08	17:35	24.6	945.9	7465		
26/04/16	09:39	17:33	25.7	944.7	7916		

trolled by large particles, the aerosol particle mass concentration, in particular from the coarse mode, is a good indicator for the presence of mineral dust particles. Comparing the coarse-particle mode aerosol (Fig. 5.3, right axis, orange dots; PM10-PM2.5) with the INP concentration at 251 K, both measured at the CAO, show that there is a correlation between these two values over the entire time period of the campaign. A relative increase in the coarse particles is associated with a relative increase in the INP concentration and vice versa. There is one outlier, 19/04/16, where the INP concentration is not following the relative change in the aerosol mass concentration. On this day, the ice nucleation activity at higher temperatures was very high. So, a possible explanation might be that the ice nucleation activity at 251 K was not only caused by mineral dust particles but was rather superimposed by another INP species. Also, the removal of large particles by the single rain event during the campaign (12/04/16, Fig. 5.3, right

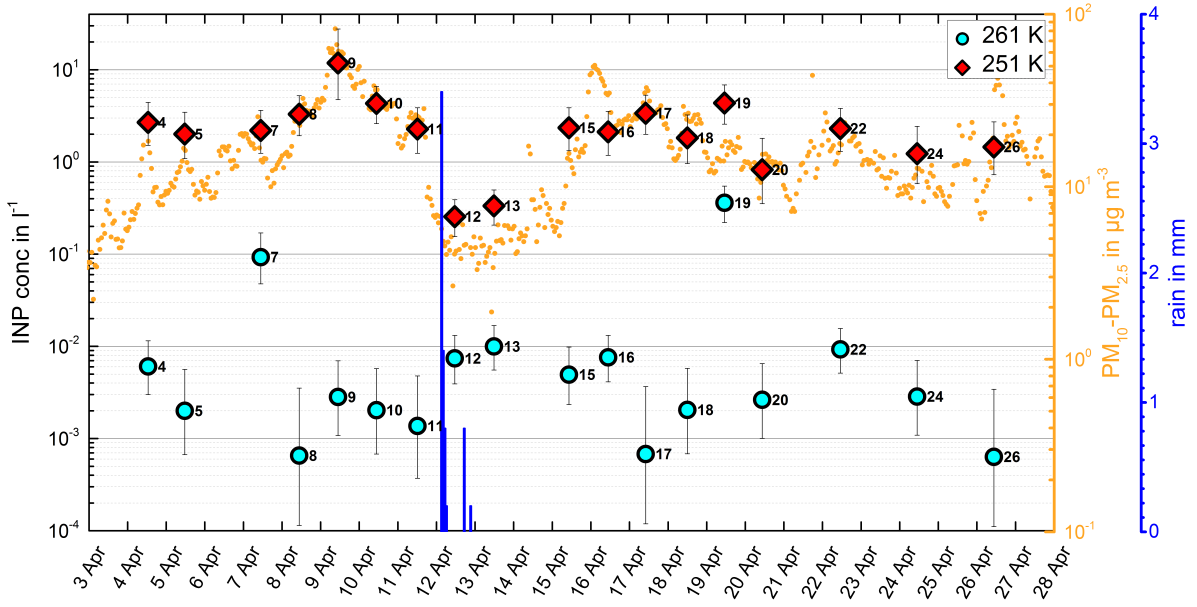

Fig. 5.3.: Data time series of the INP concentration during the Cyprus 2016 campaign for 261 K (left axis, cyan circles) and 251 K (left axis, red diamonds) at the CAO. The numbers close to the symbols indicate the day of the month. In addition, the measured PM_{10}-$PM_{2.5}$ aerosol mass concentration (right axis, orange dots) and the amount of rain is shown (right axis, blue bars), both courtesy of the Department of Labour Inspection (DLI).

axis, blue bars), is directly reflected in the measured 251 K INP concentrations. These are significantly lowered compared to other days of the campaign, but still correlate with the coarse mode measurement.

There was a pronounced dust day on the 09/04/16. The coarse-particle mass concentration reached its maximum value of 80 µg m^{-3} and also the INP concentration rose to its maximum value of 12 l^{-1}. In addition, on the 12/04/16, there was a clean day after the rain, where the INP concentration reached its minimum with a value of 2.6×10^{-1} l^{-1}. The aerosol mass concentration dropped to 4 µg m^{-3}. Both, the high dust load as well as the clean conditions were clearly visible in the atmosphere (Fig. 5.4, pictures on the right-hand side). The comparison of the total INP temperature spectra of these two days with the spectra of all other days shows that for temperatures below 253 K the dust day and the clean day show a significantly increased or decreased ice nucleation activity (Fig. 5.4). For temperatures higher than 253 K, the ice nucleation behaves different. Here, the dust day has not the highest values compared to the other days of the campaign. In this temperature regime, the clean day shows even higher INP concentrations than the dust day. This leads to the conclusion that here not mineral dust particles but other INP species are dominating the ice nucleation activity.

During the campaign, the mean INP concentration at 261 K was 2.9×10^{-2} l^{-1} (Fig. 5.3, left axis, cyan circles). On the 26/04/16 the INP concentration had its minimum with a value of 6.3×10^{-4} l^{-1}, whereas the maximum value of 3.6×10^{-1} l^{-1} was reached on the 19/04/16. The time series of the 261 K INP concentration is not correlated to the coarse mode aerosol. For some days, a relative decrease in the

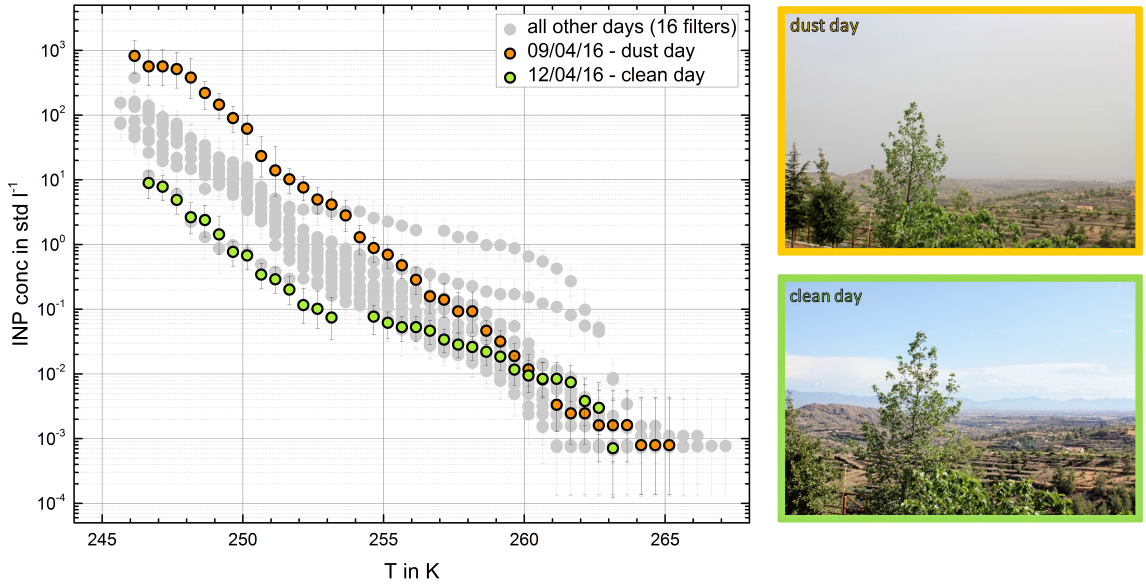

Fig. 5.4.: INP temperature spectra of the dust (orange) and clean (green) day during the Cyprus 2016 campaign in intercomparison with all other samples (grey). The right-hand side shows the view from the CAO on both of these days. Pictures courtesy of Rebecca Kohl.

coarse particles is even associated with a relative increase in the INP concentration. In contrast to the observation at 251 K, here the INP activity is increased for the samples collected after the rain. The mechanical impact of rainfall is thought to release INPs from the vegetation, which can be observed in a temporary increase of the INP concentration (Huffman et al., 2013; Prenni et al., 2013). Since the filter was collected well after the rain, it is more likely that the increase is triggered by other influences rather than by the rain. Especially the strong day-to-day changes in the 261 K INP concentration might lead to the conclusion that the ice nucleation activity at higher temperatures is triggered by local parameters. For instance, on the days before the 07/04/16 there was a high pollen count, which might have caused the significant increase in INP concentration. Pollen themselves are too big to pass the sampling inlet. Since pollen washing water is very ice active (Augustin et al., 2013), even fragments of pollen in the sample could immensely increase the ice nucleation activity. The possibly local impact makes it rather difficult to predict the INP concentration at temperatures as high as 261 K. Further investigations of the meteorological data and local parameters like the pollen count could provide more information.

5.2.2. Contribution of Soil Organic Matter

For selected samples, the contribution of soil organic matter to the ice nucleation activity has been investigated. For this purpose, measurements of the untreated sample are compared with measurements, where a sample treatment method has been applied prior to the analysis. Thereby, 368 K heating (see Sec. 3.1.3 for details) denatures heat-sensitive INPs, while H_2O_2 digestion decomposes organic INPs (see Sec. 3.1.4 for details). For this treatment methods, especially samples with a prominent ice nucleation

behavior at temperatures above 253 K have been selected, because those are most likely triggered by heat-sensitive or organic-containing INPs. The samples from 07/04/16 and 19/04/16 show both a medium INP concentration at temperatures below 253 K, but have a significant increased INP concentration at higher temperatures (Fig. 5.3, left axis, cyan circles; Fig. 5.5, yellow and orange circles, respectively). Further,

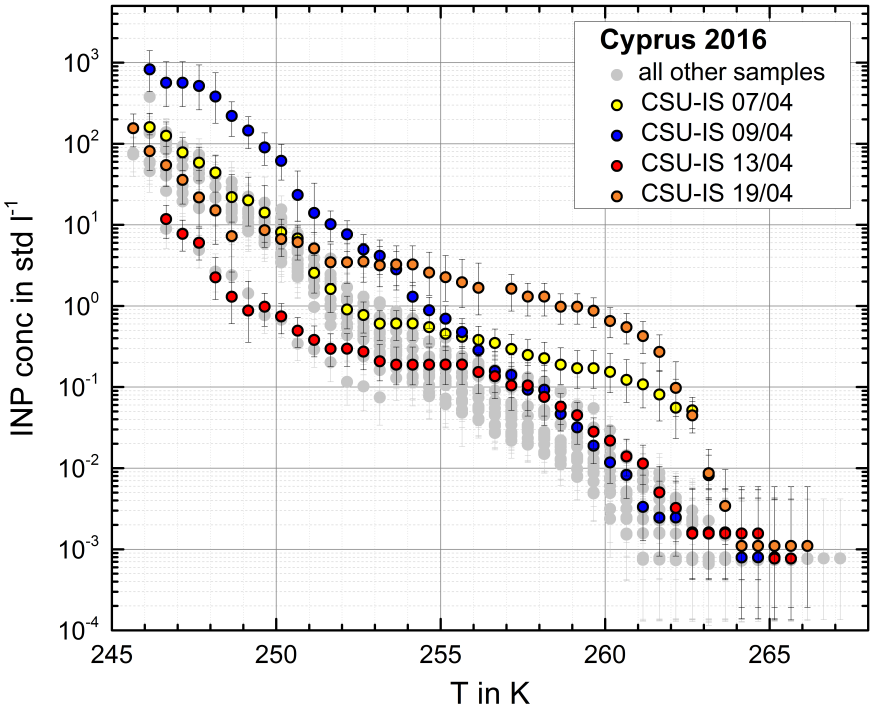

Fig. 5.5.: INP temperature spectra of samples selected for further treatment methods.

sample 13/04/16 was selected as well, because it has very low INP concentrations at lower temperatures while the ice nucleation activity at temperatures above 253 K is very pronounced (Fig. 5.5, red circles). In addition, the dust day sample from the 09/04/16 is selected to investigate the influence of the treatments on mineral dust particles. This rather different sample shows a significantly enhanced ice nucleation activity at lower temperatures, but no significant INP activity at higher temperatures (Fig. 5.5, blue circles).

The 368 K heat treatment decreases the INP concentration of sample 07/04/16 at temperatures above 253 K (Fig. 5.6a). The H_2O_2 digestion seems to cause an additional, slight reduction in the same temperature range. For temperatures below 253 K both treatment methods seem to have, within measurement uncertainties, no effect on the sample. The ice nucleation activity of sample 09/04/16 behaves independent of both treatment methods (Fig. 5.6b). For sample 13/04/16, the heat treatment slightly lowers the INP concentration at high freezing temperatures (Fig. 5.6c). Due to irregularities during sample preparation, the data for the H_2O_2 digested sample is shifted towards colder temperatures. One would not expect the treatment to have such a prominent influence at temperatures below 253 K. Keeping this shift in mind, this sample contains less heat-sensitive and more organic-rich INPs compared to sample 07/04/16. In-

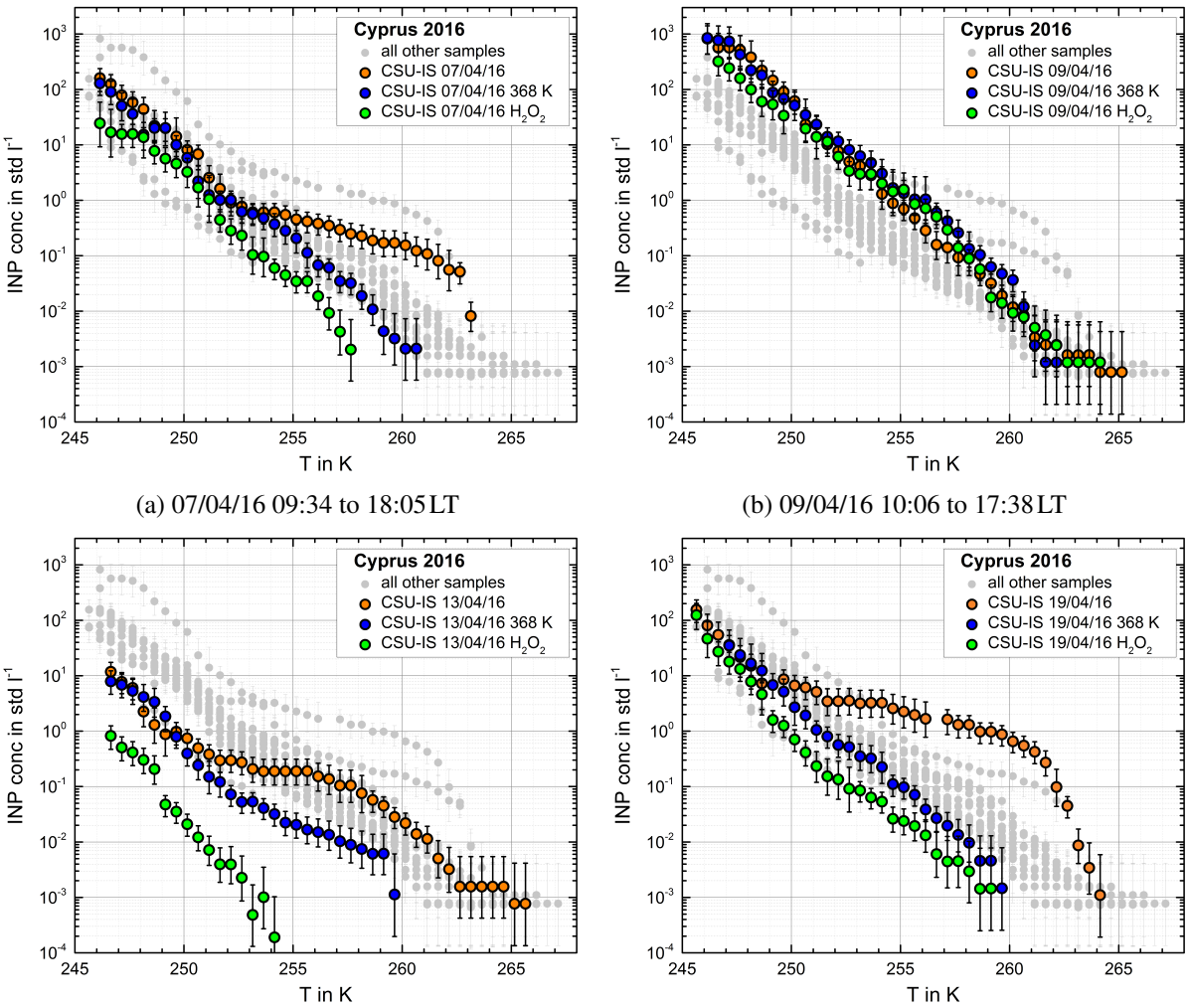

(a) 07/04/16 09:34 to 18:05 LT

(b) 09/04/16 10:06 to 17:38 LT

(c) 13/04/16 11:03 to 18:34 LT

(d) 19/04/16 11:08 to 17:07 LT

Fig. 5.6.: Contribution of heat-sensitive and organic-rich INPs to the atmospheric INP concentration measured at the CAO for four selected CSU-IS samples of the Cyprus 2016 campaign. Influence of 95 °C heat treatment (blue circles) and H_2O_2 treatment (green circles) on the ice nucleation activity of the sampled aerosol particles (orange circles).

terestingly, the temperature, where the treatments seem to have no effect on the INP concentration, is lower for this sample. Sample 19/04/16 contains a great number of heat-sensitive INPs (Fig. 5.6d). The moderate heat treatment with 368 K reduces the ice nucleation activity already over a wide temperature range. The additional H_2O_2 treatment does not have a further significant influence. Again, the threshold where the mineral particles seem to dominate the ice nucleation activity, is below 253 K and rather close to 249 K.

The local wind speed and the wind direction were measured at the CAO. The relative frequency of these values during the particle collection time of the CSU-IS samples might provide information on the sources of INPs (Fig. 5.7). For sample 07/04/16 the wind was blowing from north and northwest directions with wind speeds between $2\,m\,s^{-1}$ and $6\,m\,s^{-1}$ (Fig. 5.7a). On the 09/04/16, the wind speed was above $6\,m\,s^{-1}$ mainly blowing from south and southwest (Fig. 5.7b). During sample 13/04/16, the CAO was influenced by northerly wind with wind speeds between $2\,m\,s^{-1}$ and $6\,m\,s^{-1}$ (Fig. 5.7c). On the 19/04/16, the wind was blowing from east and northeast with a wind speed between $4\,m\,s^{-1}$ and $6\,m\,s^{-1}$ (Fig. 5.7d). So during the sampling time of the samples 07/04/16, 13/04/16 and 19/04/16 the CAO was mainly influenced by northerly wind with common wind speeds between $2\,m\,s^{-1}$ and $6\,m\,s^{-1}$, whereas the wind conditions on the 09/04/16 show a different pattern. Here, the station was influenced by southerly wind and the wind speed was relatively high for local conditions with values above $6\,m\,s^{-1}$.

For further investigations on the INP source, backward trajectories with the HYSPLIT model have been calculated (Stein et al., 2015; Rolph et al., 2017)). These trajectories provide information on the air masses reaching the measurement station at the time of particle collection (Fig. 5.8). On the 07/04/16, the air masses were mainly coming from the Sea and were reaching Cyprus from northwest (Fig. 5.8a). Only the backward trajectory for 0 m a.g.l and 1500 m a.g.l shortly crossed Southern Turkey before arriving at the CAO. The backward trajectories in 1500 m a.g.l and 3000 m a.g.l of the 09/04/16 were coming from Northern Africa, crossing Mali, Niger, Libya and Egypt before the air mass is reaching Cyprus from southwest (Fig. 5.8b). This means that air was transported from both the Sahel and the Sahara Desert. The air mass arriving at the CAO (0 m a.g.l) originated from the Sea and was entering Cyprus from southeast. The backward trajectories from the 13/04/16 first crossed the Western Mediterranean Sea (Fig. 5.8c). After surrounding Cyprus in the south, they made a bow over Syria and Southern Turkey during the last hours, before they entered Cyprus from the north. On the 19/04/16, the air masses arriving at all heights experienced a long residence time over the land (Fig. 5.8d). After crossing Morocco, Southern Europe and Turkey, the trajectories entered Cyprus from northeast.

The combination of the different INP treatments, the local wind conditions and the origin of the air masses might provide indications on the INP source. The treatment methods have no effect on the ice nucleation activity of sample 09/04/16. This leads to the conclusion that the ice nucleation of the entire

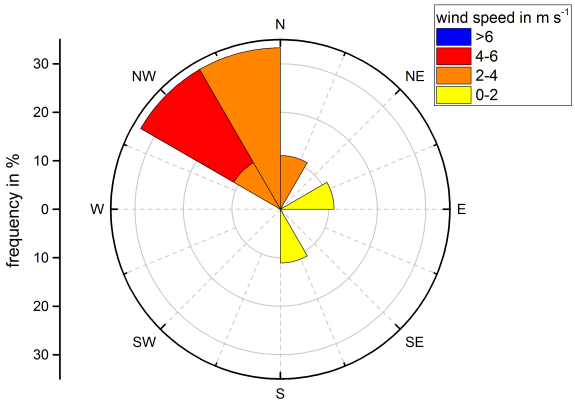

(a) 07/04/16 09:34 to 18:05 LT

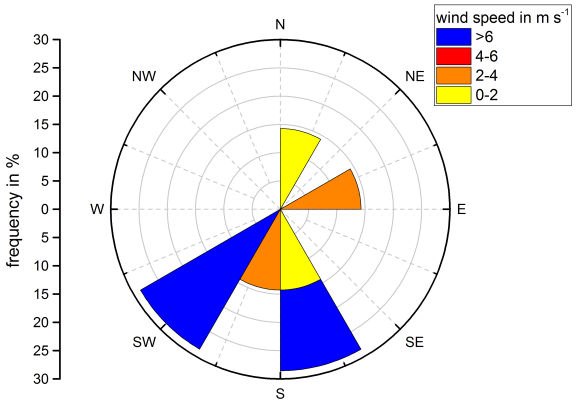

(b) 09/04/16 10:06 to 17:38 LT

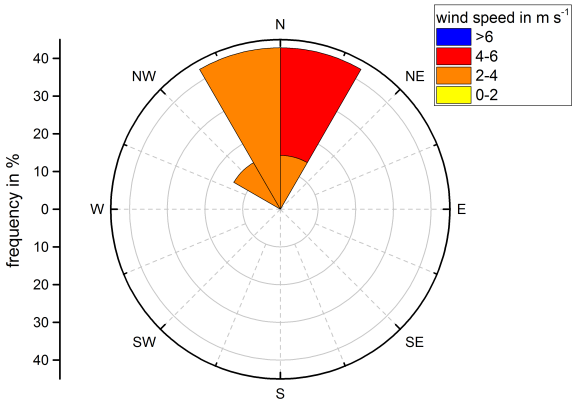

(c) 13/04/16 11:03 to 18:34 LT

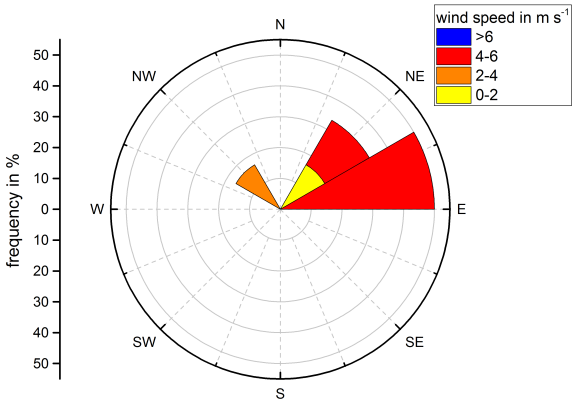

(d) 19/04/16 11:08 to 17:07 LT

Fig. 5.7.: Relative frequency of wind speed and wind direction measured at the CAO for four selected CSU-IS samples of the Cyprus 2016 campaign. Times are in local time. Hourly averages of wind speed and direction courtesy of the Department of Labour Inspection (DLI).

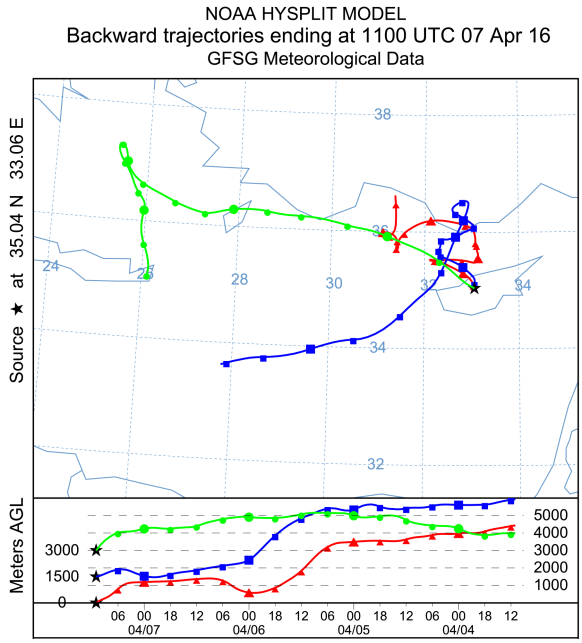

(a) 07/04/16 11:00 UTC

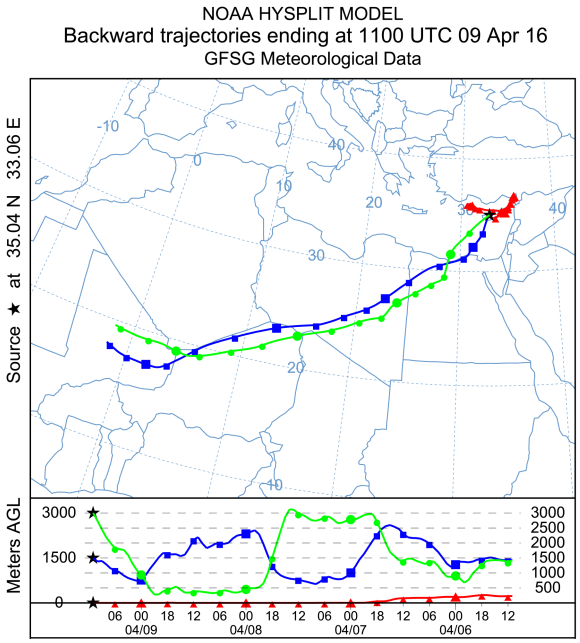

(b) 09/04/16 11:00 UTC

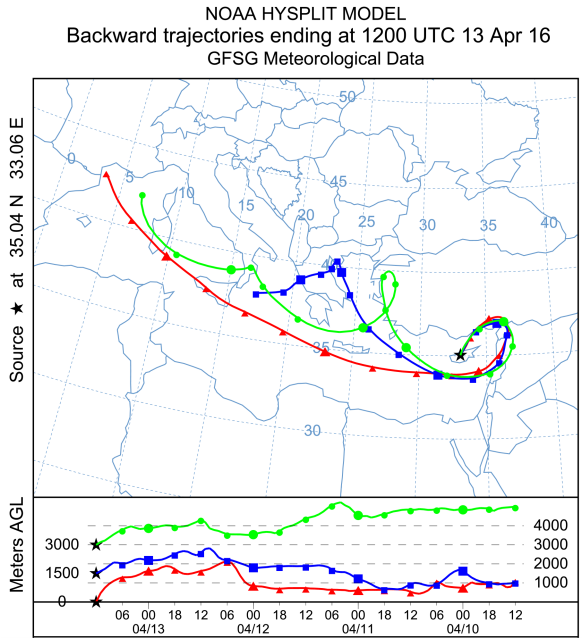

(c) 13/04/16 12:00 UTC

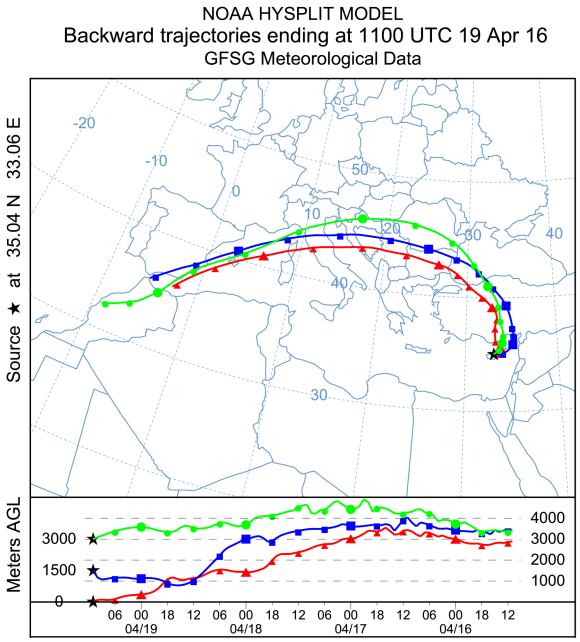

(d) 19/04/16 11:00 UTC

Fig. 5.8.: Backward trajectories for four selected CSU-IS samples of the Cyprus 2016 campaign calculated with the HYSPLIT model (96 h duration, GDAS 0.5 °; Stein et al. (2015); Rolph et al. (2017)).

temperature range is dominated by the influence of mineral dust particles. Further, the air mass reaching the station in 1500 m a.g.l and 3000 m a.g.l had a very long residence time over the Sahara. In combination with the increased local wind speed from southerly directions, it is very likely that the measurement station was influenced by mineral-dust-rich air, which confirms the findings of the treatment methods. The other three samples, 07/04/16, 13/04/16 and 19/04/16, show a different behavior. Here, the samples are more or less pronounced sensitive to the treatment methods for temperatures above 253 K, which means that this temperature range is influenced by heat-sensitive and organic-rich INPs. Below 253 K, the INPs seem to be resistant to the treatment so here the ice nucleation is most likely dominated by mineral dust particles. The air masses of these three samples are transported over the Sea or the continent and cross Southern Turkey before reaching the station from northerly directions, which is consistent with the local wind direction. The heat-sensitive and organic-rich INPs could then be either transported by the air mass, or they could be raised by local winds from surrounding INP sources. The CAO is located north of the Troodos mountains. Southerly wind could transport soil dust dominated aerosol particles from the rural valley, which usually contain both heat-sensitive as well as organic-rich INPs. To confirm this theory further characterizations of the aerosol and the ice particle residuals are necessary (see Sec. 5.3). For the enhanced ice nucleation activity at temperatures above 253 K, it is rather difficult to quantify the INP origin at this point.

5.2.3. Comparison with Predicted INP Concentrations

An important feature of field measurements is that they enable to test laboratory obtained parametrizations on their validity to predict atmospheric INP concentrations.

In the laboratory, many natural soil dust samples were investigated with the cloud simulation chamber AIDA in order to formulate a temperature-dependent parametrization of the INAS density (Ullrich et al., 2017) (Fig. 5.9). Aerosol size distributions (OPS measurements) from the CAO measuring site enable to determine the total aerosol surface during the sampling time of the CSU-IS aerosol particle filter. For the dust day (09/04/16), this value allows to calculate the predicted INP concentration from the AIDA mineral dust parametrization.

Comparing the measured atmospheric INP concentration of the CSU-IS with the predicted INP concentration shows a good agreement for temperatures lower than 248 K (Fig. 5.10). However, the slope of the predicted INP concentration seems to be flatter compared to the measurements.

Possible reasons for the different temperature dependence are that the total aerosol surface concentration is used for all temperatures rather than a decreasing concentration reduced by the amount of already at higher temperature frozen particles. This correction would steepen the temperature dependence of the predicted INP concentration and would therefore bring its slope closer to the one of the measured INP concentrations. However, it would increase the gap between the total INP concentration values. Another reason could be that the aerosol size distribution measured in the field does not solely contain mineral dust particles even when the dust day is chosen. This would then again bring the slopes closer together

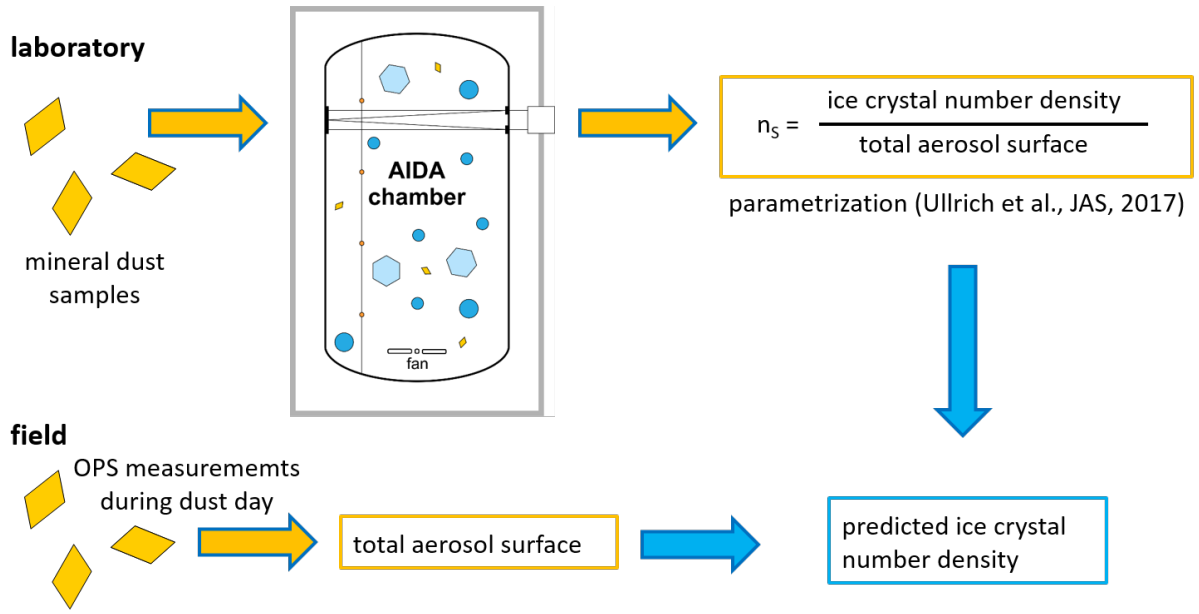

Fig. 5.9.: Schematic of the INP closure study. Laboratory obtained parametrizations in combination with aerosol measurements in the field are used to calculate the predicted INP concentration.

but would increase the deviation of the total values. The differences in the intercomparison could also be caused by measurement artifacts of either the aerosol size distribution or the INP concentration on site. Further, the aerosol surface concentration is only based on one aerosol measurement. Other available aerosol characterization measurements need to be considered as well.

5.2.4. Comparison with Measurements at other Locations

The following Section will focus on the comparison of the INP temperature spectra from the INUIT-BACCHUS-ACTRIS campaign during April 2016 conducted at the Cyprus Atmospheric Observatory (CAO) with atmospheric INP measurements from other locations and other seasons: The temporary measurement station at the airport Paphos during the A-LIFE campaign in April 2017 (Dietel, 2017) and the Storm Peak Laboratory (SPL) during the FIN-3 campaign in September 2015 (see Sec. 3.1.2 for details about the stations and the measurement campaigns).

During the A-LIFE campaign, the INP spectra show a similar temperature dependence compared to the results from the INUIT-BACCHUS-ACTRIS campaign (Fig. 5.11a). Also, the INP concentrations are in the same range except for a few days of the A-LIFE measurements, where they are slightly shifted towards lower values. The measurements were both conducted in Cyprus during the same season. Paphos is located close to the Sea, while the CAO is located in the center of the island, surrounded by a rural area in the foothills of the Troodos mountains. Lofted, local soil dust dominated aerosol particles could be an explanation for the few days with increased INP concentrations at temperatures above 253 K of the CAO measurements. The slightly lower INP concentrations at lower temperatures for the A-LIFE measurements might be explained by the increased influence of marine aerosol particles.

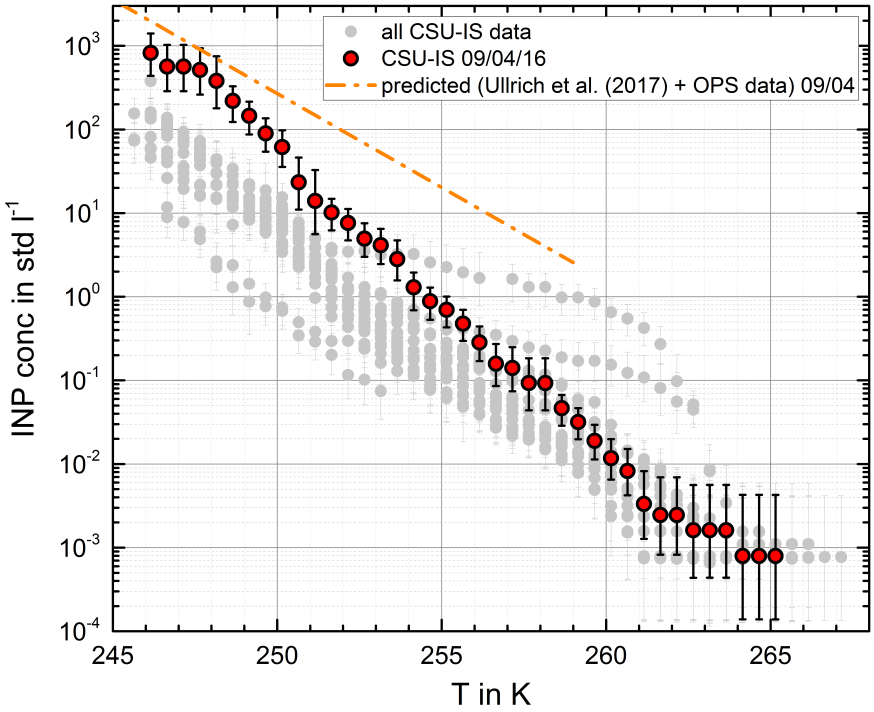

Fig. 5.10.: Comparison of measured and predicted INP concentrations for mineral dust particles. The measured INP concentrations (red circles) are from the dust day (09/04/16). The predicted INP concentrations (orange, dashed line) are obtained from the AIDA mineral dust parametrization (Ullrich et al., 2017) in combination with measured aerosol size distributions during the dust day at the CAO. OPS data courtesy of Rebecca Kohl.

INP measurements from the FIN-3 campaign also show very similar results to those taken at the CAO, even though they were conducted on a different continent at a different time of year (Fig. 5.11b).

In general, the atmospheric INP concentrations measured at three different locations show similar temperature trends with a variability of about one order of magnitude. There are only a single days, where the INP concentration is enhanced or decreased compared to the average values. Thus, the INP concentration range may be used by models as lower and upper limits for the primary ice formation in, for example, convective clouds which form on aerosols originating from the lower boundary layer, for the respective locations and time periods of the campaigns.

5.3. Summary

During the four-week campaign at the Cyprus Atmospheric Observatory in April 2016, atmospheric INP concentrations were measured on a daily basis with the offline immersion freezing method CSU-IS. Since this instrument is able to detect rather low INP concentrations, results have been obtained over a wide temperature range from about 263 K to 246 K. In this way, INP temperature spectra were measured

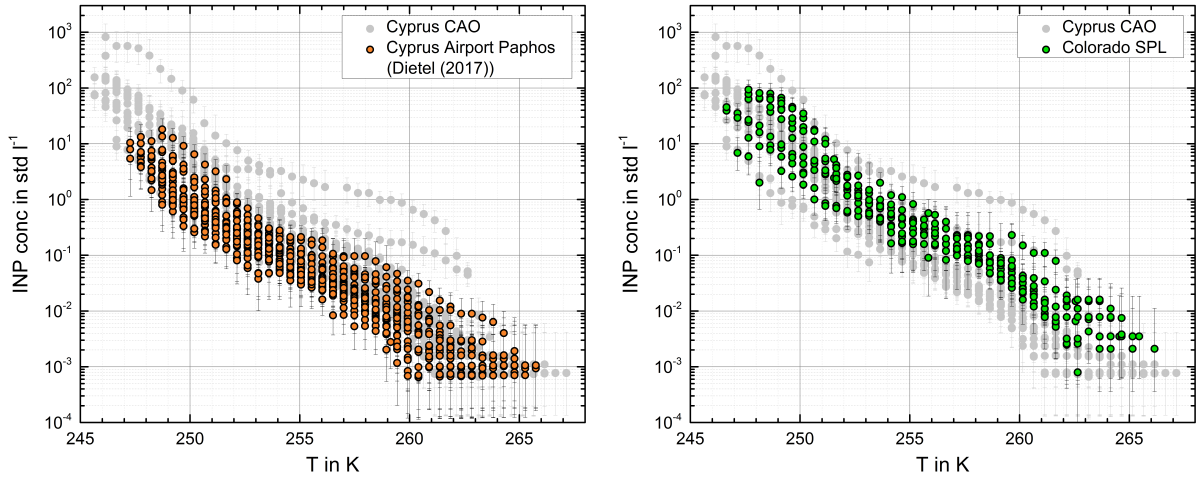

(a) Airport Paphos.

(b) Storm Peak Laboratory.

Fig. 5.11.: Comparison of the INP temperature spectra measured at the Cyprus Atmospheric Observatory with measurements conducted at the temporary measurement station at the airport Paphos during April 2017 (Dietel, 2017) and at the Storm Peak Laboratory (SPL) in Colorado during September 2015.

for days with high dust aerosol concentrations as well as for relatively clean days with very low aerosol concentrations after rainfall.

Over the entire campaign period, the INP concentration at 251 K was well correlated with the coarse mode particle concentration, which was already observed at other locations (Chou et al., 2011). This leads to the conclusion that the mineral dust aerosol, which has major contribution to the coarse mode aerosol concentration (Schwikowski et al., 1995), also mainly contributes to the observed INP concentrations measured at temperatures as low as 251 K. This conclusion is also supported by the fact that heat and hydrogen peroxide treatment of the aerosol suspensions did not much affect the INP concentration measured at temperatures below about 250 K.

At temperatures above 253 K, however, heat and hydrogen peroxide treatment markedly lowered the INP concentration in the aerosol suspensions prepared from the atmospheric aerosol filters for the CSU-IS measurements. This is in agreement to results by Hill et al. (2016) who also concluded that the INP abundance at temperatures above 253 K may be dominated by heat-sensitive INPs, which are possibly proteins or other macromolecules.

The atmospheric dust concentration was remarkably high during one day of the INUIT-BACCHUS-ACTRIS campaign (09/04/16) due to mineral dust transport form the Sahara. The INP temperature spectrum of this day clearly differed from the others. The INP concentration shows an almost exponential temperature dependence over the entire range, with higher values at lower temperatures and lower values at higher temperatures, compared to the average of the other days. Also, heat and hydrogen peroxide treatment had almost no effect on the measured INP abundance. This also strongly supports the conclu-

sion that the the INP abundance is dominated by mineral dust particles at lower temperatures, but has other major contributions at higher temperatures. For the dust dominated day on 09/04/16, we checked whether closure between measured and predicted INP concentrations can be achieved. For this purpose, the INP measurements were compared with the INP concentration calculated by using the immersion freezing parametrization for desert dust aerosols by Ullrich et al. (2017) and the aerosol measurements at the field site. Below 248 K, the predicted and the measured INP concentration agree very well, but the temperature dependence is slightly higher for the measured INP concentrations leading to an increasing discrepancy at higher temperatures. The reasons for the discrepancy of this first case study can be manifold and need to be further elaborated in future field studies at different locations and with a variety of aerosol sources and mixtures.

INP temperature spectra were measured at three different locations and during different seasons in the scope of this thesis. In general, the INP spectra follow similar temperature trends with a variability of about one order of magnitude. There are only a few days, where the INP concentration is enhanced compared to the average values. The range of INP concentration can be considered typical for the respective locations and time periods of the campaign and may be used by models as lower and upper limits for the primary ice formation in, for example, convective clouds which form on aerosols originating from the lower boundary layer.

More atmospheric measurements are required in order to further investigate the contribution of different aerosol species to the atmospheric INP abundance, in particular at temperatures above 253 K. Among other, such studies should include determination of the biological content and the chemical composition of both aeorsol and ice residual particles. Such measurements, including the ice nucleation behavior of size-selected aerosol particles, were conducted by other participants of the INUIT-BACCHUS-ACTRIS campaign at the CAO and the FIN-3 campaign at the SPL. The analysis of these measurements is still ongoing and is therefore not mentioned in this thesis.

6. Summary and Outlook

Mineral dust aerosols are generally acknowledged to be an important atmospheric INP (DeMott et al., 2003b; Cziczo et al., 2013). Recent investigations have shown an increased ice nucleation activity of arable soil dust aerosol compared to pure mineral dust aerosol (Tobo et al., 2014; Steinke et al., 2016), probably because of its content of soil organic matter and biological material. This enhanced ice nucleation of arable soil dust aerosols was confirmed and further investigated in this thesis with both laboratory experiments and field studies.

The laboratory experiments were conducted at the AIDA cloud chamber facility in the temperature range between 190 K and 256 K. For this purpose, four different natural soil samples from different locations in the world have been analyzed. The AIDA measurements were complemented by measurements with INKA and INSEKT, two new instruments for ice nucleation studies and INP measurements, which were developed and built as part of this thesis in close collaboration with the Colorado State University in Fort Collins, USA. In addition, the Colorado State University Ice Spectrometer (CSU-IS) was used to measure INP temperature spectra and the Max Planck Institute for Chemistry in Mainz also contributed to the AIDA experiments with offline INP measurements using the MINA experiment. Results from both methods were based on aerosol filter samples taken from the AIDA aerosol. Furthermore, a series of aerosol and bulk material heat treatments have been applied in order to investigate the contribution of heat-sensitive and organic-rich INPs on the ice nucleation activity of arable soil dust aerosol.

The atmospheric INP measurements of various air masses were carried out at the Storm Peak Laboratory (SPL) in Colorado and at two locations in Cyprus in the framework of the Fifth International Workshop on Ice Nucleation-3 campaign (September 2015), the INUIT-BACCHUS-ACTRIS campaign at the CAO (April 2016) and the A-LIFE campaign close to the airport Paphos (April 2017). During these field activities, INP concentrations were measured with the CSU-IS and the newly developed INSEKT instrument. Heat and hydrogen peroxide treatments were applied to elucidate the contribution of heat-sensitive and organic-rich aerosol particles to the atmospheric INP abundance.

The new online ice nucleation instrument INKA is built after the original design of Rogers (1988). It measures the ice nucleation activity of aerosol particles by exposing them to defined temperature and humidity conditions. Fast, automated humidity scans enable extensive studies of ice nucleation processes at constant aerosol temperatures between 213 K and 263 K and a relative humidity increasing continuously from about ice saturation to a temperature dependent relative humidity with respect to liquid water, ranging from about 110 % at 253 K to about 114 % at an aerosol temperature of 243 K. In this study,

INKA screened conditions typical for mixed-phase clouds and sampled the aerosols under investigation either directly from the AIDA chamber, prior to the cloud simulation run, or from a second aerosol chamber called APC (Aerosol Preparation and Characterization) to which the same aerosols were added as to the AIDA chamber. Thus, the combination of AIDA and INKA measurements allowed for a more comprehensive investigation of the same aerosols in a wide range of temperature and relative humidity. The newly built INKA instrument also participated at the FIN-2 campaign, where it was tested and calibrated with respect to AIDA and other INP instruments. Ice nucleation results for illite NX particles proved the instrument's performance and validated the new method against the results from the AIDA chamber, the well-established CSU-CFDC, and other instruments (Broadley et al., 2012; Hiranuma et al., 2015).

INSEKT is a new freezing array based on the CSU-IS design, which was originally developed by Hill et al. (2014, 2016). For this offline immersion freezing method, aerosol particles are collected on filters for certain time periods, then washed off the filter, suspended into clean water and analyzed for the content of INPs as a function of the temperature. INSEKT is sensitive to low INP concentrations, which is relevant for INP measurements at higher temperatures and for the generally low concentrations present in the atmosphere. This strongly extended the temperature range of this study towards higher temperatures and enabled INSEKT to detect ice nucleation between 248 K and about 268 K. In addition, the possibility of detecting low INP concentrations made INSEKT suitable for field measurements. In intercomparison measurements for different soil dust aerosol samples, INSEKT agreed well with the well-established CSU-IS and three other INP measurement methods.

A major result from both, the laboratory ice nucleation experiments and the field INP measurements, was the discovery of two regimes in the temperature-dependent ice nucleation activity of the mixed-phase cloud regime, for temperatures between 243 K and 268 K. The ice nucleation activity is either expressed in terms of the INAS density for the laboratory experiments or the INP number concentrations measured in the atmosphere. In the lower temperature regime below about 253 K, the ice nucleation activity follows an exponential temperature dependence with only a small variability between different samples. Heat and hydrogen peroxide treatment has almost no effect, indicating that this regime is dominated by mineral dust particles. At higher temperatures above 253 K, the ice nucleation activity varies largely between the individual samples. Heat and hydrogen peroxide treatment strongly reduce the ice nucleation activity, clearly demonstrating the important contribution of heat-sensitive or organic-rich INPs to the ice nucleation of soil dust aerosols at temperatures above 253 K.

During the INUIT-BACCHUS-ACTRIS campaign, the atmospheric dust concentration was remarkably high during one day due to mineral dust transport form the Sahara. The INP concentration of this day shows an almost exponential temperature dependence over the entire range, with higher values at lower temperatures and lower values at higher temperatures, compared to the average of the other days.

Further, the measured INP concentration were independent of heat and hydrogen peroxide treatments. This strongly supports the conclusion that the low temperature regime for mixed-phase cloud temperatures is dominated by mineral dust particles, whereas the variability at higher temperatures is caused by other INP species.

In the cirrus cloud temperature regime, two different arable soil dust aerosols were investigated with the AIDA cloud chamber. Here, the ice formation occurs far below water saturation and depends on both, the temperature and the relative humidity with respect to ice. A series of deposition nucleation experiments with one soil dust sample between 190 K and 245 K showed u-shaped isolines of the INAS density parameter in the temperature-saturation ratio diagram. Previous AIDA studies showed a similar u-shape behavior for pure mineral dust aerosols (Ullrich et al., 2017), but the pure mineral dust aerosol is less ice active at low ice supersaturations than the here investigated arable soil dust aerosol. At lower temperatures, the INAS density isoline rises with decreasing temperatures, which can be explained by classical nucleation theory. The increasing INAS density isolines with increasing temperatures above about 220 K may be due to the occurrence of the pore condensation and freezing mechanism (Marcolli, 2014) at these higher temperatures. In the transition regime, the ice nucleation activity is almost only dependent on the relative humidity. Further, the measurements with two different samples indicate that the ice nucleation activity of arable soil dust aerosol in the cirrus cloud regime is independent of the soil organic matter content.

This thesis confirmed the enhanced immersion freezing activity of arable soil dust already found in previous laboratory studies (Steinke et al., 2016). Bulk sample and aerosol treatment of four soil samples from different regions demonstrated the contribution of soil organic matter and of biological components to this enhanced ice nucleation activity, in particular at higher temperatures above about 253 K, which was also found in previous laboratory studies of natural soil samples (Tobo et al., 2014; Hill et al., 2016). Two new instruments for laboratory ice nucleation studies (INKA) and for atmospheric INP measurements (INSEKT) were successfully developed and built as part of this thesis, in close collaboration with the Colorado State University in Fort Collins, USA. Recently, important progress was achieved by developing and testing an automated version of the INSEKT laboratory setup to analyze the aerosol suspensions for the INP content. This markedly facilitates the operation of INSEKT and its efficient use for future laboratory ice nucleation studies and field INP measurements. A mobile version of INKA is still under development for future detailed analysis of atmospheric aerosols for their ice nucleation behavior with online measurements in order to be able to capture more time-resolved changes in the INP distribution.

First field application of INSEKT together with other INP methods also demonstrated and confirmed the contribution of organic and biological aerosol species to the atmospheric INP abundance at higher temperatures. In summary, all temperature spectra of INP concentrations measured during this thesis at three different continentally influenced locations showed similar temperature trends and differed from

each other by about one order of magnitude, with only a few exceptions to higher or lower INP concentrations. The range of INP concentration can be considered typical for the respective locations and time periods of the campaign and may be used by models as lower and upper limits for the primary ice formation in, for example, convective clouds which form on aerosols originating from the lower boundary layer.

An important additional aspect of future field activities is to measure the INP content in size-selected aerosols. Some size-resolved INP measurements were performed during this thesis in collaboration with the University of British Columbia, Vancouver (Mason et al., 2015). Unfortunately, results cannot be shown here because of a delay in the data analysis due to some technical issues with the aerosol sampling device. However, because some aerosol species are preferentially abundant in certain particle size ranges, size resolved INP analysis can help elucidating the sources of atmospheric INPs.

Additional aerosol and ice residual characterization measurements were conducted by other participants of the laboratory measurements and the field campaigns at the Storm Peak Lab and in Cyprus. The results from these activities are not mentioned in this thesis because data evaluation is still ongoing. However, such additional aerosol and ice residual measurements are needed to further investigate and understand the physical and chemical nature of atmospheric INPs, and by that, to better formulate and predict the amount and variability of atmospheric INPs as a function of aerosol parameters in future cloud, weather and climate models.

Acknowledgements

At this point, I would like to thank all the people who supported me during the last three years of my PhD project.

First of all, I would like to thank my referee Prof. Dr. Thomas Leisner for making this thesis possible. The scientific discussions were very helpful and contributed to the success of this thesis. I particularly appreciate his interest in the progress of the instrument development of INKA and his active contribution to the future INSEKT automated analysis.

Prof. Dr. Corinna Hoose I would like to thank for taking over the second-referee and for her great interest in my work and the useful discussions during the INUIT meetings.

I thank Dr. Ottmar Möhler for giving me the opportunity to work on such an exciting topic. He not only originally aroused my interest on ice nucleation, but also supported me with all my ideas and intentions. He introduced me to the ice nucleation community and gave me the opportunity to establish new contacts during many workshops and conferences. Only through these contacts and his trust in me to conduct independent research, I had the chance to take part at the Colorado and Cyprus field campaigns, which have greatly benefited my PhD project. Thanks to his recommendation to Dr. Paul J. DeMott and his support of my GRACE scholarship, he made it possible for me to visit the CSU for two extended research stays, which was an experience that I will never forget.

I thank Dr. Kristina Höhler for all her supervising advise, the motivation and the helpful ideas. In her organized way, she often reminded me to keep focused. Also her way of questioning things and all the useful discussion greatly contributed to the success of this thesis. It was always reassuring to having her support, and I really enjoyed working together with her.

Additionally I want to thank the whole IMK-AAF staff for the nice working atmosphere. Special thanks to Jens Nadolny for his great support during the instrument development of INKA and INSEKT. Thanks to Ines Weber, who contributed in the scope of her bachelor thesis to the automated RH scans of INKA. I would like to thank Barbara Dietel, who greatly contributed to the INSEKT development and conducted INP measurements in Cyprus 2017 in the scope of her bachelor thesis. I thank Dr. Romy Ullrich for the great atmosphere in the office and her support for the AIDA data analysis. Thanks to

the AIDA scientific team for useful discussions, especially to Dr. Robert Wagner, Dr. Naruki Hiranuma and Dr. Harald Saathof. Also, I'm very grateful to Susanne Bolz, Georg Scheurig, Olga Dombrowski, Steffen Vogt, Rainer Buschbacher, Tomasz Chudy, and Frank Schwarz for all their support.

For an unforgettable experience, I want to thank Dr. Paul J. DeMott and his group at the CSU. Not only did my scientific work greatly benefit from my time spent at CSU, but also I personally. This was made possible by the welcoming atmosphere and support of the whole group. Special thanks to Dr. Thomas C. J. Hill for introducing me to the workings of the CSU-IS, for all his support and advise in collecting the AIDA and atmospheric samples, for providing the Wyoming soil dust sample, and last but not least especially for the wonderful time in the lab. Also I would like to thank Dr. Ezra J. T. Levin for his great support during the INKA development and the FIN-3 campaign. Especially, his warm welcome and the wonderful hikes in the Rocky Mountains contributed to an unforgettable time during my research stay at CSU.

Thanks to the organizers and participants of the FIN-2 and FIN-3 campaign for the great support and the wonderful working atmosphere.

A great thanks to the organizers and participants of the INUIT-BACCHUS-ACTRIS campaign, especially to Dr. Johannes Schneider for his support of the ACTRIS scholarship, to Prof. Dr. Jean Sciare, Dr. Michael Pikridas and Iasonas Stavroulas for all their support at the CAO, to Dr. Chrysanthos Savvides for the meteorological and aerosol data from the station, and to Rebecca Kohl for the wonderful pictures from the dust and the clean day and the OPS data.

I thank all participants of the SOIL02 campaign for their great support, especially Dr. Roger Funk for the soil samples and Dr. Peter Weidler for the XRD analysis. Further Dr. Janine Fröhlich-Nowoisky, Dr. Bettina Weber, Dr. Bernhard Pummer and Petya Yordanova for the MINA measurements and the useful discussions, and Dr. Harald Saathof and Xiaoli Shen for the LAAPTOF measurements.

I would like to thank my parents, who awakened my interest in physics already at a very early age and supported me in all of my decisions.

Special thanks go to my husband for his endless patience, encouragement and support.

Nomenclature

Acronyms

ACTRIS	Aerosols, Clouds and Trace gases Research Infrastructure
AFR	aerosol flow region
A-LIFE	Absorbing aerosol layers in a changing climate: aging, LIFEtime and dynamics
AIDA	Aerosol Interactions and Dynamics in the Atmosphere
APC	aerosol preparation and characterization
APeT	AIDA PCI extractive TDL
APicT	AIDA PCI in cloud TDL
APS	aerodynamic particle sizer
AS	activation section
BACCHUS	Impact of Biogenic versus Anthropogenic emissions on Clouds and Climate: towards a Holistic UnderStanding
CAO	Cyprus Atmospheric Observatory
CCN	cloud condensation nucleus/nuclei
CFDC	continuous flow diffusion chamber
CFMC	continuous flow mixing chamber
CERN	Conseil Européen pour la recherche nucléaire
CLOUD	Cosmics Leaving OUtdoor Droplets
CI	confidence interval
CPC	condensation particle counter
CSU	Colorado State University

CSU-IS Colorado State University Ice Spectrometer

DLI Department of Labour Inspection

DLR Deutsches Zentrum für Luft- und Raumfahrt

DMA differential mobility analyzer

DT diffusion tube

ES evaporation section

ESEM environmental scanning electron microscope

FIN Fifth International Workshop on Ice Nucleation

GEOS-5 Goddard Earth Observing System Model, Version 5

HYSPLIT Hybrid Single Particle Lagrangian Integrated Trajectory

IMK-AAF Institute of Meteorology and Climate Research - Atmospheric Aerosol Research

IMCA-ZINC immersion mode cooling chamber - Zurich ice nucleation chamber

INAS ice nucleation active surface site

INKA ice nucleation instrument of the Karlsruhe Institute of Technology

INP ice nucleating particle

INSEKT ice nucleation spectrometer of the Karlsruhe Institute of Technology

INTA National Agricultural Technology Institute

INUIT Ice Nuclei Research Unit

IPR ice particle residual

KIT Karlsruhe Institute of Technology

LAAPTOF laser ablation aerosol particle time-of-flight mass spectrometer

LIDAR light detection and ranging

LT local time

MFC mass flow controller

MINA mono ice nucleation assay

MIT Massachusetts Institute of Technology

MPIC Max Planck Institute for Chemistry

NOAA National Oceanic and Atmospheric Administration

OPC optical particle counter

OPS optical particle sizer

PALMS particle analysis by laser mass spectrometry

PCF pore condensation and freezing

PCR polymerase chain reaction

PINC portable ice nucleation chamber

PM particulate matter

PNNL-CIC Pacific Northwest National Laboratory - compact ice chamber

PVC polyvinyl chloride

RH relative humidity

SDAr08 Argentinian soil dust

SDGe01 German soil dust from Gottesgabe

SDPA01 German soil dust from Paulinenaue

SDWY01 American soil dust from Wyoming

SMPS scanning mobility particle sizer

SP-APicT Single-Path AIDA PCI in cloud TDL

SP2 single particle soot photometer

SPL Storm Peak Laboratory

TDL tunable diode laser

TROPOS Leibniz Institute for Tropospheric Research

UAS unmanned aircraft system

UV ultraviolet

welas Weißlichtaerosolspektrometer

WIBS wideband integrated bioaerosol sensor

XRD X-ray diffraction

ZALF Leibniz Centre for Agricultural Landscape Research

ZINC Zurich ice nucleation chamber

Symbols

a_{dv}	cross sectional area of the detection volume
$A_{imm,dep}$	kinetic prefactor
c_n	number concentration
$c_{n,aero}$	total aerosol number concentration
$c_{n,aero}(log\, d_p)$	size distribution of the particle number concentration
$c_{n,all}$	total particle number concentration
$c_{n,ice}$	ice particle number concentration
$c_{n,inp}$	INP concentration
$c_{n,inp,liq}$	cumulative number of INP per volume of aerosol suspension
$c_{s,aero}$	total aerosol surface area concentration
$c_{s,aero}(log\, d_p)$	size distribution of the particle surface area concentration
c_w	water concentration
d	half width of the annular gap
d_a	aerodynamic diameter
d_m	mobility diameter
d_p	particle diameter
$d_{p,m}$	median diameter of the log-normal fit
d_{va}	vacuum aerodynamic diameter
d_{ve}	volume equivalent diameter
ΔE	energy barrier
η	dilution
f	geometric term
ΔF_g	free energy of germ formation
g	gravity

$(\Delta g)_{act,w}$	activation energy for self-diffusion in water
Δg^+	molar activation energy
$J_{imm,dep}$	nucleation rate for immersion freezing and deposition nucleation, respectively
k	Boltzmann constant
l_{dv}	length of the detection volume
μ	dynamic (shear) viscosity of air
M_W	molar mass of water
m_w	water content
n	amount of substance
N_{all}	number of all particles/samples
N_f	number of frozen samples
N_{ice}	number of ice crystals
n_s	ice nucleation active surface site density
N_u	number of unfrozen samples
p	pressure
$p_{s,liq}$, $p_{s,ice}$	saturation vapor pressure with respect to liquid water and ice, respectively
p_w	water vapor partial pressure
Q	total flow rate
Q_{air}	aerosol sample flow
R	universal gas constant
RH_{liq}, RH_{ice}	relative humidity with respect to liquid water and ice, respectively
ρ_0	reference density
ρ_{air}	air density
ρ_p	particle density
s	particle surface area

s_{aero}	total available aerosol surface
σ_g	geometric standard deviation of the log-normal fit
S_{liq}, S_{ice}	saturation ratio with respect to liquid water and ice, respectively
t	time
T_{aero}	temperature at the center of the aerosol lamina
T_{cold}	cold wall temperature
T_a	temperature at the cold edge a of the aerosol lamina
τ	pulse length
T_b	temperature at the warm edge b of the aerosol lamina
T_{corr}	corrected temperature
Δt	time interval
δT	temperature difference
T_g	gas temperature inside the chamber
$\bar{T}$	mean temperature
T_{raw}	raw temperature
T_{ref}	reference temperature
T_w	wall temperature of the chamber
T_{warm}	warm wall temperature
V	gas volume
v	velocity
V_{air}	volume of sampled air
V_{drop}	droplet volume per investigated sample
$\bar{v}$	mean velocity
V_m	molar volume
V_{wash}	volume of water used to suspend the aerosol particles

χ	dynamic shape factor
z	distance from the center line of the flow

A. List of Figures

B. List of Tables

C. Bibliography

Agresti, A. and B. A. Coull, 1998: Approximate is better than "exact" for interval estimation of binomial proportions. *The American Statistician*, **52**, 119–126.

Archuleta, C. M., P. DeMott, and S. Kreidenweis, 2005: Ice nucleation by surrogates for atmospheric mineral dust and mineral dust/sulfate particles at cirrus temperatures. *Atmos. Chem. Phys.*, **5**, 2617–2634.

Ardon-Dryer, K. and Z. Levin, 2014: Ground-based measurements of immersion freezing in the eastern mediterranean. *Atmos. Chem. Phys.*, **14**, 5217–5231.

Arnalds, O., P. Dagsson-Waldhauserova, and H. Olafsson, 2016: The icelandic volcanic aeolian environment: Processes and impacts - a review. *Aeolian Res.*, **20**, 176–195.

Atkinson, J. D., B. J. Murray, M. T. Woodhouse, T. F. Whale, K. J. Baustian, K. S. Carslaw, S. Dobbie, D. O'Sullivan, and T. L. Malkin, 2013: The importance of feldspar for ice nucleation by mineral dust in mixed-phase clouds. *Nature*, **498**, 355–358.

Augustin, S., H. Wex, D. Niedermeier, B. Pummer, H. Grothe, S. Hartmann, L. Tomsche, T. Clauss, J. Voigtländer, K. Ignatius, et al., 2013: Immersion freezing of birch pollen washing water. *Atmos. Chem. Phys.*, **13**, 10 989–11 003.

Augustin-Bauditz, S., H. Wex, S. Kanter, M. Ebert, D. Niedermeier, F. Stolz, A. Prager, and F. Stratmann, 2014: The immersion mode ice nucleation behavior of mineral dusts: A comparison of different pure and surface modified dusts. *Geophys. Res. Lett.*, **41**, 7375–7382.

Beall, C. M., M. D. Stokes, T. C. Hill, P. J. DeMott, J. T. DeWald, and K. A. Prather, 2017: Automation and heat transfer characterization of immersion mode spectroscopy for analysis of ice nucleating particles. *Atmospheric Measurement Techniques Discussions*, 1–25.

Benz, S., 2006: *Experimente zur Eisnukleation von Wassertröpfchen und Sulfatpartikeln bei Temperaturen zwischen -65°C und -35°C*. Dissertation, University Karlsruhe.

Benz, S., K. Megahed, O. Möhler, H. Saathoff, R. Wagner, and U. Schurath, 2005: T-dependent rate measurements of homogeneous ice nucleation in cloud droplets using a large atmospheric simulation chamber. *J. Photochem. Photobiol. A*, **176**, 208–217.

Bingemer, H., H. Klein, M. Ebert, W. Haunold, U. Bundke, T. Herrmann, K. Kandler, D. Müller-Ebert, S. Weinbruch, A. Judt, et al., 2012: Atmospheric ice nuclei in the eyjafjallajökull volcanic ash plume. *Atmos. Chem. Phys.*, **12**, 857–867.

Boose, Y., Z. A. Kanji, M. Kohn, B. Sierau, A. Zipori, I. Crawford, G. Lloyd, N. Bukowiecki, E. Herrmann, P. Kupiszewski, et al., 2016a: Ice nucleating particle measurements at 241 k during winter months at 3580 m msl in the swiss alps. *J. Atmos. Sci.*, **73**, 2203–2228.

Boose, Y., B. Sierau, M. I. Garcia, S. Rodriguez, A. Alastuey, C. Linke, M. Schnaiter, P. Kupiszewski, Z. A. Kanji, and U. Lohmann, 2016b: Ice nucleating particles in the saharan air layer. *Atmos. Chem. Phys.*, **16**, 9067–9087.

Boose, Y., A. Welti, J. Atkinson, F. Ramelli, A. Danielczok, H. G. Bingemer, M. Plötze, B. Sierau, Z. A. Kanji, and U. Lohmann, 2016c: Heterogeneous ice nucleation on dust particles sourced from nine deserts worldwide-Part 1: Immersion freezing. *Atmos. Chem. Phys.*, **16**, 15 075–15 095.

Borys, R. D. and M. A. Wetzel, 1997: Storm peak laboratory: A research, teaching, and service facility for the atmospheric sciences. *Bull. Am. Meteorol. Soc.*, **78**, 2115–2123.

Broadley, S., B. Murray, R. Herbert, J. Atkinson, S. Dobbie, T. Malkin, E. Condliffe, and L. Neve, 2012: Immersion mode heterogeneous ice nucleation by an illite rich powder representative of atmospheric mineral dust. *Atmos. Chem. Phys.*, **12**, 287–307.

Brown, L. D., T. T. Cai, and A. DasGupta, 2001: Interval estimation for a binomial proportion. *Statistical Science*, **16**, 101–117.

Budke, C. and T. Koop, 2015: Binary: an optical freezing array for assessing temperature and time dependence of heterogeneous ice nucleation. *Atmos. Meas. Tech.*, **8**, 689–703.

Bullard, J. E. and M. J. Austin, 2011: Dust generation on a proglacial floodplain, west greenland. *Aeolian Res.*, **3**, 43–54.

Bundke, U., B. Nillius, R. Jaenicke, T. Wetter, H. Klein, and H. Bingemer, 2008: The fast ice nucleus chamber finch. *Atmos. Res.*, **90**, 180–186.

Buschiazzo, D. E. and R. Funk, 2015: Wind Erosion of Agricultural Soils and the Carbon Cycle. *in: Soil Carbon: Science, Management and Policy for Multiple Benefits*, 161–168.

Cantrell, W. and A. Heymsfield, 2005: Production of ice in tropospheric clouds: A review. *Bull. Am. Meteorol. Soc.*, **86**, 795–807.

Choi, Y.-S., R. S. Lindzen, C.-H. Ho, and J. Kim, 2010: Space observations of cold-cloud phase change. *Proc. Natl. Acad. Sci.*, **107**, 11 211–11 216.

Chou, C., O. Stetzer, E. Weingartner, Z. Jurányi, Z. Kanji, and U. Lohmann, 2011: Ice nuclei properties within a saharan dust event at the jungfraujoch in the swiss alps. *Atmos. Chem. Phys.*, **11**, 4725–4738.

Connolly, P., O. Möhler, P. Field, H. Saathoff, R. Burgess, T. Choularton, and M. Gallagher, 2009: Studies of heterogeneous freezing by three different desert dust samples. *Atmos. Chem. Phys.*, **9**, 2805–2824.

Curtius, J., 2006: Nucleation of atmospheric aerosol particles. *C. R. Phys.*, **7**, 1027 – 1045.

Cziczo, D. J., K. D. Froyd, C. Hoose, E. J. Jensen, M. Diao, M. A. Zondlo, J. B. Smith, C. H. Twohy, and D. M. Murphy, 2013: Clarifying the dominant sources and mechanisms of cirrus cloud formation. *Science*, **340**, 1320–1324.

DeCarlo, P. F., J. G. Slowik, D. R. Worsnop, P. Davidovits, and J. L. Jimenez, 2004: Particle morphology and density characterization by combined mobility and aerodynamic diameter measurements. part 1: Theory. *Aerosol Sci. Tech.*, **38**, 1185–1205.

DeMott, P., D. Cziczo, A. Prenni, D. Murphy, S. Kreidenweis, D. Thomson, R. Borys, and D. Rogers, 2003a: Measurements of the concentration and composition of nuclei for cirrus formation. *Proc. Natl. Acad. Sci. USA*, **100**, 14 655–14 660.

DeMott, P. J., T. C. J. Hill, M. D. Petters, A. K. Bertram, Y. Tobo, R. H. Mason, K. J. Suski, C. S. McCluskey, E. J. T. Levin, G. P. Schill, Y. Boose, A. M. Rauker, A. J. Miller, J. Zaragoza, K. Rocci, N. E. Rothfuss, H. P. Taylor, J. D. Hader, C. Chou, J. A. Huffman, U. Pöschl, A. J. Prenni, and S. M. Kreidenweis, 2017a: Comparative measurements of ambient atmospheric concentrations of ice nucleating particles using multiple immersion freezing methods and a continuous flow diffusion chamber. *Atmos. Chem. Phys. Discuss.*, 1–29.

DeMott, P. J., O. Möhler, O. Stetzer, G. Vali, Z. Levin, M. D. Petters, M. Murakami, T. Leisner, U. Bundke, H. Klein, et al., 2011: Resurgence in ice nuclei measurement research. *Bull. Amer. Meteor. Soc.*, **92**, 1623–1635.

DeMott, P. J., A. J. Prenni, X. Liu, S. M. Kreidenweis, M. D. Petters, C. H. Twohy, M. Richardson, T. Eidhammer, and D. Rogers, 2010: Predicting global atmospheric ice nuclei distributions and their impacts on climate. *Proc. Natl. Acad. Sci.*, **107**, 11 217–11 222.

DeMott, P. J., A. J. Prenni, G. R. McMeeking, R. C. Sullivan, M. D. Petters, Y. Tobo, M. Niemand, O. Möhler, J. R. Snider, Z. Wang, et al., 2015: Integrating laboratory and field data to quantify the immersion freezing ice nucleation activity of mineral dust particles. *Atmos. Chem. Phys.*, **15**, 393–409.

DeMott, P. J. and D. C. Rogers, 1990: Freezing Nucleation Rates of Dilute Solution Droplets Measured between -30° and -40°C in Laboratory Simulations of Natural Clouds. *J. Atmos. Sci.*, **47**, 1056–1064.

DeMott, P. J., K. Sassen, M. R. Poellot, D. Baumgardner, D. C. Rogers, S. D. Brooks, A. J. Prenni, and S. M. Kreidenweis, 2003b: African dust aerosols as atmospheric ice nuclei. *Geophys. Res. Lett.*, **30 (14)**.

DeMott, P. J. et al., 2017b: Overview of results from the fifth international workshop on ice nucleation part 2 (fin-02): Laboratory intercomparisons of ice nucleation measurements. *In preparation for submission to Atmos. Chem. Phys.*

Després, V. R., J. A. Huffman, S. M. Burrows, C. Hoose, A. S. Safatov, G. Buryak, J. Fröhlich-Nowoisky, W. Elbert, M. O. Andreae, U. Pöschl, et al., 2012: Primary biological aerosol particles in the atmosphere: a review. *Tellus B*, **64**.

Diehl, K., M. Debertshäuser, O. Eppers, H. Schmithüsen, S. Mitra, and S. Borrmann, 2014: Particle surface area dependence of mineral dust in immersion freezing mode: investigations with freely suspended drops in an acoustic levitator and a vertical wind tunnel. *Atmos. Chem. Phys.*, **14**, 12 343–12 355.

Dietel, B., 2017: *Eisbildungsaktivität von atmosphärischem Aerosol über Zypern - Erste Experimente mit dem Tröpfchengefrierexperiment INSEKT*. Bachelor Thesis, Karlsruhe Institute of Technology.

Engelstaedter, S., I. Tegen, and R. Washington, 2006: North African dust emissions and transport. *Earth Sci. Rev.*, **79**, 73–100.

Fahey, D., R.-S. Gao, O. Möhler, H. Saathoff, C. Schiller, V. Ebert, M. Krämer, T. Peter, N. Amarouche, L. Avallone, et al., 2014: The AquaVIT-1 intercomparison of atmospheric water vapor measurement techniques. *Atmos. Meas. Tech.*, **7**, 3177–3213.

Fröhlich-Nowoisky, J., S. Burrows, Z. Xie, G. Engling, P. Solomon, M. Fraser, O. Mayol-Bracero, P. Artaxo, D. Begerow, R. Conrad, M. Andreae, V. Deprés, and U. Pöschl, 2012: Biogeography in the air: fungal diversity over land and oceans. *Biogeosciences*, **9**, 1125–1136.

Fröhlich-Nowoisky, J., T. C. Hill, B. G. Pummer, P. Yordanova, G. D. Franc, and U. Pöschl, 2015: Ice nucleation activity in the widespread soil fungus mortierella alpina. *Biogeosciences*, **12**, 1057–1071.

Funk, R., H. I. Reuter, C. Hoffmann, W. Engel, and D. Öttl, 2008: Effect of moisture on fine dust emission from tillage operations on agricultural soils. *Earth Surf. Process. Landforms*, **33**, 1851–1863.

Garimella, S., T. Kristensen, K. Ignatius, A. Welti, J. Voigtländer, G. Kulkarni, F. Sagan, G. Kok, J. Dorsey, L. Nichman, et al., 2016: The spectrometer for ice nuclei (spin): an instrument to investigate ice nucleation. *Atmos. Meas. Tech.*, **9**, 2781–2795.

Gemayel, R., S. Hellebust, B. Temime-Roussel, N. Hayeck, J. T. V. Elteren, H. Wortham, and S. Gligorovski, 2016: The performance and the characterization of laser ablation aerosol particle time-of-flight mass spectrometry (laap-tof-ms). *Atmos. Meas. Tech.*, **9**, 1947–1959.

Glen, A. and S. D. Brooks, 2014: Single particle measurements of the optical properties of small ice crystals and heterogeneous ice nuclei. *Aerosol Sci. Tech.*, **48**, 1123–1132.

Hagen, D. E., R. J. Anderson, and J. L. Kassner Jr, 1981: Homogeneous condensation-freezing nucleation rate measurements for small water droplets in an expansion cloud chamber. *J. Atmos. Sci.*, **38**, 1236–1243.

Hill, T. C., P. J. DeMott, Y. Tobo, J. Fröhlich-Nowoisky, B. F. Moffett, G. D. Franc, and S. M. Kreidenweis, 2016: Sources of organic ice nucleating particles in soils. *Atmos. Chem. Phys.*, **16**, 7195–7211.

Hill, T. C., B. F. Moffett, P. J. DeMott, D. G. Georgakopoulos, W. L. Stump, and G. D. Franc, 2014: Measurement of ice nucleation-active bacteria on plants and in precipitation by quantitative pcr. *Appl. Environ. Microbiol.*, **80**, 1256–1267.

Hiranuma, N., S. Augustin-Bauditz, H. Bingemer, C. Budke, J. Curtius, A. Danielczok, K. Diehl, K. Dreischmeier, M. Ebert, F. Frank, et al., 2015: A comprehensive laboratory study on the immersion freezing behavior of illite nx particles: a comparison of 17 ice nucleation measurement techniques. *Atmos. Chem. Phys.*, **15 (5)**, 2489–2518.

Hiranuma, N., M. Paukert, I. Steinke, K. Zhang, G. Kulkarni, C. Hoose, M. Schnaiter, H. Saathoff, and O. Möhler, 2014: A comprehensive parameterization of heterogeneous ice nucleation of dust surrogate: laboratory study with hematite particles and its application to atmospheric models. *Atmos. Chem. Phys.*, **14**, 13 145–13 158.

Hoffmann, N., A. Kiselev, D. Rzesanke, D. Duft, and T. Leisner, 2013: Experimental quantification of contact freezing in an electrodynamic balance. *Atmos. Meas. Tech.*, **6**, 2373–2382.

Hoose, C., J. E. Kristjánsson, J.-P. Chen, and A. Hazra, 2010: A classical-theory-based parameterization of heterogeneous ice nucleation by mineral dust, soot, and biological particles in a global climate model. *J. Atmos. Sci.*, **67**, 2483–2503.

Hoose, C. and O. Möhler, 2012: Heterogeneous ice nucleation on atmospheric aerosols: a review of results from laboratory experiments. *Atmos. Chem. Phys.*, **12**, 9817–9854.

Hoyle, C. R., V. Pinti, A. Welti, B. Zobrist, C. Marcolli, B. Luo, . Höskuldsson, H. B. Mattsson, O. Stetzer, T. Thorsteinsson, G. Larsen, and T. Peter, 2011: Ice nucleation properties of volcanic ash from eyjafjallajökull. *Atmos. Chem. Phys.*, **11**, 9911–9926.

Huffman, J. A., A. Prenni, P. DeMott, C. Pöhlker, R. Mason, N. Robinson, J. Fröhlich-Nowoisky, Y. Tobo, V. Després, E. Garcia, et al., 2013: High concentrations of biological aerosol particles and ice nuclei during and after rain. *Atmos. Chem. Phys.*, **13**, 6151–6164.

Huneeus, N., M. Schulz, Y. Balkanski, J. Griesfeller, J. Prospero, S. Kinne, S. Bauer, O. Boucher, M. Chin, et al., 2011: Global dust model intercomparison in AeroCom phase I. *Atmos. Chem. Phys.*, **11**, 7781–7816.

Iannone, R., D. Chernoff, A. Pringle, S. Martin, and A. Bertram, 2011: The ice nucleation ability of one of the most abundant types of fungal spores found in the atmosphere. *Atmos. Chem. Phys.*, **11**, 1191–1201.

Ickes, L., A. Welti, C. Hoose, and U. Lohmann, 2015: Classical nucleation theory of homogeneous freezing of water: thermodynamic and kinetic parameters. *Phys. Chem. Chem. Phys.*, **17**, 5514–5537.

Ickes, L., A. Welti, and U. Lohmann, 2017: Classical nucleation theory of immersion freezing: sensitivity of contact angle schemes to thermodynamic and kinetic parameters. *Atmos. Chem. Phys.*, **17**, 1713–1739.

Kaaden, N., A. Massling, A. Schladitz, T. Müller, K. Kandler, L. Schütz, B. Weinzierl, A. Petzold, M. Tesche, S. Leinert, et al., 2009: State of mixing, shape factor, number size distribution, and hygroscopic growth of the Saharan anthropogenic and mineral dust aerosol at Tinfou, Morocco. *Tellus B*, **61**, 51–63.

Kalikmanov, V. I., 2013: *Nucleation Theory*. Springer, Dordrecht.

Kamphus, M., M. Ettner-Mahl, T. Klimach, F. Drewnick, L. Keller, D. J. Cziczo, S. Mertes, S. Borrmann, and J. Curtius, 2010: Chemical composition of ambient aerosol, ice residues and cloud droplet residues in mixed-phase clouds: single particle analysis during the cloud and aerosol characterization experiment (clace 6). *Atmos. Chem. Phys.*, **10**, 8077–8095.

Kandler, K., L. Schütz, C. Deutscher, M. Ebert, H. Hofmann, S. Jäckel, R. Jaenicke, P. Knippertz, K. Lieke, A. Massling, et al., 2009: Size distribution, mass concentration, chemical and mineralogical composition and derived optical parameters of the boundary layer aerosol at Tinfou, Morocco, during SAMUM 2006. *Tellus B*, **61**, 32–50.

Kanji, Z. A. and J. P. D. Abbatt, 2009: The university of toronto continuous flow diffusion chamber (ut-cfdc): A simple design for ice nucleation studies. *Aerosol Sci. Tech.*, **43**, 730–738.

Kanji, Z. A. et al., 2017: Inp intercomparison study of the inuit-bacchus-actris campaign in cyprus in april 2016. *In preparation*.

Kirkby, J., J. Duplissy, K. Sengupta, C. Frege, H. Gordon, C. Williamson, M. Heinritzi, M. Simon, C. Yan, J. Almeida, et al., 2016: Ion-induced nucleation of pure biogenic particles. *Nature*, **533 (7604)**, 521–526.

Knippertz, P., 2017: Mineral dust generation across northern africa and its impacts. *Oxford Research Encyclopedia of Climate Science*, 1–50.

Koehler, K., S. Kreidenweis, P. DeMott, M. Petters, A. Prenni, and O. Möhler, 2010: Laboratory investigations of the impact of mineral dust aerosol on cold cloud formation. *Atmos. Chem. Phys.*, **10**, 1195–11 968.

Kok, J. F., D. A. Ridley, Q. Zhou, R. L. Miller, C. Zhao, C. L. Heald, D. S. Ward, S. Albani, and K. Haustein, 2017: Smaller desert dust cooling effect estimated from analysis of dust size and abundance. *Nat. Geosci.*, **10**, 274–278.

Koop, T., 2004: Homogeneous ice nucleation in water and aqueous solutions. *Z. Phys. Chem.*, **218**, 1231–1258.

Koren, I., Y. J. Kaufman, R. Washington, M. C. Todd, Y. Rudich, J. V. Martins, and D. Rosenfeld, 2006: The Bodélé depression: a single spot in the Sahara that provides most of the mineral dust to the Amazon forest. *Environ. Res. Lett.*, **1**, 014 005.

Lacher, L., U. Lohmann, Y. Boose, A. Zipori, E. Herrmann, N. Bukowiecki, M. Steinbacher, and Z. A. Kanji, 2017: The horizontal ice nucleation chamber hinc: Inp measurements at conditions relevant for mixed-phase clouds at the high altitude research station jungfraujoch. *Atmos. Chem. Phys. Discuss.*, 1–49.

Levin, Z., E. Ganor, and V. Gladstein, 1996: The effects of desert particles coated with sulfate on rain formation in the eastern mediterranean. *J. Appl. Meteorol.*, **35**, 1511–1523.

Mahowald, N., S. Albani, J. F. Kok, S. Engelstaeder, R. Scanza, D. S. Ward, and M. G. Flanner, 2014: The size distribution of desert dust aerosols and its impact on the earth system. *Aeolian Res.*, **15**, 53–71.

Marcolli, C., 2014: Deposition nucleation viewed as homogeneous or immersion freezing in pores and cavities. *Atmos. Chem. Phys.*, **14**, 2071–2104.

Mason, R., C. Chou, C. McCluskey, E. Levin, C. Schiller, T. Hill, J. Huffman, P. DeMott, and A. Bertram, 2015: The micro-orifice uniform deposit impactor-droplet freezing technique (moudi-dft) for measuring concentrations of ice nucleating particles as a function of size: improvements and initial validation. *Atmos. Meas. Tech.*, **8**, 2449–2462.

Mason, R., M. Si, C. Chou, V. Irish, R. Dickie, P. Elizondo, R. Wong, M. Brintnell, M. Elsasser, W. Lassar, et al., 2016: Size-resolved measurements of ice-nucleating particles at six locations in north america and one in europe. *Atmos. Chem. Phys.*, **16**, 1637–1651.

McCluskey, C. S., T. C. J. Hill, C. M. Sultana, O. Laskina, J. Trueblood, M. V. Santander, C. M. Beall, J. M. Michaud, K. A. Prather, V. H. Grassian, and P. J. DeMott, 2017: A mesocosm double feature: Insights into the chemical make-up of marine ice nucleating particles. *Submitted to J. Atmos. Sci.*

Mie, G., 1908: Beiträge zur Optik trüber Medien, speziell kolloidaler Metallösungen. *Ann. Phys.*, **330**, 377–445.

Mikutta, R., M. Kleber, K. Kaiser, and R. Jahn, 2005: Review: Organic Matter Removal from Soils using Hydrogen Peroxide, Sodium Hypochlorite, and Disodium Peroxodisulfate. *Soil Sci. Soc. Am. J.*, **69**, 120–135.

Möhler, O., S. Büttner, C. Linke, M. Schnaiter, H. Saathoff, O. Stetzer, R. Wagner, M. Krämer, A. Mangold, V. Ebert, and U. Schurath, 2005: Effect of sulfuric acid coating on heterogeneous ice nucleation by soot aerosol particles. *J. Geophys. Res.*, **110**, D11 210.

Möhler, O., P. Field, P. Connolly, S. Benz, H. Saathoff, M. Schnaiter, R. Wagner, R. Cotton, M. Krämer, A. Mangold, and A. Heymsfield, 2006: Efficiency of the deposition mode ice nucleation on mineral dust particles. *Atmos. Chem. Phys.*, **6**, 3007–3021.

Möhler, O., D. Georgakopoulos, C. Morris, S. Benz, V. Ebert, S. Hunsmann, H. Saathoff, M. Schnaiter, and R. Wagner, 2008: Heterogeneous ice nucleation activity of bacteria: new laboratory experiments at simulated cloud conditions. *Biogeosciences*, **5**, 1425–1435.

Möhler, O., O. Stetzer, S. Schaefers, C. Linke, M. Schnaiter, R. Tiede, H. Saathoff, M. Krämer, A. Mangold, P. Budz, P. Zink, J. Schreiner, K. Mauersberger, W. Haag, B. Kärcher, and U. Schurath, 2003: Experimental investigation of homogeneous freezing of sulphuric acid particles in the aerosol chamber AIDA. *Atmos. Chem. Phys.*, **3**, 211–223.

Murphy, D. M. and T. Koop, 2005: Review of the vapour pressures of ice and supercooled water for atmospheric applications. *Quart. J. R. Met. Soc.*, **131**, 1539–1565.

Murray, B., D. O'Sullivan, J. Atkinson, and M. Webb, 2012: Ice nucleation by particles immersed in supercooled cloud droplets. *Chem. Soc. Rev.*, **41**, 6519–6554.

NASA/Goddard, 2016: Portrait of global aerosols by William Putman. *URL https://www.nasa.gov/multimedia/imagegallery/image_feature_2393.html*, [accessed 12.04.2017].

Némethy, G. and H. A. Scheraga, 1962: Structure of water and hydrophobic bonding in proteins. i. a model for the thermodynamic properties of liquid water. *J. Chem. Phys.*, **36**, 3382–3400.

Niedermeier, D., R. Shaw, S. Hartmann, H. Wex, T. Clauss, J. Voigtländer, and F. Stratmann, 2011: Heterogeneous ice nucleation: exploring the transition from stochastic to singular freezing behavior. *Atmos. Chem. Phys.*, **11**, 8767–8775.

Niemand, M., O. Möhler, B. Vogel, H. Vogel, C. Hoose, P. Connolly, H. Klein, H. Bingemer, P. DeMott, J. Skrotzki, et al., 2012: A particle-surface-area-based parameterization of immersion freezing on desert dust particles. *J. Atmos. Sci.*, **69**, 3077–3092.

O'Sullivan, D., B. Murray, T. Malkin, T. Whale, N. Umo, J. Atkinson, H. Price, K. Baustian, J. Browse, and M. Webb, 2014: Ice nucleation by fertile soil dusts: relative importance of mineral and biogenic components. *Atmos. Chem. Phys.*, **14**, 1853–1867.

PALAS, 2010: *Bedienungsanleitung Streulichtspektrometer Promo 2000*. PALAS GmbH, Karlsruhe.

Peckhaus, A., A. Kiselev, T. Hiron, M. Ebert, and T. Leisner, 2016: A comparative study of k-rich and na/ca-rich feldspar ice-nucleating particles in a nanoliter droplet freezing assay. *Atmos. Chem. Phys.*, **16**, 11 477–11 496.

Petters, M. D., M. T. Parsons, A. J. Prenni, P. J. DeMott, S. M. Kreidenweis, C. M. Carrico, A. P. Sullivan, G. R. McMeeking, E. Levin, C. E. Wold, J. L. J. Collett, and H. Moosmüller, 2009: Ice nuclei emissions from biomass burning. *J. Geophys. Res.*, **114**.

Prenni, A., Y. Tobo, E. Garcia, P. DeMott, J. Huffman, C. McCluskey, S. Kreidenweis, J. Prenni, C. Pöhlker, and U. Pöschl, 2013: The impact of rain on ice nuclei populations at a forested site in colorado. *Geophys. Res. Lett.*, **40**, 227–231.

Prenni, A. J., P. J. Demott, D. C. Rogers, S. M. Kreidenweis, G. M. McFarquhar, G. Zhang, and M. R. Poellot, 2009: Ice nuclei characteristics from m-pace and their relation to ice formation in clouds. *Tellus B*, **61**, 436–448.

Prospero, J. M., 1999: Long-range transport of mineral dust in the global atmosphere: Impact of African dust on the environment of the southeastern United States. *Proc. Natl. Acad. Sci.*, **96**, 3396–3403.

Prospero, J. M., P. Ginoux, O. Torres, S. E. Nicholson, and T. E. Gill, 2002: Environmental characterization of global sources of atmospheric soil dust identified with the nimbus 7 total ozone mapping spectrometer (toms) absorbing aerosol product. *Rev. Geophys.*, **40**.

Pruppacher, H. and J. Klett, 1997: *Microphysics of Clouds and Precipitation*. Kluwer Acadamic Publishers, Dordrecht.

Pruppacher, H. R., 1995: A new look at homogeneous ice nucleation in supercooled water drops. *J. Atmos. Sci.*, **52**, 1924–1933.

Pummer, B., C. Budke, S. Augustin-Bauditz, D. Niedermeier, L. Felgitsch, C. Kampf, R. Huber, K. Liedl, T. Loerting, T. Moschen, et al., 2015: Ice nucleation by water-soluble macromolecules. *Atmos. Chem. Phys.*, **15**, 4077–4091.

Richardson, M., 2009: Making real time measurements of ice nuclei concentrations at upper tropospheric temperatures: Extending the capabilities of the continuous flow diffusion chamber. Ph.D. thesis, Colorado State University.

Riechers, B., F. Wittbracht, A. Hütten, and T. Koop, 2013: The homogeneous ice nucleation rate of water droplets produced in a microfluidic device and the role of temperature uncertainty. *Phys. Chem. Chem. Phys.*, **15**, 5873–5887.

Roedel, W. and T. Wagner, 2011: *Physik unserer Umwelt: die Atmosphäre*. 4th ed., Springer, Heidelberg.

Rogers, D. C., 1988: Development of a continuous flow thermal gradient diffusion chamber for ice nucleation studies. *Atmos. Res.*, **22 (2)**, 149–181.

Rogers, D. C., P. J. DeMott, S. M. Kreidenweis, and Y. Chen, 1998: Measurements of ice nucleating aerosols during success. *Geophys. Res. Lett.*, **25**, 1383–1386.

———, 2001: A continuous-flow diffusion chamber for airborne measurements of ice nuclei. *J. Atmos. Oceanic Technol.*, **18 (5)**, 725–741.

Rolph, G., A. Stein, and B. Stunder, 2017: Real-time Environmental Applications and Display sYstem: READY. *Environ. Model. Soft.*, **95**, 210–228.

Rzesanke, D., J. Nadolny, D. Duft, R. Müller, A. Kiselev, and T. Leisner, 2012: On the role of surface charges for homogeneous freezing of supercooled water microdroplets. *Phys. Chem. Chem. Phys.*, **14 (26)**, 9359–9363.

Schiebel, T., 2014: *Homogeneous Freezing of Water Droplets and its Dependence on Droplet Size*. Diploma Thesis, Karlsruhe Institute of Technology.

Schmidt, S., J. Schneider, T. Klimach, S. Mertes, L. P. Schenk, P. Kupiszewski, J. Curtius, and S. Borrmann, 2017: Online single particle analysis of ice particle residuals from mountain-top mixed-phase clouds using laboratory derived particle type assignment. *Atmos. Chem. Phys.*, **17**, 575–594.

Schrod, J., A. Danielczok, D. Weber, M. Ebert, E. S. Thomson, and H. Bingemer, 2016: Re-evaluating the frankfurt isothermal static diffusion chamber for ice nucleation. *Atmos. Meas. Tech.*, **9**, 1313–1324.

Schrod, J., D. Weber, J. Drücke, C. Keleshis, M. Pikridas, M. Ebert, B. Cvetković, S. Nickovic, E. Marinou, H. Baars, et al., 2017: Ice nucleating particles over the eastern mediterranean measured by unmanned aircraft systems. *Atmos. Chem. Phys.*, **17**, 4817–4835.

Schwikowski, M., P. Seibert, U. Baltensperger, and H. Gaggeler, 1995: A study of an outstanding Saharan dust event at the high-alpine site Jungfraujoch, Switzerland. *Atmos. Environ.*, **29**, 1829–1842.

Seinfeld, J. H. and S. N. Pandis, 2016: *Atmospheric chemistry and physics: from air pollution to climate change*. 3d ed., Wiley, Hoboken.

Shao, Y., M. Ishizuka, M. Mikami, and J. Leys, 2011: Parameterization of size-resolved dust emission and validation with measurements. *J. Geophys. Res. Atmos.*, **116**.

Shen, X. L., R. Ramisetty, C. Mohr, W. Huang, T. Leisner, and H. Saathoff, 2017: A Laser ablation aerosol particle time-of-flight mass spectrometer (LAAPTOF): Performance, reference spectra and classification of atmospheric samples. *In preparation*.

Sokolik, I. N. and O. B. Toon, 1999: Incorporation of mineralogical composition into models of the radiative properties of mineral aerosol from uv to ir wavelengths. *J. Geophys. Res. Atmos.*, **104**, 9423–9444.

Stein, A., R. R. Draxler, G. D. Rolph, B. J. Stunder, M. Cohen, and F. Ngan, 2015: NOAA's hysplit atmospheric transport and dispersion modeling system. *Bull. Amer. Meteor. Soc.*, **96**, 2059–2077.

Steinke, I., R. Funk, J. Busse, A. Iturri, S. Kirchen, M. Leue, O. Möhler, T. Schwartz, M. Schnaiter, B. Sierau, et al., 2016: Ice nucleation activity of agricultural soil dust aerosols from mongolia, argentina, and germany. *J. Geophys. Res.*, **121**.

Steinke, I., O. Möhler, A. Kiselev, M. Niemand, H. Saathoff, M. Schnaiter, J. Skrotzki, C. Hoose, and T. Leisner, 2011: Ice nucleation properties of fine ash particles from the eyjafjallajökull eruption in April 2010. *Atmos. Chem. Phys.*, **11**, 12 945–12 958.

Stetzer, O., B. Baschek, F. Lüönd, and U. Lohmann, 2008: The zurich ice nucleation chamber (zinc)-a new instrument to investigate atmospheric ice formation. *Aerosol Sci. Tech.*, **42**, 64–74.

Stocker, T. et al., 2013: *Climate Change 2013: The Physical Science Basis: Working Group I Contribution to the Fifth Assessment Report of the Intergovernmental Panel on Climate Change*. Cambridge Univ. Press, Cambridge and New York.

Tegen, I. and A. A. Lacis, 1996: Modeling of particle size distribution and its influence on the radiative properties of mineral dust aerosol. *J. Geophys. Res. Atmos.*, **101**, 19 237–19 244.

Tobo, Y., P. DeMott, T. Hill, A. Prenni, N. Swoboda-Colberg, G. Franc, and S. Kreidenweis, 2014: Organic matter matters for ice nuclei of agricultural soil origin. *Atmos. Chem. Phys.*, **14**, 8521–8531.

Tröstl, J., W. K. Chuang, H. Gordon, M. Heinritzi, C. Yan, U. Molteni, L. Ahlm, C. Frege, F. Bianchi, R. Wagner, et al., 2016: The role of low-volatility organic compounds in initial particle growth in the atmosphere. *Nature*, **533 (7604)**, 527–531.

TSI, 2002: *Model 3010 Condensation Particle Counter Instruction Manual*. TSI.

———, 2009: *Series 3080 Operation and Service Manual*. TSI.

———, 2012: *Model 3321 Aerodynamic Particle Sizer Spectrometer - Operation and Service Manual*. TSI.

Ullrich, R., C. Hoose, O. Möhler, M. Niemand, R. Wagner, K. Höhler, N. Hiranuma, H. Saathoff, and T. Leisner, 2017: A new ice nucleation active site parameterization for desert dust and soot. *J. Atmos. Sci.*, **74**, 699–717.

Vali, G., 1971: Quantitative evaluation of experimental results an the heterogeneous freezing nucleation of supercooled liquids. *J. Atmos. Sci.*, **28**, 402–409.

———, 1999: Ice nucleation-theory: A tutorial. *Presented at the NCAR/ASP 1999 Summer Colloquium*, unpublished.

Vali, G., P. DeMott, O. Möhler, and T. Whale, 2015: Technical note: A proposal for ice nucleation terminology. *Atmos. Chem. Phys.*, **15**, 10 263–10 270.

Vogel, F., 2016: *Laborexperimente zur Eisnukleation auf Wüstenstaubaerosolen bei Temperaturen der oberen Troposphäre*. Bachelor Thesis, Karlsruhe Institute of Technology.

Wagner, R., K. Höhler, W. Huang, A. Kiselev, O. Möhler, C. Mohr, A. Pajunoja, H. Saathoff, T. Schiebel, X. Shen, et al., 2017: Heterogeneous ice nucleation of α-pinene SOA particles before and after ice cloud processing. *J. Geophys. Res. Atmos.*, **122**, 4924–4943.

Wagner, R., A. Kiselev, O. Möhler, H. Saathoff, and I. Steinke, 2016: Pre-activation of ice-nucleating particles by the pore condensation and freezing mechanism. *Atmos. Chem. Phys.*, **16**, 2025–2042.

Wagner, R., C. Linke, K.-H. Naumann, M. Schnaiter, M. Vragel, M. Gangl, and H. Horvath, 2009: A review of optical measurements at the aerosol and cloud chamber aida. *J. Quant. Spectr. Rad. T.*, **110**, 930–949.

Wagner, R. and O. Möhler, 2013: Heterogeneous ice nucleation ability of crystalline sodium chloride dihydrate particles. *J. Geophys. Res. Atmos.*, **118**, 4610–4622.

Weinzierl, B., A. Ansmann, J. Prospero, D. Althausen, N. Benker, F. Chouza, M. Dollner, D. Farrell, W. Fomba, V. Freudenthaler, et al., 2017: The Saharan Aerosol Long-range Transport and Aerosol-Cloud-Interaction Experiment (SALTRACE): overview and selected highlights. *Bull. Amer. Meteor. Soc.*, **98**, 1–25.

Wex, H., S. Augustin-Bauditz, Y. Boose, C. Budke, J. Curtius, K. Diehl, A. Dreyer, F. Frank, S. Hartmann, N. Hiranuma, et al., 2015: Intercomparing different devices for the investigation of ice nucleating particles using snomax® as test substance. *Atmos. Chem. Phys.*, **15**, 1463–1485.

Whitby, K. T., 1978: The physical characteristics of sulfur aerosols. *Atmos. Env.*, **12**, 135–159.

Whytlaw-Gray, R., J. Speakman, and J. Campbell, 1923: Smokes: Part i. a study of their behaviour and a method of determining the number of particles they contain. *Proc. Roy. Soc.*, **102**, 600–615.

Wright, T. P. and M. D. Petters, 2013: The role of time in heterogeneous freezing nucleation. *J. Geophys. Res. Atmos.*, **118**, 3731–3743.

Zobrist, B., T. Koop, B. Luo, C. Marcolli, and T. Peter, 2007: Heterogeneous ice nucleation rate coefficient of water droplets coated by a nonadecanol monolayer. *J. Phys. Chem. C*, **111**, 2149–2155.